

ACTA POLYTECHNICA

Editorial Board:

ZDENĚK P. BAŽANT

Northwestern University McCormick School of Engineering, Illinois, USA

LENKA BODNÁROVÁ

Brno University of Technology, Czech Republic, Czech Republic

STEFFEN BOHRMANN

Hochschule Mannheim University of Applied Sciences, Germany

REINHARD HARTE

Department of Civil Engineering, Bergische Universität, Wuppertal, Germany

TATĀNA JAROŠÍKOVÁ

Faculty of Biomedical Engineering, Czech Technical University in Prague, Czech Republic

JITKA JÍROVÁ

Faculty of Transportation Sciences, Czech Technical University in Prague, Czech Republic

PETR JIZBA

Faculty of Nuclear Sciences and Physical Engineering, Czech Technical University in Prague, Czech Republic

PAVEL KALINA

Faculty of Architecture, Czech Technical University in Prague, Czech Republic

TOMÁŠ KOZIK

Department of Technology and Information Technologies, Constantine the Philosopher University in Nitra, Slovakia

FRANTIŠEK KRAUS

ETH Zürich, Switzerland

LIBOR MAKOVIČKA

Université de Franche Comté, France, France

ZUZANA MASÁKOVÁ

Faculty of Nuclear Sciences and Physical Engineering, Czech Technical University in Prague, Czech Republic

DAVID MURRAY-SMITH

School of Engineering, University of Glasgow, United Kingdom

DRAHOMÍR NOVÁK

Faculty of Civil Engineering, Brno University of Technology, Czech Republic

MARIÁN PECIAR

Institute of Chemical and Hydraulic Machines and Equipment (FME), Slovak University of Technology in Bratislava, Slovakia

JAN PÍCHAL

Faculty of Electrical Engineering, Czech Technical University in Prague, Czech Republic

MIROSLAV SÝKORA

Klokner Institute, Czech Technical University in Prague, Czech Republic

ZBYNĚK ŠKVOR (Head of Editorial Board)

Faculty of Electrical Engineering, Department of Electromagnetic Field, Czech Technical University in Prague, Czech Republic

RADEK ŠULC

Faculty of Mechanical Engineering, Czech Technical University in Prague, Czech Republic

MARTIN VOHRALÍK

INRIA de Paris, Institut universitaire de technologie, France

PAVEL TRTIK

Paul Scherrer Institut (PSI), Villigen, Switzerland, Switzerland

JAN ZEMAN

Faculty of Civil Engineering, Czech Technical University in Prague, Czech Republic



Title of journal: ACTA POLYTECHNICA. **Volume:** 62. **Number:** 6.
Periodicity: Bimonthly; 6 issues per year. **Date of issue:** December 31, 2022.
Published by: Czech Technical University in Prague,
Jugoslávských partyzánů 1580/3, 160 00 Praha 6 – Dejvice, Czech Republic.
IČO: 68407700.

Editorial Office: CTU — Central Library,
Technická 6, 160 80 Praha 6, Czech Republic.
acta@cvut.cz

Head of the Editorial Board: ZBYNĚK ŠKVOR (Faculty of Electrical Engineering, Department of Electromagnetic Field, Czech Technical University in Prague).

Editor-in-chief: TEREZA BULANOVA (CTU Central Library, Czech Technical University in Prague).

Editor: IVANA VÁVROVÁ (CTU Central Library, Czech Technical University in Prague).

Language Editor: TOMÁŠ MIKYŠKA (CTU Central Library, Czech Technical University in Prague).

Graphic design and typesetting: JITKA DAVIDOVÁ (CTU Central Library, Czech Technical University in Prague), TOMÁŠ PALIESEK (Faculty of Nuclear Sciences and Physical Engineering, Department of Physical Electronics, Czech Technical University in Prague).

Acta Polytechnica is available at <http://ojs.cvut.cz/ojs/index.php/ap>

Each article is assigned a digital object identifier <https://doi.org/10.14311/AP.2022.62.<4-digit article page number>>

ISSN 1805–2363 (online)

MK ČR E 4923



This work is licensed under a Creative Commons Attribution 4.0 International License.

Dear Reader

The ACTA POLYTECHNICA journal that you have just opened is a scientific journal published by the Czech Technical University in Prague. This journal first appeared in 1961 under the name “Proceedings of the Czech Technical University”. The main purpose of the journal was to support publication of the results of scientific and research activities at the Czech technical universities. Five years later, in 1966, the name of the journal was changed to Acta Polytechnica, and it started appearing quarterly. The main title ACTA POLYTECHNICA is accompanied by the subtitle JOURNAL OF ADVANCED ENGINEERING, which expresses the scope of the journal more precisely. Acta Polytechnica covers a wide spectrum of engineering topics in civil engineering, mechanical engineering, electrical engineering, nuclear sciences and physical engineering, architecture, transportation science, biomedical engineering and computer science and engineering. The scope of the journal is not limited to the realm of engineering. We also publish articles from the area of natural sciences, in particular physics and mathematics.

Acta Polytechnica is now being published in an enlarged format. Our aim is to be a high-quality multi-disciplinary journal publishing the results of basic research and also applied research. We place emphasis on the quality of all published papers. The journal should also serve as a bridge between basic research in natural sciences and applied research in all technical disciplines.

We invite researchers to submit high-quality original papers. The conditions of the submission process are explained in detail on: <http://ojs.cvut.cz/ojs/index.php/ap>. All papers will be reviewed, and accepted papers are published in English.

We hope that you will find our journal interesting, and that it will serve as a valuable source of scientific information.

Editorial Board

CONTENTS

- 574 Study of surface roughness with MHD and couple stress fluid on porous curved annular plates
Salma Alla Baksh, Hanumagowda Bannihalli Naganagowda
- 589 Stone topography – Useful tool in monument restoration process
Michal Cihla, Kateřina Kovářová, Richard Malát, Jaroslav Valach
- 595 Parametric study of the energy potential of a building's envelope with integrated energy-active elements
Daniel Kalús, Daniela Koudelková, Veronika Mučková, Martin Sokol, Mária Kurčová, Patrik Šťastný
- 607 Application of strut-and-tie models for assessing RC half-joints not complying with current code specifications
Gregoria Kotsovou, Emmanouil Vougioukas, Demetrios M. Cotsovos
- 618 Conversion of units of length from the Czech state standard to the geodetic baseline Javoriv
Jiří Lechner, Nikolai Sergeevich Kosarev, Igor Sergeevich Trevoho
- 627 Theoretical analysis of the influence of the chevron inclination angle on the thermal performance of a gasket plate heat exchanger
Élcio Nogueira
- 639 Design and simulation of a bearing housing aerospace component from titanium alloy (Ti6Al4V) for additive manufacturing
Moses Oyesola, Khumbulani Mpofo, Ilesanmi Daniyan, Ntombi Mathe
- 654 Recommended procedure for headroom design according to geometric parameters of building structures
Linda Veselá

STUDY OF SURFACE ROUGHNESS WITH MHD AND COUPLE STRESS FLUID ON POROUS CURVED ANNULAR PLATES

SALMA ALLA BAKSH*, HANUMAGOWDA BANNIHALLI NAGANAGOWDA

REVA University, School of Applied Sciences, Department of Mathematics, Bangalore-560064, India

* corresponding author: salma.alla@gmail.com

ABSTRACT. The purpose of this article is to examine the effect of surface roughness on porous curved annular plates lubricated with couple stress fluid in the presence of magnetic field. The MHD-Stochastic Reynolds equation is derived using Christensen's stochastic model and applied to predict the squeeze film characteristics of porous curved annular plates. The expressions for squeeze film pressure, load-carrying capacity, and squeeze film time are obtained analytically, the results are discussed for various values of operating parameters, and are plotted graphically. It is found that the squeeze film characteristics of porous curved annular plates are improved using a non-Newtonian fluid in the presence of an external magnetic field. The effect of roughness parameter is to increase (decrease) the squeeze film attributes for azimuthal (radial) roughness configuration as compared to the smooth case. Furthermore, the effect of permeability parameter is to decrease the pressure, load-carrying capacity, and squeeze-film time as compared to the non-porous case.

KEYWORDS: Couple stress fluid, MHD, surface roughness, porous medium, curved annular plates.

1. INTRODUCTION

In development of modernised machine equipment, a great attention is being paid to fluids which contain microstructures, such as suspensions, long-chained polymers, and additives. Newtonian fluid is one which does not depend on the dimension of fluid particles and hence such fluids are not a suitable engineering concept. Since non-Newtonian fluid flow cannot be precisely explained by the classical theory of continuum, numerous micro continuum theories have been constructed [1, 2] for explaining the particular behaviour of fluids featuring substructures that have the ability to interpret, pivot, or even distort on their own. Among them, Stoke's theory [3] is the simplest theory. Numerous authors have considered this theory to examine the impact of couple stresses for several kinds of fluid film bearings, for example, Lin [4] presented the sphere-flat plate, Kashinath [5] presented the parallel stepped squeeze films plates and Naduvinamani et al. [6] presented circular stepped plates. These authors have concluded that presence of couple stress fluid increases load and film time as compared to classical case. Recently, the concepts of Magnetohydrodynamics (MHD) in lubrication theory have caught the attention of numerous researchers. Since it is found that by using an electrically conducting fluid, the load-carrying capacity in a bearing can be increased. Many theoretical studies have carried out and detected that the impact of electromagnetic fields on squeeze films is beneficial particularly in the devices which involve high speeds and high external temperature. The hydromagnetic bearings, when compared to solid bearings, possess many advantages with couple stress fluid as lubricant. They are capable to function at high temperatures, and they offer a significant resistance to radioactive radiation. To protect undesirable variation in viscosity with temperature, the use of electrically conducting liquid-metal as lubricant is emphasized. In the occurrence of a magnetic field, many authors presented MHD performance of bearings lubricated with an electrically conducting fluid for smoothness, such as slider bearing by Snyder [7], inclined slider bearing and finite step slider bearing by Hughes [8, 9], parallel plate slider bearing by Kuzma [10], Lin [11] for annular disks, and Lin et al. [12] for curved annular. If we compare the results with a non-magnetic case there is an enhancement in film pressure, load and the length of the squeeze film time in presence of a magnetic field. In all the above-mentioned papers, it has been observed that the work is limited only for smooth surfaces.

But practically, even the rough surface is very crucial. Keeping this in mind, few investigators have tried to study the effect of porous medium on the rough surfaces. Nowadays, porous medium is one of areas of interest for many authors in various fields of science and engineering. Porous bearings are found to be advantageous due to its self-lubricating properties, lower costs, and design ease. Thus, the study of porous squeeze-film bearings was based on Darcy model, in which fluid flow through porous matrix obeys Darcy's law and no-slip condition was expected on the film interface. Several authors have examined rough surface for hydrodynamic lubrication using stochastic approaches. For example, the stochastic model for rough surfaces have been recognised by Christensen [13]. Numerous investigators have considered this model to examine the impact of roughness for distinctive bearings along with porous medium, such as Bhat et al. [14] for annular discs, Naduvinamani et

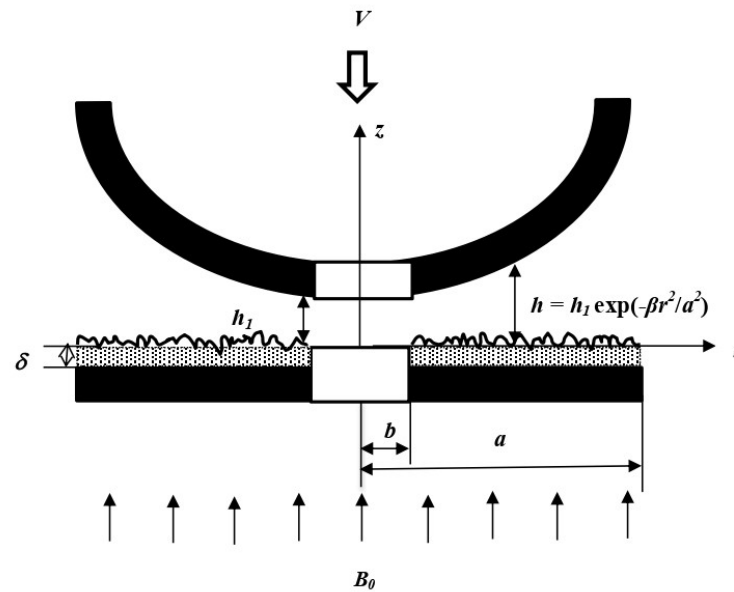


FIGURE 1. Geometry of rough - porous curved annular plates.

al. [15] for circular stepped plates, Syeda et al. [16] for Elliptical Plates, Hanumagowda et al. [17] for circular stepped plates, Biradar et al. [18] for Curved Annular Circular Plates, Hanumagowda et al. [19] for Conical Bearing, Patel et al. [20] for long bearings, Sankar et al. [21] for vertical annulus, Kiran et al. [22] for porous annulus, Shimpi et al. [23] for Curved Porous Annular Plates, and Niru et al. [24] for Curved Porous Annular Plates considering the rotation of magnetic particles and slip velocity. All these authors studied the effect of roughness in presence of porous medium and concluded that the effect of radial (azimuthal) roughness pattern on the bearing surface decrease (increase) the pressure, load carrying capacity, and approach of squeeze film time whereas the permeability parameter decreases these squeeze film attributes as compared to a non-porous case. Motivated by these investigations and their applications, in the present article, the authors examine the combined impact of MHD and surface roughness on the couple stress squeeze film lubrication between curved annular plates by considering the porous medium. The results are analysed for different values of the physical parameters – the pressure, load bearing capacity and squeeze film time. The obtained numerical results for a special case are found to be in good agreement with those of the results available in the literature. Furthermore, the results obtained reveal many interesting behaviours that warrant a further study of the equations related to non-Newtonian couple stress fluid phenomena in the presence of pressure dependent viscosity and slip velocity.

2. MATHEMATICAL FORMULATION AND SOLUTION

The geometry of rough-porous curved annular plates is displayed in Figure 1, having internal radius b and external radius a . The lower plate with permeable facing of thickness δ is fixed while the upper smooth plate is moving with a velocity $V = -dh_1/dt$ towards it. A transverse magnetic field B_0 is applied vertical to the plates.

The shape of the film thickness h is an exponential type as in Jaw-Rein Lin et al. [25]

$$h = h_1 \exp(-\beta r^2/a^2), \quad b \leq r \leq a, \quad (1)$$

where β is the curvature parameter and h_1 is the initial minimum film thickness.

In view of hydrodynamic and hydro-magnetic lubrication, the governing equations, which satisfies Stokes [3] model, are considered as

$$\mu \frac{\partial^2 u}{\partial z^2} - \eta \frac{\partial^4 u}{\partial z^4} - \sigma B_0^2 u = \frac{\partial p}{\partial r}, \quad (2)$$

$$\frac{\partial p}{\partial z} = 0, \quad (3)$$

$$\frac{1}{r} \frac{\partial}{\partial r}(ru) + \frac{\partial w}{\partial z} = 0, \quad (4)$$

in which the components of velocities are u and w in r and z direction, respectively, p represents the pressure in the region, η is the materialistic constant, σ is the electrical conductivity and B_0 is the applied magnetic field.

For the porous region

$$\frac{1}{r} \frac{\partial}{\partial r} (ru^*) + \frac{\partial w^*}{\partial z} = 0. \quad (5)$$

Governing Modified Darcy's equation given by Biradar et al. [26], the velocity components u^* and w^* in porous region are

$$u^* = \frac{-k}{\mu \left(1 - \Phi + \frac{kM^2}{mh_0^2}\right)} \frac{\partial p^*}{\partial r}, \quad (6)$$

$$w^* = \frac{-k}{\mu(1 - \Phi)} \frac{\partial p^*}{\partial z}, \quad (7)$$

where p^* is the pressure in the porous region, k is the permeability parameter, Φ is the ratio of the microstructure size to pore size, $M = B_0 H_0 \left(\frac{\sigma}{\mu}\right)^{1/2}$ is the Hartmann number.

The velocity boundary conditions are:

- For lower rough-porous curved annular surface at $z = 0$

$$u = 0, \quad \frac{\partial^2 u}{\partial z^2} = 0, \quad (\text{Vanishing of couple stresses}) \quad (8a)$$

$$w = 0. \quad (8b)$$

- For upper curved annular surface at $z = h$

$$u = 0, \quad \frac{\partial^2 u}{\partial z^2} = 0, \quad (\text{Vanishing of couple stresses}) \quad (9a)$$

$$w = V = \frac{-\partial h_1}{\partial t}. \quad (9b)$$

Solving Equation (1) subject to boundary conditions (8a) and (8b), the expression for the velocity component is

$$u = \{(g_1 - g_2) - 1\} \frac{h_0^2}{\mu M^2} \frac{\partial p}{\partial r}. \quad (10)$$

Here,

$$g_1 = g_{11}, \quad g_2 = g_{12}, \quad \text{for } 4M^2 l^2 / h_0^2 < 1 \quad (11a)$$

$$g_1 = g_{21}, \quad g_2 = g_{22}, \quad \text{for } 4M^2 l^2 / h_0^2 = 1 \quad (11b)$$

$$g_1 = g_{31}, \quad g_2 = g_{32}, \quad \text{for } 4M^2 l^2 / h_0^2 > 1 \quad (11c)$$

The associated relations in Equations (11a), (11b) and (11c) are given in Appendix A.

The continuity equation in polar form is obtained by integrating Equation (3) over film thickness using the boundary conditions (8b) and (9b), resulting in

$$\frac{1}{r\mu} \frac{\partial}{\partial r} \left\{ rS(h, l, M) \frac{\partial p}{\partial r} \right\} = w_h - w_0, \quad (12)$$

but upper surface is not porous $w_h = 0$.

The velocity component in z-direction is continuous at the interface between the lower plate and film so that

$$w_0 = - \left\{ \frac{dh}{dt} + \frac{k}{\mu(1 - \Phi)} \left(\frac{\partial p^*}{\partial z} \right)_{z=0} \right\}. \quad (13)$$

By substituting Equation (13) in (12), we obtain

$$\frac{1}{r\mu} \frac{\partial}{\partial r} \left\{ rS(h, l, M) \frac{\partial p}{\partial r} \right\} = \frac{dh}{dt} + \frac{k}{\mu(1 - \Phi)} \left(\frac{\partial p^*}{\partial z} \right)_{z=0}, \quad (14)$$

where

$$S(h, l, M) = \begin{cases} \frac{h_0^2}{M^2} \left\{ \frac{2l}{(A^2 - B^2)} \left(\frac{B^2}{A} \tanh \frac{Ah}{2l} - \frac{A^2}{B} \tanh \frac{Bh}{2l} \right) + h \right\} & \text{for } M^2 l^2 / h_0^2 < 1, \\ \frac{h_0^2}{M^2} \left\{ \frac{h}{2} \sec^2 h^2 \left(\frac{h}{2\sqrt{2}l} \right) - 3\sqrt{2}l \tanh \left(\frac{h}{2\sqrt{2}l} \right) + h \right\} & \text{for } M^2 l^2 / h_0^2 = 1, \\ \frac{h_0^2}{M^2} \left\{ \frac{2lh_0}{M} \left(\frac{(A_2 \cot \theta - B_2) \sin B_2 h - (B_2 \cot \theta + A_2) \sin A_2 h}{\cos B_2 h + \cosh A_2 h} \right) + h \right\} & \text{for } M^2 l^2 / h_0^2 > 1. \end{cases}$$

In porous region, fluid pressure satisfies the equation

$$\frac{1}{r} \frac{\partial}{\partial r} \left(r \frac{\partial p^*}{\partial r} \right) + \left(\frac{D}{1 - \Phi} \right) \frac{\partial p^*}{\partial z} = 0, \tag{15}$$

where $D = \left(1 - \Phi + \frac{kM^2}{mh_0^2} \right)$.

Let us integrate the above equation using Morgan-Cameron approximation [27] that is $\frac{\partial p^*}{\partial r}$ at $z = -\delta$ yields,

$$\left(\frac{\partial p^*}{\partial z} \right)_{z=0} = - \left(\frac{1 - \Phi}{D} \right) \int_{-\delta}^0 \frac{1}{r} \frac{\partial}{\partial r} \left(r \frac{\partial p^*}{\partial r} \right) dz.$$

Since porous thickness layer δ is exceedingly small, Morgan-Cameron approximation [27] is considered and Equation (15) yields

$$\left(\frac{\partial p^*}{\partial z} \right)_{z=0} = -\delta \left(\frac{1 - \Phi}{D} \right) \frac{1}{r} \frac{\partial}{\partial r} \left(r \frac{\partial p}{\partial r} \right), \tag{16}$$

where $\frac{\partial p^*}{\partial z} = 0$ at $z = -\delta$ has been used.

Using Equation (16) in (14) the Reynold's modified equation results in

$$\frac{1}{r\mu} \frac{\partial}{\partial r} \left\{ \left(S(h, l, M) + \frac{\delta k}{D} \right) r \frac{\partial p}{\partial r} \right\} = V. \tag{17}$$

According to the stochastic model of Christensen [13], the film thickness H is

$$H = h + h_s(r, \theta, \xi), \tag{18}$$

where h is the nominal thickness, h_s is the part owing to surface roughness as measured from nominal level and ξ is a stochastic variable which describes roughness geometry.

2.1. STOCHASTIC REYNOLDS EQUATION

Let us take the stochastic mean of Equation (17) with respect to probability density function $g(h_s)$, we get

$$\frac{1}{r\mu} \frac{\partial}{\partial r} \left\{ \left(E \left(S(h, l, M) + \frac{\delta k}{D} \right) \right) r \frac{\partial E(p)}{\partial r} \right\} = V, \tag{19}$$

where $E(\bullet) = \int_{-\infty}^{\infty} (\bullet) g(h_s) dh_s$.

The roughness distribution function based on Christensen's theory is in form

$$g(h_s) = \begin{cases} \frac{35}{32n^7} (n^2 - h_s^2)^3, & -n < h_s < n \\ 0, & otherwise \end{cases} \tag{20}$$

where $n = 3\bar{\sigma}$ and $\bar{\sigma}$ is the standard deviation.

Generally, there are two kinds of roughness configuration, namely:

- **Radial Roughness configuration:** It is one-dimensional roughness in the form of long, narrow ridges and valleys running in r -direction. Film thickness and average modified Reynold's equation is

$$H = h + h_s(\theta, \xi), \tag{21}$$

$$\frac{1}{r\mu} \frac{\partial}{\partial r} \left\langle \left[ES(h, l, M) + \frac{\delta k}{D} \right] r \frac{\partial E(p)}{\partial r} \right\rangle = V, \tag{22}$$

where

$$E(S(h, l, M)) = \frac{35}{32n^7} \int_{-n}^n S(h, l, M) (n^2 - h_s^2)^3 dh_s.$$

- **Azimuthal Roughness configuration:** It is one-dimensional roughness in the form of long, narrow ridges and valleys running in θ -direction. Film thickness and average modified Reynold's equation is

$$H = h + h_s(r, \xi), \tag{23}$$

$$\frac{1}{r\mu} \frac{\partial}{\partial r} \left\langle \left([E1/S(h, l, M)]^{-1} + \frac{\delta k}{D} \right) r \frac{\partial E(p)}{\partial r} \right\rangle = V, \tag{24}$$

where

$$E \left(\frac{1}{S(h, l, M)} \right) = \frac{35}{32n^7} \int_{-n}^n \frac{(n^2 - h_s^2)^3}{S(h, l, M)} dh_s.$$

Introducing the following non-dimensional quantities in Equation (19),

$$r^* = \frac{r}{a}, \quad h_1^* = \frac{h_1}{h_0}, \quad h^* = \frac{h}{h_0}, \quad l^* = \frac{2l}{h_0}, \quad P = -\frac{h_1^3 p}{\mu a^2 V}, \quad \delta^* = \frac{\delta}{h_0}, \quad \Psi = \frac{k\delta}{h_0^3}, \quad D_1 = \left(1 - \Phi + \frac{\Psi M^2}{m\delta^*}\right), \quad C = \frac{n}{h_0}.$$

Here, h_0 is the minimum film thickness.

The modified-stochastic Reynold's equation for film pressure is given by

$$\frac{1}{r^*} \frac{\partial}{\partial r^*} \left\{ J(H, l^*, M, \Psi, C) r^* \frac{\partial P}{\partial r^*} \right\} = -1, \quad (25)$$

where

$$J(H, l^*, M, \Psi, C) = \begin{cases} E \langle S(h_1^*, l^*, M) \rangle + \frac{\Phi}{D_1} & \text{for radial roughness,} \\ \langle E(1/S(h_1^*, l^*, M)) \rangle^{-1} + \frac{\Phi}{D_1} & \text{for azimuthal roughness.} \end{cases}$$

The relevant boundary conditions to present the squeeze problem is

$$p = 0 \quad \text{for } r^* = \alpha = b/a, \quad (26a)$$

$$p = 0 \quad \text{for } r^* = 1. \quad (26b)$$

The non-dimensional stochastic Reynold equation (25) is integrated using the boundary conditions (26a) and (26b), which results in the expression for non-dimensional MHD mean squeezing film pressure:

$$p = \frac{f_2(r^*)f_1(1) - f_1(r^*)f_2(1)}{2f_2(1)}, \quad (27)$$

where

$$f_1(1) = \int_{r^*=\alpha}^1 \frac{r^*}{J(H, l^*, M, \Psi, C)} dr^*, \quad f_2(1) = \int_{r^*=\alpha}^1 \frac{1}{r^* J(H, l^*, M, \Psi, C)} dr^*.$$

The pressure field over the plate surface is integrated to find the load supporting capacity and is

$$W = \int_{r=b}^a 2\pi r p dr. \quad (28)$$

The non-dimensional MHD mean load-supporting capacity W is

$$W = \frac{E(W)h_1^3}{2\pi\mu a^4(-dh_1/dt)} = \frac{-1}{2} \int_{r^*=\alpha}^1 f_1(r^*)r^* dr^* + \frac{1}{2} \frac{f_1(1)}{f_2(1)} \int_{r^*=\alpha}^1 f_2(r^*)r^* dr^*. \quad (29)$$

The non-dimensional squeeze film time for film thickness is

$$T = \frac{E(W)h_1^2}{\pi\mu a^4} t = \int_{h_1^*}^1 \left(\frac{2f_2(1)}{f_2(1) \int_{r^*=\alpha}^1 f_1(r^*)r^* dr^* - f_1(1) \int_{r^*=\alpha}^1 f_2(r^*)r^* dr^*} \right) dh_1^*. \quad (30)$$

3. RESULT AND DISCUSSIONS

In the present article, the impact of roughness, MHD, and couple stress fluid is investigated. The MHD-Stochastic Reynolds-type equation is derived using Christensen's stochastic model and applied to predict the squeeze film characteristics of porous curved annular plates. The results are discussed for various values of non-dimensional quantities, such as Hartmann number M , couple stress parameter l^* , roughness parameter C , permeability parameter Ψ , curvature parameter β , and radius ratio α . To discuss the squeeze film characteristics, the following parameters range is considered:

$$M = 0, 2, 4; \quad l^* = 0.0, 0.2, 0.4; \quad C = 0.0, 0.2, 0.4; \quad \beta = -0.5, 0, 0.5; \quad \Psi = 0, 0.001, 0.1; \quad \alpha = 0.2, 0.4, 0.6$$

and $m = 0.6; \delta^* = 0.01; \Phi = 0.2$ are fixed.

Limiting cases:

- (i) As $C \rightarrow 0$, corresponds to the smooth case discussed by Hanumagowda et al. [28],
- (ii) As $C \rightarrow 0, M \rightarrow 0$, corresponds to the non-magnetic case discussed by Gupta et al. [29],
- (iii) As $C \rightarrow 0, M \rightarrow 0, l^* \rightarrow 0$, corresponds to the Newtonian case studied by Jaw et al. [25],
- (iv) As $\Psi \rightarrow 0$, corresponds to the non-porous case discussed by Hanumagowda et al. [28],
- (v) As $\beta = 0$, corresponds to the annular plates discussed by Syeda et al. [30].

3.1. MEAN FILM PRESSURE

Figure 2 presents the profile of mean pressure P along dimensionless co-ordinate axial r^* as a function of C for both roughness configurations and clearly shows that for larger C values, the mean pressure inclines (declines) for azimuthal (radial) roughness structures, and also, when $C \rightarrow 0$, it reduces to smooth case. In Figure 3, a graph of P against r^* as a function of Ψ is presented and can clearly be seen that for increasing Ψ values, the mean pressure decreases for azimuthal roughness rather than radial roughness structure. Figure 4 shows the distinctive values of Hartmann number, the graph P against r^* is presented and shows that for increasing M values, the pressure increases. The profile of P against r^* for various l^* values is described in Figure 5 and it can be seen that the impact of l^* is to enhance P . Figure 6 displays the graph of P against r^* for distinctive values of β and it can be seen that the pressure is a significant factor for increasing β values.

3.2. MEAN LOAD SUPPORTING CAPACITY

The deviation of mean load supporting capacity W against curvature parameter β as a function of C is displayed in Figure 7 for both roughness configurations and it can be seen that when $C = 0$, an azimuthal and radial roughness configurations coincide and reduce to a smooth case. In Figure 8 the profile of W against β as a function of permeability parameter Ψ is depicted and shows that the mean load declines for larger Ψ values. The graph W along β for several values of Hartmann number is illustrated in Figure 9 and for distinct values of l^* in Figure 10. It is found that the impact of couple stress fluid in the existence of applied magnetic field is to substantially enhance the load supporting capacity as compared to Newtonian fluids. This is due to the use of magnetic field normal to the flow, which results in a lower velocity of the lubricant in the fluid film region. Thus, a large amount of the fluid is retained in the film region, and this yields a rise in pressure. Figure 11 represents the load profile W along β for distinct values of radius ratio α for both roughness configurations and it shows that the mean load decreases for rising values of α . Furthermore, the mean load increases for larger β values.

3.3. SQUEEZE FILM TIME

Figure 12 shows the deviation of dimensionless squeeze film T against dimensionless film height h_1^* for distinct values of C , illustrated for both roughness configurations. From the results obtained, squeeze film time T is predicted to increase (decreases) for azimuthal (radial) roughness configurations as compared to the solid case. The time profile T against h_1^* for distinct values of Ψ is presented in Figure 13 and it clearly shows that T increases for decreasing Ψ values, even more significantly for the azimuthal roughness structure. Figure 14 depict the time variation T against h_1^* as a function of Hartmann number M and shows that T increases for larger M values.

The graph of T against h_1^* for various values of couple stress parameter l^* is shown in Figure 15 and it can clearly be seen that the impact of l^* enhances the squeeze film time. Figure 16 represents the deviation of T against h_1^* for distinct values of radius ratio α and shows that T decreases for larger values of radius ratio. The time profile T along h_1^* as a function of curvature parameter β is illustrated in Figure 17 and shows that for increasing β values, T also increases.

4. CONCLUSION

Using a stochastic model of Christensen for rough surfaces, the present analysis predicts the influence of roughness on squeeze film attributes for porous annular plates with MHD and couple stress fluid. Through the above discussions, conclusions are drawn as follows:

- The surface roughness impact increases the pressure, load supporting capacity and prolongs film time in comparison with the smooth case. This impact is greater for the azimuthal roughness than the radial roughness structure.
- In a comparison with non-magnetic case, the impact of Hartmann number enhances the squeezing attributes for both roughness structures.
- The couple stress effects for azimuthal roughness are more pronounced than for the radial. Also, the squeeze film attributes are very significant for non-Newtonian case.
- The permeability parameter effect reduces the performance of squeeze-film characteristics as compared to the solid case.
- The load and film time are reduced due to an increase in radius ratio.
- Obtained results are compared with previous analysis carried out by Hanumagowda et al. [28] and shown in the Table 1. It is observed that there is a substantial increase in load and time for both roughness configurations in the porous region. An increase of 14 % (15 %) in radial (azimuthal) roughness configuration is observed when $M = 6$, $C = 0.2$ and $\Psi = 0.001$.
- It is anticipated that these results will help the design engineers in choosing the most suitable structure, magnetic field, and lubricant additives to prolong the bearing's life. These results are in agreement with the experimental study by Artur et al. [31] that the final composition of the lubricant should be supplemented with suitably selected additives.

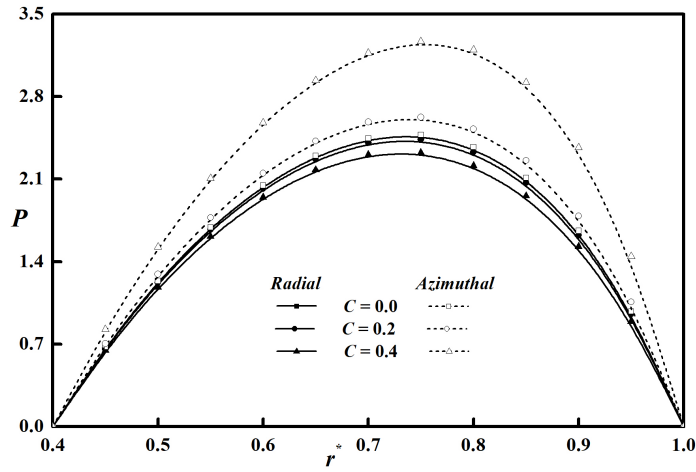


FIGURE 2. Variation of P against r^* for distinct values of C with $M = 3, l^* = 0.3, \alpha = 0.4, \beta = 0.5, \Psi = 0.001, m = 0.6, \delta^* = 0.01, \Phi = 0.2$.

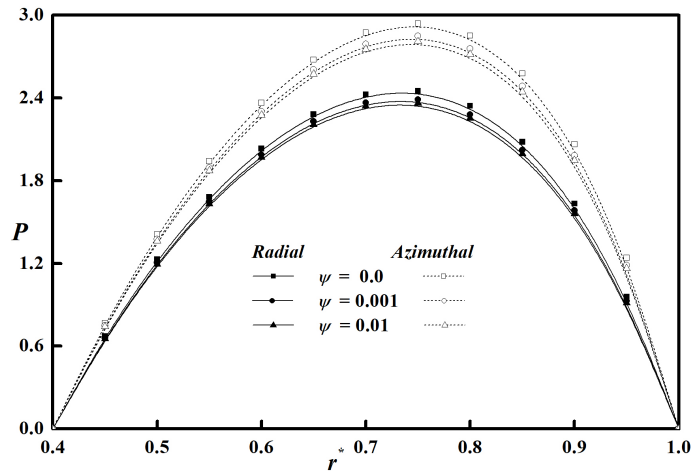


FIGURE 3. Variation of P against r^* for distinct values of Ψ with $M = 3, l^* = 0.3, C = 0.3, \alpha = 0.4, \beta = 0.5, m = 0.6, \delta^* = 0.01, \Phi = 0.2$.

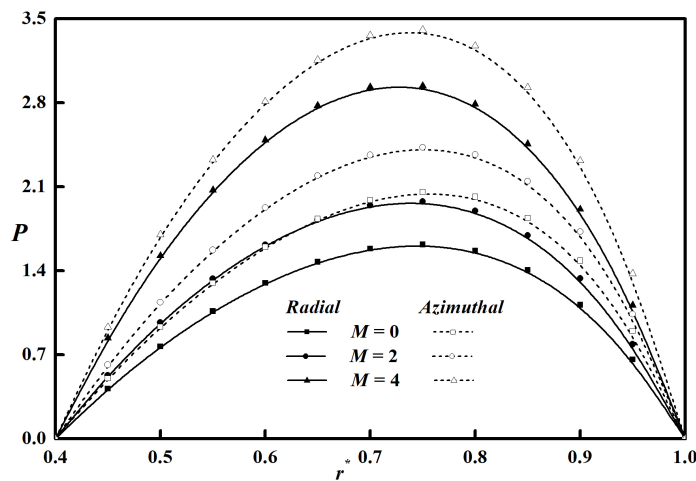


FIGURE 4. Variation of P against r^* for distinct values of M with $C = 0.3, l^* = 0.3, \alpha = 0.4, \beta = 0.5, \Psi = 0.001, m = 0.6, \delta^* = 0.01, \Phi = 0.2$.

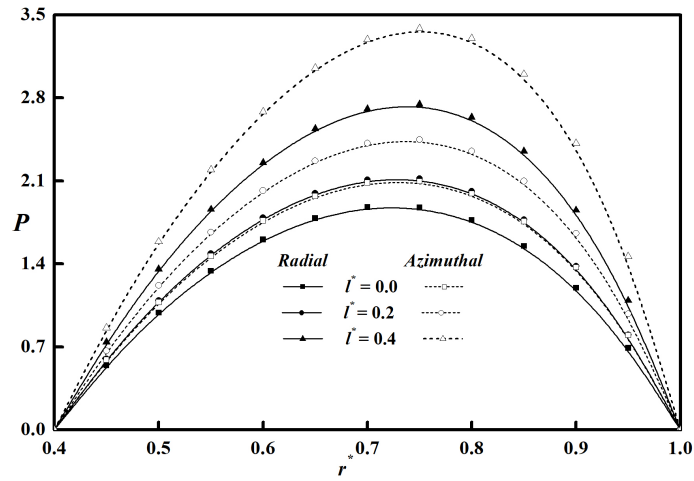


FIGURE 5. Variation of P against r^* for distinct values of l^* with $C = 0.3$, $M = 3$, $\alpha = 0.4$, $\beta = 0.5$, $\Psi = 0.001$, $m = 0.6$, $\delta^* = 0.01$, $\Phi = 0.2$.

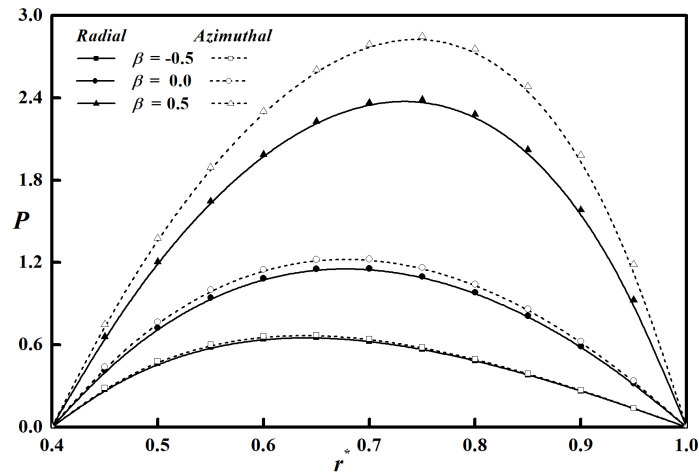


FIGURE 6. Variation of P against r^* for distinct values of β with $C = 0.3$, $M = 3$, $\alpha = 0.4$, $l^* = 0.3$, $\Psi = 0.001$, $m = 0.6$, $\delta^* = 0.01$, $\Phi = 0.2$.

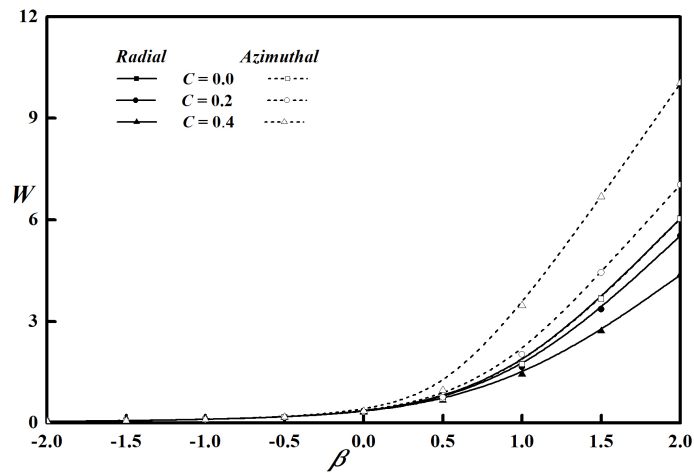


FIGURE 7. Variation of W against β for various values of C with $M = 3$, $l^* = 0.3$, $\alpha = 0.4$, $\Psi = 0.001$, $m = 0.6$, $\delta^* = 0.01$, $\Phi = 0.2$.

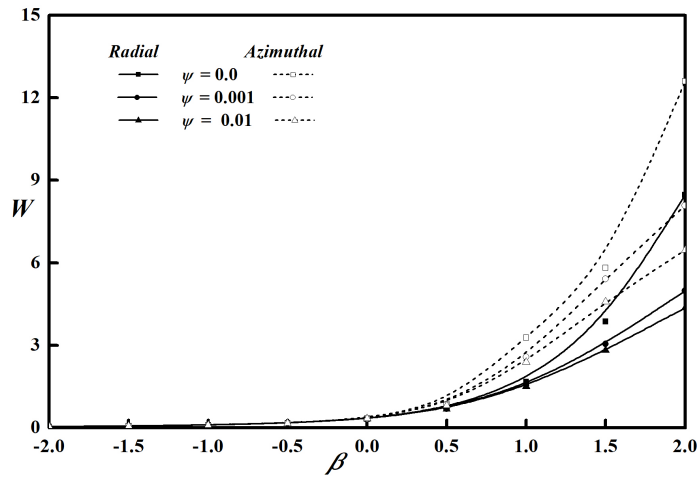


FIGURE 8. Variation of W against β for various values of Ψ with $M = 3, l^* = 0.3, C = 0.3, \alpha = 0.4, m = 0.6, \delta^* = 0.01, \Phi = 0.2$.

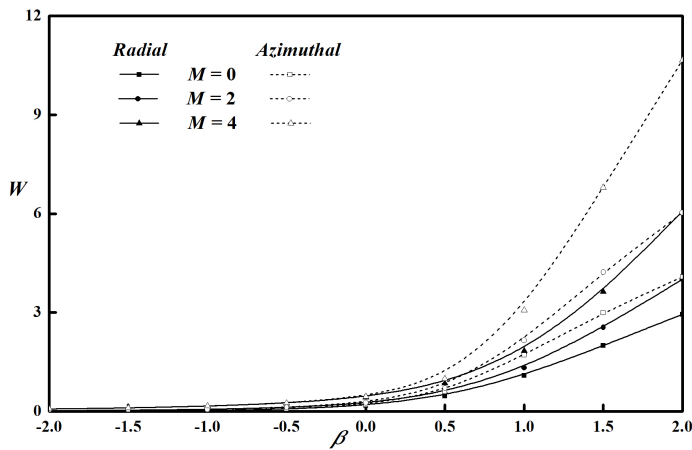


FIGURE 9. Variation of W against β for various values of M with $C = 0.3, l^* = 0.3, \alpha = 0.4, \Psi = 0.001, m = 0.6, \delta^* = 0.01, \Phi = 0.2$.

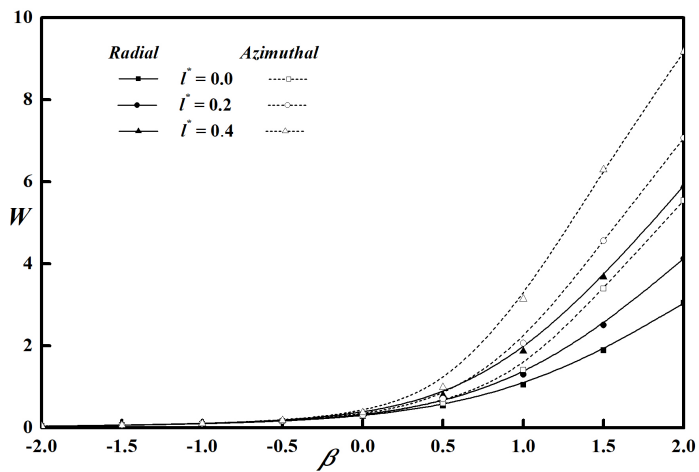


FIGURE 10. Variation of W against β for various values of l^* with $C = 0.3, M = 3, \alpha = 0.4, \Psi = 0.001, m = 0.6, \delta^* = 0.01, \Phi = 0.2$.

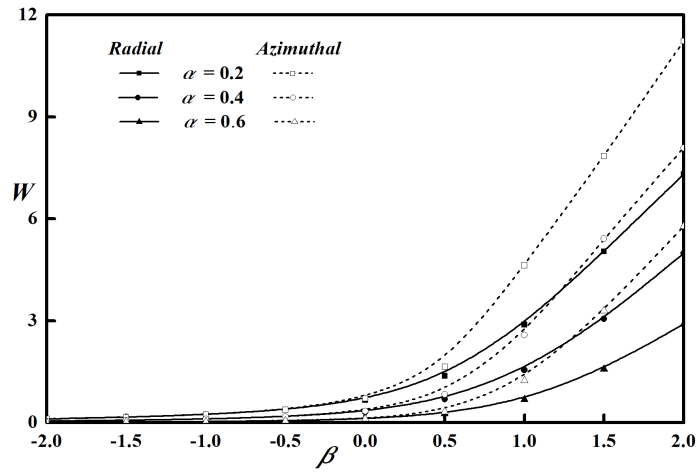


FIGURE 11. Variation of W against β for various values of α with $C = 0.3$, $M = 3$, $l^* = 0.3$, $\Psi = 0.001$, $m = 0.6$, $\delta^* = 0.01$, $\Phi = 0.2$.

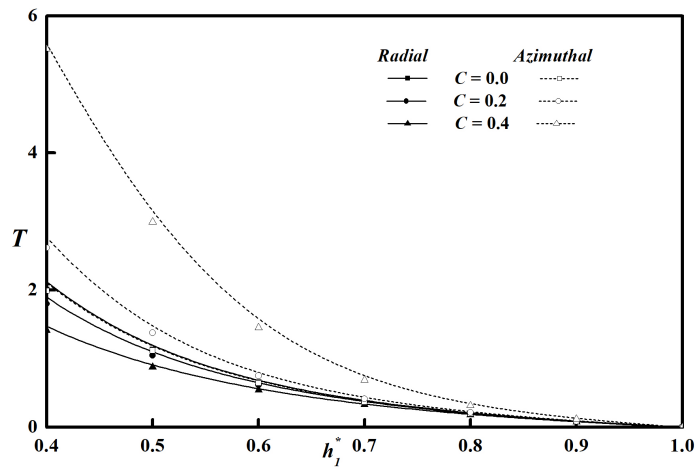


FIGURE 12. Variation of T against h_1^* for different values of C with $M = 3$, $l^* = 0.3$, $\alpha = 0.4$, $\beta = 0.5$, $\Psi = 0.001$, $m = 0.6$, $\delta^* = 0.01$, $\Phi = 0.2$.

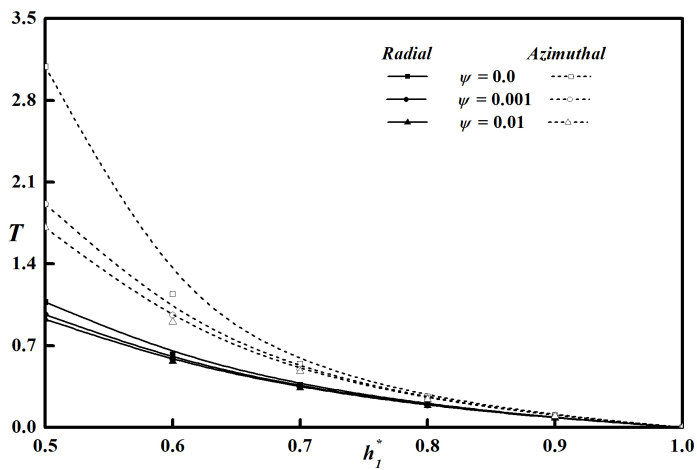


FIGURE 13. Variation of T against h_1^* for different values of Ψ with $M = 3$, $l^* = 0.3$, $C = 0.3$, $\alpha = 0.4$, $\beta = 0.5$, $m = 0.6$, $\delta^* = 0.01$, $\Phi = 0.2$.

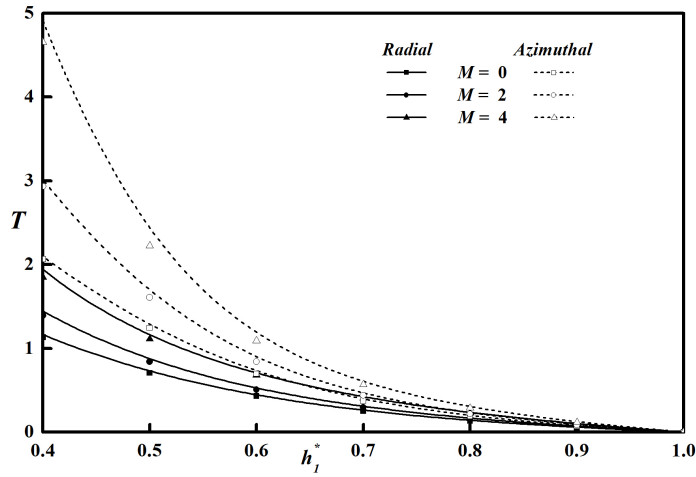


FIGURE 14. Variation of T against h_1^* for different values of M with $C = 0.3$, $l^* = 0.3$, $\alpha = 0.4$, $\beta = 0.5$, $\Psi = 0.001$, $m = 0.6$, $\delta^* = 0.01$, $\Phi = 0.2$.

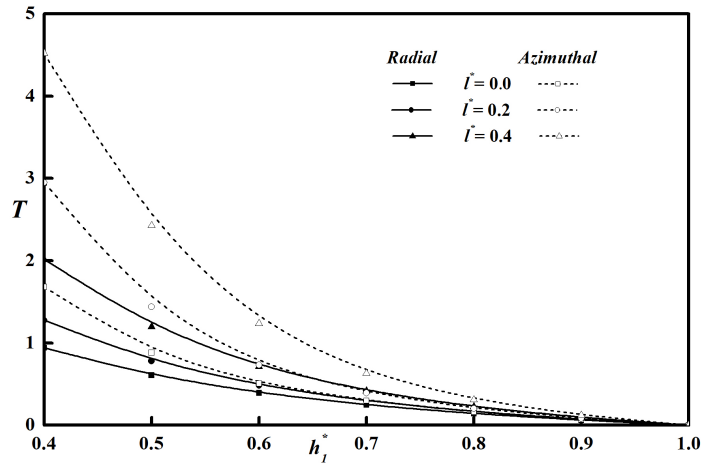


FIGURE 15. Variation of T against h_1^* for different values of l^* with $C = 0.3$, $M = 3$, $\alpha = 0.4$, $\beta = 0.5$, $\Psi = 0.001$, $m = 0.6$, $\delta^* = 0.01$, $\Phi = 0.2$.

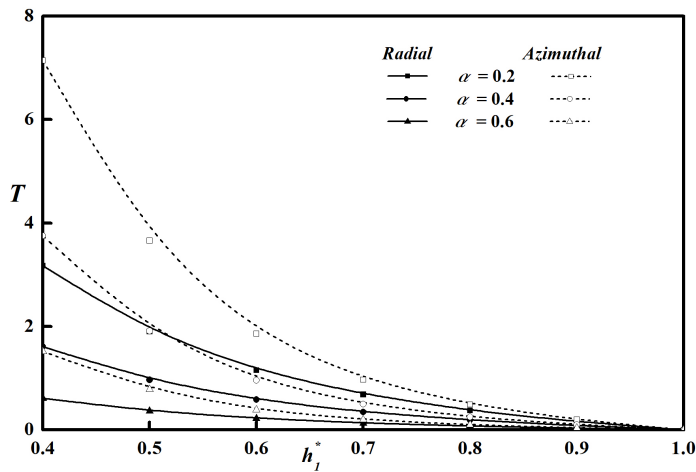


FIGURE 16. Variation of T against h_1^* for different values of α with $C = 0.3$, $M = 3$, $l^* = 0.3$, $\beta = 0.5$, $\Psi = 0.001$, $m = 0.6$, $\delta^* = 0.01$, $\Phi = 0.2$.

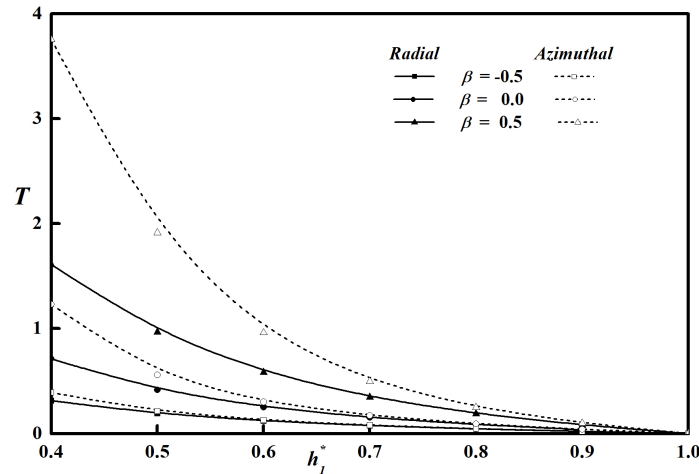


FIGURE 17. Variation of T against h_1^* for different values of β with $C = 0.3, M = 3, l^* = 0.3, \alpha = 0.4, \Psi = 0.001, m = 0.6, \delta^* = 0.01, \Phi = 0.2$.

M	Hanumagowda et al. [28]	Present analysis											
		$C = 0, \Psi = 0$				$C = 0.2, l^* = 0.4, \Psi = 0.001$				$C = 0.2, l^* = 0.4, \Psi = 0.01$			
		$l^* = 0$	$l^* = 0.2$	$l^* = 0$	$l^* = 0.2$	Radial	Azimuthal	Radial	Azimuthal	Radial	Azimuthal		
W	0	0.3740	0.4471	0.3740	0.4471	0.5854	0.6588	0.3743	0.4016				
	2	0.4610	0.5371	0.4610	0.5371	0.6946	0.7713	0.6678	0.7378				
	4	0.7128	0.7980	0.7128	0.7980	0.9802	1.0591	0.9740	1.0518				
	6	1.1194	1.2200	1.1194	1.2200	1.4230	1.5033	1.4201	1.5000				
T	0	0.1496	0.1788	0.1496	0.1788	0.2341	0.2635	0.1497	0.1606				
	2	0.1844	0.2148	0.1844	0.2148	0.2778	0.3085	0.2671	0.2951				
	4	0.2851	0.3192	0.2851	0.3192	0.3920	0.4236	0.3896	0.4207				
	6	0.4477	0.4880	0.4477	0.4880	0.5692	0.6013	0.5680	0.6000				

TABLE 1. Numerical comparison of the Non-dimensional load carrying capacity W and Non-dimensional squeeze film time T between Hanumagowda et al. [28] and the present analysis with $h^* = 0.5, \beta = 0.5, \alpha = 0.4, m = 0.6, \delta^* = 0.01, \Phi = 0.2$ as fixed.

ACKNOWLEDGEMENTS

Authors acknowledge the support from REVA University for the facilities provided to carry out the research. The authors wish to express their deep gratitude to the reviewers of the original manuscript for their kind suggestions based upon which the present version of the paper has been prepared.

REFERENCES

- [1] T. Ariman, M. A. Turk, N. D. Sylvester. Microcontinuum fluid mechanics – A review. *International Journal of Engineering Science* **11**(8):905–930, 1973. [https://doi.org/10.1016/0020-7225\(73\)90038-4](https://doi.org/10.1016/0020-7225(73)90038-4).
- [2] T. Ariman, M. A. Turk, N. D. Sylvester. Applications of microcontinuum fluid mechanics. *International Journal of Engineering Science* **12**(4):273–293, 1974. [https://doi.org/10.1016/0020-7225\(74\)90059-7](https://doi.org/10.1016/0020-7225(74)90059-7).
- [3] V. K. Stokes. Couple stresses in fluids. *The Physics of Fluids* **9**(9):1709–1715, 1966. <https://doi.org/10.1063/1.1761925>.
- [4] J.-R. Lin. Squeeze film characteristics between a sphere and a flat plate: couple stress fluid model. *Computers & Structures* **75**(1):73–80, 2000. [https://doi.org/10.1016/S0045-7949\(99\)00080-2](https://doi.org/10.1016/S0045-7949(99)00080-2).
- [5] B. Kashinath. Squeeze film lubrication between parallel stepped plates with couplestress fluids. *International Journal of Statistika and Matematika* **3**(2):65–69, 2012.
- [6] N. B. Naduvinamani, A. Siddangouda. Squeeze film lubrication between circular stepped plates of couple stress fluids. *Journal of the Brazilian Society of Mechanical Sciences and Engineering* **31**(1):21–26, 2009. <https://doi.org/10.1590/S1678-58782009000100004>.

- [7] W. T. Snyder. The magnetohydrodynamic slider bearing. *Journal of Basic Engineering* **84**(1):197–202, 1962. <https://doi.org/10.1115/1.3657252>.
- [8] W. F. Hughes. The magnetohydrodynamic inclined slider bearing with a transverse magnetic field. *Wear* **6**(4):315–324, 1963. [https://doi.org/10.1016/0043-1648\(63\)90164-9](https://doi.org/10.1016/0043-1648(63)90164-9).
- [9] W. F. Hughes. The magnetohydrodynamic finite step slider bearing. *Journal of Basic Engineering* **85**(1):129–135, 1963. <https://doi.org/10.1115/1.3656508>.
- [10] D. C. Kuzma. The magnetohydrodynamic parallel plate slider bearing. *Journal of Basic Engineering* **87**(3):778–780, 1965. <https://doi.org/10.1115/1.3650685>.
- [11] J.-R. Lin. Magneto-hydrodynamic squeeze film characteristics between annular disks. *Industrial Lubrication and Tribology* **53**(2):66–71, 2001. <https://doi.org/10.1108/00368790110384028>.
- [12] J. R. Lin, R. F. Lu, W. H. Liao. Analysis of magnetohydrodynamic squeeze film characteristics between curved annular plates. *Industrial Lubrication and Tribology* **56**(5):300–305, 2004. <https://doi.org/10.1108/00368790410550714>.
- [13] H. Christensen. Stochastic models for hydrodynamic lubrication of rough surfaces. *Proceedings of the Institution of Mechanical Engineers* **184**(1):1013–1026, 1969. https://doi.org/10.1243/PIME_PROC_1969_184_074_02.
- [14] M. V. Bhat, G. M. Deheri. Squeeze film behaviour in porous annular discs lubricated with magnetic fluid. *Wear* **151**(1):123–128, 1991. [https://doi.org/10.1016/0043-1648\(91\)90352-U](https://doi.org/10.1016/0043-1648(91)90352-U).
- [15] N. B. Naduvinamani, B. N. Hanumagowda, S. Tasneem Fathima. Combined effects of MHD and surface roughness on couple-stress squeeze film lubrication between porous circular stepped plates. *Tribology International* **56**:19–29, 2012. <https://doi.org/10.1016/j.triboint.2012.06.012>.
- [16] S. T. Fathima, N. B. Naduvinamani, J. S. Kumar, B. N. Hanumagowda. Derivation of modified MHD-stochastic Reynolds equation with conducting couple stress fluid on the squeeze film lubrication of porous rough elliptical plates. *International Journal of Mathematical Archive* **5**(8):135–145, 2014.
- [17] B. N. Hanumagowda, B. T. Raju, J. Santhosh Kumar, K. R. Vasanth. Combined effect of surface roughness and pressure-dependent viscosity over couple-stress squeeze film lubrication between circular stepped plates. *Proceedings of the Institution of Mechanical Engineers, Part J: Journal of Engineering Tribology* **232**(5):525–534, 2018. <https://doi.org/10.1177/1350650117721432>.
- [18] T. Biradar, B. N. Hanumagowda, S. Biradar, et al. Effect of MHD and couple stress on squeeze film characteristics between porous curved annular circular plates. *International Journal of Mechanical and Production Engineering Research and Development* **10**(3):8535–8546, 2020.
- [19] B. N. Hanumagowda, A. Salma, S. S. Nair. Combined effect of rough surface with MHD on porous conical bearing with conducting couple-stress fluid. *Palestine Journal of Mathematics* **10**(1):59–68, 2021. <https://doi.org/https://pjm.ppu.edu/vol1/828>.
- [20] J. Patel, G. M. Deheri. Influence of viscosity variation on ferrofluid based long bearing. *Reports in Mechanical Engineering* **3**(1):37–45, 2021. <https://doi.org/10.31181/rme200103037j>.
- [21] M. Sankar, S. Kemparaju, B. M. R. Prasanna, S. Eswaramoorthi. Buoyant convection in porous annulus with discrete sources-sink pairs and internal heat generation. *Journal of Physics: Conference Series* **1139**(1):012026, 2018. <https://doi.org/10.1088/1742-6596/1139/1/012026>.
- [22] S. Kiran, M. Sankar, Y. H. Gangadharaiah, B. V. Dhananjayamurthy. Natural convection in a linearly heated vertical porous annulus under the effect of magnetic field. In G. Manik, S. Kalia, S. K. Sahoo, et al. (eds.), *Advances in Mechanical Engineering*, pp. 537–546. Springer Singapore, Singapore, 2021. ISBN 978-981-16-0942-8, https://doi.org/10.1007/978-981-16-0942-8_50.
- [23] M. E. Shimpi, G. M. Deheri. Magnetic fluid based squeeze film in rough rotating curved porous annular plates: Deformation effect. *International Journal of Mathematical and Computational Sciences* **7**(8):1370–1380, 2013. <https://doi.org/10.5281/zenodo.1088604>.
- [24] N. C. Patel, J. R. Patel. Magnetic fluid-based squeeze film between curved porous annular plates considering the rotation of magnetic particles and slip velocity. *Journal of the Serbian Society for Computational Mechanics* **14**(2):69–82, 2020. <https://doi.org/10.24874/jsscm.2020.14.02.05>.
- [25] J.-R. Lin, R.-F. Lu, W.-H. Liao. Analysis of MHD squeeze film characteristics between curved annular plates. *Industrial Lubrication and Tribology* **56**(5):300–305, 2004. <https://doi.org/10.1108/00368790410550714>.
- [26] B. Kashinath, H. B. Nagangouda. MHD effect on porous wide composite slider bearing lubricated with a couplestress fluids. *Tribology Online* **10**(1):11–20, 2015. <https://doi.org/10.2474/trol.10.11>.
- [27] V. T. Morgan, A. Cameron. Mechanism of lubrication in porous metal bearings. In *Proceedings of the Conference on Lubrication and Wear, Institution of Mechanical Engineers*, pp. 151–157. London, 1957.
- [28] B. N. Hanumagowda, A. Salma. Study of squeeze film performance with MHD and couple stress between curved annular plates. *International Journal of Research and Analytical Reviews* **5**(3):669–676, 2018.
- [29] J. L. Gupta, K. H. Vora. Analysis of squeeze films between curved annular plates. *Journal of Lubrication Technology* **102**(1):48–50, 1980. <https://doi.org/10.1115/1.3251436>.

- [30] S. T. Fathima, N. B. Naduvinamani, B. N. Hanumagowda, J. S. Kumar. Modified Reynolds equation for different types of finite plates with the combined effect of MHD and couple stresses. *Tribology Transactions* **58**(4):660–667, 2015. <https://doi.org/10.1080/10402004.2014.981906>.
- [31] A. Król, B. Giemza, T. Kałdoński. The development of the lubricants applied in the porous bearings. *Journal of KONES Powertrain and Transport* **14**(3):311–317, 2007.

A. APPENDICES

$$A = \left\{ \frac{1 + (1 - 4M^2l^2/h_0^2)^{1/2}}{2} \right\}^{1/2}$$

$$B = \left\{ \frac{1 - (1 - 4M^2l^2/h_0^2)^{1/2}}{2} \right\}$$

$$g_{11} = \frac{A^2}{(A^2 - B^2)} \frac{\cosh \{B(2z - h)/2l\}}{\cosh(Bh/2l)}$$

$$g_{12} = \frac{B^2}{(A^2 - B^2)} \frac{\cosh \{A(2z - h)/2l\}}{\cosh(Ah/2l)}$$

$$g_{21} = \frac{2 \cosh \{(z - h)/\sqrt{2}l\} + 2 \cosh(z/\sqrt{2}l)}{2 \{ \cosh(\sqrt{2}l) + 1 \}}$$

$$g_{22} = \frac{(z/\sqrt{2}l) \sinh \{(z - h)/\sqrt{2}l\} + \{(z - h)/\sqrt{2}l\} \sinh(z/\sqrt{2}l)}{2 \{ \cosh(h/\sqrt{2}l) + 1 \}}$$

$$g_{31} = \frac{\cos B_2z \cosh A_2(z - h) + \cosh A_2z \cos B_2(z - h)}{\cosh A_2h + \cos B_2h}$$

$$g_{32} = \frac{\cot \theta \{ \sinh A_2z \sin B_2(z - h) + \sin B_2z \sinh A_2(z - h) \}}{\cosh A_2h + \cos B_2h}$$

$$A_2 = \sqrt{M/lh_0} \cos(\theta/2)$$

$$B_2 = \sqrt{M/lh_0} \sin(\theta/2)$$

$$\theta = \tan^{-1} \left(\sqrt{4l^2M^2/h_0^2 - 1} \right)$$

STONE TOPOGRAPHY – USEFUL TOOL IN MONUMENT RESTORATION PROCESS

MICHAL CIHLA^a, KATEŘINA KOVÁŘOVÁ^{b,*}, RICHARD MALÁT^b,
JAROSLAV VALACH^a

^a Czech Academy of Sciences, Institute of Theoretical and Applied Mechanics, Prosecká 809/76, 190 00 Prague 9, Czech Republic

^b Czech Technical University, Faculty of Civil Engineering, Thákurova 7, 166 29 Prague 6 – Dejvice, Czech Republic

* corresponding author: katerina.kovarova@fsv.cvut.cz

ABSTRACT. The surface of building stones on historic buildings often bears traces of the original craftsmanship. These are an integral part of the visual appearance of the monument and thus its value, which needs to be protected. For studying and identifying traces and subsequent reconstruction of stonemason's tools, we use the methods of traceology and mechanoscopy. Using modern imaging techniques, we can identify the stonemason's tool used, reconstruct the shape of its blade, and determine how it was used. The obtained results can be used in the process of monument care, especially in the process of preparation and implementation of restoration interventions on the objects, but they are also useful for completing the historical context of the monument. Our research is focused on a systematic study of the surface topography of stone monuments in Prague. The obtained results were systematically divided according to individual historical periods. As a model example of the use of the above-mentioned methods and approaches, we present the topography of stone elements and the development of stonemason's craft in Gothic Prague. The development of the stonemason's craft within one city in a given period can be documented on selected examples arranged chronologically in succession.

KEYWORDS: Stone topography, stonemason's tool, Gothic Prague.

1. INTRODUCTION

Topography is a discipline concerning the configuration of a surface, including its relief and the positions of its natural and artificial features. In common practice, we encounter topography in terms of shapes on the surface of the Earth or other celestial bodies. It deals, among other things, with their description, measurement, display, and mapping. In our case, however, we are talking about the topography of surfaces of much smaller scales whose formation is due to human activity [1]. Our object of interest is the surface topography of historical building stone that bears traces of historical craftsmanship. Each tool trace represents a valuable source of historical information. Each work is specific in its own way due to the unique pattern imprinted by the hands of the stonemason. From our extensive experience, we know that the traces on individual historic objects show, among other things, the influence of stonemason's workshops and local traditions. They also often reflect the economic and social conditions of the time e.g. [2]. Traces of working are also an integral part of the visual appearance of historic buildings and thus of their value, which needs to be protected. Within our project "Building stone surface topography and its application in the field of stone features restoration" Nr. DG20P02OVV021 founded by Ministry of Culture of the Czech Republic, we focused,

in particular, on the investigation of the craftsmanship of selected historical stone artefacts of the Prague Conservation Area, on which we identified working traces using traceologic and mechanoscopic methods. These methods allowed us to identify the traces of historical tools, create 3D models of them, and then identify and reconstruct the stonemason's tools used and the actual reconstruction of working with them. The obtained results can be used in the process of monument conservation, especially in the process of preparation and implementation of restoration interventions on given objects, however, they are also useful for completing the historical context of a given monument. The paper is, therefore, a summary of the results of our research in the field of documentation and identification of traces of historical craftsmanship. Like other crafts, the craft of stonemasonry has evolved over time and has been a subject, among other things, to fashion and social pressures. Some techniques are thus typical for certain historical periods, while others were rarely or never used in other periods. This fact can be used, for example, when dating disputed stone objects.

2. TRACEOLOGY OF TRACES AND THE TOOL USED

As we have already mentioned above, we use the methods of mechanoscopy and traceology for the iden-

tification of the traces themselves, on the basis of which we are able to reconstruct the tool and the working process itself. Both methods are based on forensic science and are used for criminal identification of traces. According to Mašková [3], mechanoscopy is based on expert knowledge of mechanics, physics and proven knowledge of the design and function of tools and instruments. It deals with the identification, way of use and mechanism of tools and other similar instruments. In criminalistics, traceological expertise deals with the examination of the traces themselves (e.g. the suspect's shoe prints). These traces can be either areal or volumetric. In our case, traceology deals with the blade of the tool itself, especially its shape, and in the case of analytical traceology, the identification of its metallic abrasions [4]. For this reason, this method is very popular in archaeology and related fields [5–7]. In addition to the analyses themselves, in traceology, there is a need to create a system of trace catalogues and also to make copies of supposed tools and to verify the excavated traces on them. The methods used in our traceological research are briefly described below.

2.1. RELIEF PHOTOGRAPHY

Relief photography is one of the important documentation photographic methods, where images of a given object are taken with lateral illumination. The light is set perpendicular to the processing traces, whereby each trace creates a shadow that highlights the corresponding raster. This method is primarily used for basic orientation on the surface of the stone being imaged. Photographs with direct illumination alone do not give any idea of the state of the surface working under examination. Lateral illumination can be achieved either with a steady light or with a flash. When adjusting the illumination intensity, it is necessary to pay attention to the illumination intensity so that the surface is not overexposed in the final photograph [4].

2.2. MECHANOSCOPY

The interpretation of data in terms of determining the actual trace is called mechanoscopy. The aim of this analysis is to identify tool traces, reconstruct the tools that produced them and outline the stone working process. As a result of the analyses, an attempt is made to reveal the process and working technique of the historical craftsmen in the making of the work concerned. Mechanoscopy works with 3D imaged materials, so it is necessary to create a 3D model of the object under study. Currently, two techniques are used for 3D modelling – laser scanning and photogrammetric scanning. For the purpose of our modelling, we use multi-frame photogrammetry. The basis of this method is spatial analytical geometry in a chosen coordinate system. First, we perform a focusing of the main points on the object to be photographed. The method of determining these points is trigonometric

calculations in the polar coordinate system. The azimuth height angles are determined using the camera, where the software calculates both angles from the position of the point on the sensor. The essential information is then the determination of the unknown position of the camera. This can be calculated by the software by creating a continuous strip of images with a minimum overlap of 50%. Once all the necessary data are obtained, a finer structure consisting of a triangular mesh can be constructed from the original point cloud. This is a simple approximation of the shape of the object. Such a mesh can then be replaced by the corresponding cutouts in the photograph [4].

The quality of photogrammetric imaging is mainly determined by the software and the quality of the sensor. The lens projects an image onto the sensor, which is made up of a mosaic of photocells called pixels. The sensor is essentially a photoelectric element that produces a voltage and corresponds to the intensity of light. The photocells are connected to a computer that is able to focus any photocell in X, Y coordinates. Ideally, the computer transfers the pixels in the matrix to memory, so that each memory cell should correspond to one X, Y pixel. In our case, however, everything depends mostly on the quality of the sensor. In practice, the sensor does not capture every pixel in X, Y, but with little intensity. Therefore, it helps itself significantly by sensing the immediate surroundings of the intensity of a given point. The result in the computer's memory is, therefore, not the intensity value of the X, Y point, but the arithmetic mean of its surroundings [8]. Laser scanning works on a similar principle, except that the scanning is done directly. The laser is emitted from a static head and oscillates on the object. Again, this is not a point focusing, but a numerical averaging of the point's surroundings. For this method, the distance of the sensor from the object is decisive. The greater the distance, the greater the oscillation of the laser. In manual scanning, the range of the beam is controlled by the camera system. However, if we have a good quality camera and lens, then the focus is at a high level, the area around the intensity of the point is reduced and the surface texture of the object is focused quite accurately. In contrast, with laser handheld scanners, where the scanning range of the laser is stable, there is a considerable blurring of the image detail. Such a method, therefore, precludes working in millimetre dimensions. Currently, photogrammetric examination of an object is significantly more suitable for mechanoscopy [9].

The photogrammetric documentation itself can be performed using a high quality, high resolution digital SLR camera, a fixed focal length lens and a set of lights that allow for a choice of directional and diffuse surface illumination. The lights themselves can be shone continuously or used in flash form. A 3D model of the surface with its topography is created from sets of photographs using Agisoft Photoscan Professional [11].

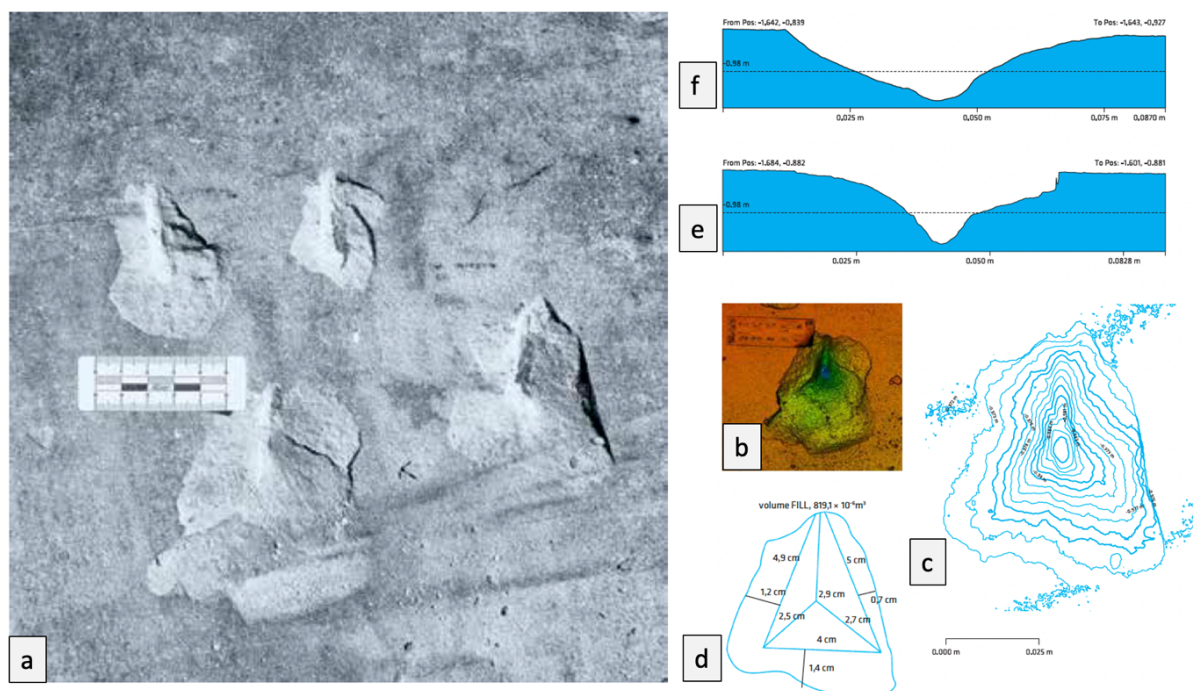


FIGURE 1. Experimental traces created by double-pick on the Mšeno sandstone (a), hypsometric image of the trace (b), its contour model (c) used to calculate the excavated volume (d), transverse height profile of the trace (e) and longitudinal height profile of the trace (f) (M. Cihla, adapted from [10]).

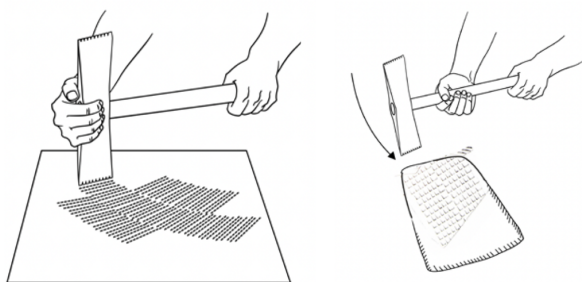


FIGURE 2. Traces of an almost perpendicular strike with an axe with flat pointed teeth (left), strikes with the same axe on a tilted face (drawing by A. Musilová, taken from [10]).

To study the surface sections and profiles, we use the Global Mapper software, in which the data are further processed using hypsometry or contouring. The selected trace is sectioned both longitudinally to determine the dynamics of the strike and transversally to generate the optimal shape of the tool blade (see Figure 1).

Every trace of a stonemason's tool found requires verification. This is only possible by experimenting with the tool itself. That is why there are copies of the stonemason's tools in question and attempts to imitate the way they work. Each work with a given tool has its own characteristics, which are reflected in the traces on the related surface (see Figure 2). The creation of a catalogue of historical stone processing traces is then the result of the knowledge of stonemason's ways of stone processing with tools in a historical context.

3. MODEL EXAMPLE – STONE PROCESSING OF GOTHIC PRAGUE

One of the main objectives of our research was a systematic study of the surface topography of the stone monuments of Prague. The obtained results were systematically divided according to the individual historical periods and clearly organised into a database [12]. As a model example of the use of the methods and approaches described above, let us consider the topography of stone elements and the development of stonemason craft in Gothic Prague.

Building activities in Prague during the 13th century continued the previous Romanesque architectural achievements [14]. The stone craftsmanship tradition continued to the full extent in the intentions of the so-called Prague School. Surface faces were cut in diagonally centred rasters, and the axe with a pick was still the most commonly used stone tool, just as in the Romanesque period. In the 1330s, a major building contract was ordered for the construction of a stone wall, part of the fortification of the Old Town. This monumental undertaking required not only an adequate quantity of material but also a change in the approach to its processing [13]. According to current knowledge, the material used in the construction of the wall, except for two short sections, was “opuka” [15]. This stone can be characterised as sandy-marly siltstones or sandy-silty marlstones or silicified marlstones and or marly silicites [16]. It was broken in so-called quarry “flatbreads” and then split into the necessary small blocks. The “opuka” building blocks were usually worked by stonemasons only on the load-



FIGURE 3. Old Town – Old Town Walls, between 1230 and 1253. Above, photo by M. Cihla, individual stages of working (drawing by A. Musilová, adapted from [13]).

ing surfaces, i.e. in the areas necessary for the stone to settle into the row. In this way, the common perimeter masonry was very simply designed. In contrast, the corner reinforcement of the tower walls was much more carefully manufactured in terms of craftsmanship [17]. The “opuka” blocks were of larger dimensions, around 30×30 cm. The tool traces testify to the fact that these blocks were first roughly modelled with the pick of a handled tool and then a circumferential path was made with a 1.5 cm wide straight-edged chisel. Finally, the surface was realigned in an oblique grid with a straight-bladed axe with a blade size of approximately 4 cm (see Figure 3).

The height of the stonemason’s craft in Prague at that time was the construction of the St. Agnes Monastery, whose first construction phase was completed with its consecration in 1234 [18]. This phase, which falls into the period of late Romanesque construction, prefigured a completely new trend that carried throughout the Middle Ages. It is clearly the

dominant use of toothed tools. The perimeter masonry of the Church of St Francis in the Convent of St Agnes still shows the receding approach typical of the Romanesque period, edging with a double-pick or other pointed handed tool and then resurfacing with an axe in areas of protruding material. In contrast, corner armatures and other architectural features are modelled with extreme precision using chisels or an axe with fine flat teeth. In architectural profiles, surface worked with toothed tools is also beginning to be used as a decorative grid (see Figure 4).

The orientation of stonemason’s work towards the straight-edged chisel, which reflected European trends, came in the late 15th and early 16th centuries. Rough stone modelling still used a pointed handed tool. The paths tend to be narrow, cut with a straight chisel, and in some cases, still visible. However, the final realignment of the face is always done in an angled grid, in parallel rows with a straight-bladed chisel. An example of such a precise work is the processing of the



FIGURE 4. Old Town – Agnes Monastery, refectory, after 1234. Surface processing with toothed tools in a decorative grid (photo by M. Cihla, taken from [13]).



FIGURE 5. Malá Strana – Malostranská Bridge Tower, 2nd half of the 15th century. Final realignment of the face in an oblique grid in parallel rows with a straight-edged chisel (photo by M. Cihla, taken from [13]).

blocks of the perimeter masonry of the Malostranska Bridge Tower (see Figure 5).

4. CONCLUSION

All of the above methods of surface working are more than typical and accompany the construction activity in the Gothic period. Like other crafts, stonemason craft developed and evolved over time. We have illustrated this development in the Prague Conservation Area with the example of the processing of Gothic stone elements. It is clear that the way of stone elements working and the traces of individual tools create the visual perception of a given monument and are indeed an integral part of its value. This value needs to be protected as a valuable part of the cultural and historical heritage. The use of new modern methods enables the precise identification of the tool traces, their reconstruction and even the reconstruction of the working process itself. The working process itself can also be seen as a cultural heritage of our ancestors. Furthermore, systematic research and documentation

of traces is an important source of information in the process of heritage conservation.

ACKNOWLEDGEMENTS

The presented work is carried out within project “Building stone surface topography and its application in the field of stone features restoration” and is supported by the program of applied research and development of national and cultural identity (NAKI) of the Ministry of Culture of the Czech Republic – grant No. DG20P02OVV021.

REFERENCES

- [1] The Science Dictionary. [2012-11-07], <https://www.thesciencedictionary.com/>.
- [2] M. Cihla, M. Tryml, L. Bartoš, et al. Stone surface finishing of selected Romanesque buildings. In *The Stone Prague. Topography of stone surface in the historic centre of Prague*, chap. 2.3. Institute of Theoretical and Applied Mechanics of the Czech Academy of Science, 2022. [in press].

- [3] N. Mašková. *Criminalistic expertise. (Kriminalistická expertiza [in Czech])*. Bachelor's thesis, University of Finance and Administration, 2019.
- [4] M. Cihla. Stoneworking (Traceology) and documentation options. In *The Stone Prague. Topography of stone surface in the historic centre of Prague*, chap. 1.4. Institute of Theoretical and Applied Mechanics of the Czech Academy of Science, 2022. [in press].
- [5] B. Molloy, M. Wiśniewski, M. Lynam, et al. Tracing edges: A consideration of the applications of 3D modelling for metalwork wear analysis on Bronze Age bladed artefacts. *Journal of Archaeological Science* **76**:79–87, 2016. <https://doi.org/10.1016/j.jas.2016.09.007>.
- [6] J. L. Adams. Ground stone use-wear analysis: a review of terminology and experimental methods. *Journal of Archaeological Science* **48**(1):129–138, 2014. <https://doi.org/10.1016/j.jas.2013.01.030>.
- [7] E. Girya, D. Fedorova, K. Stepanova, et al. Technical means and research perspectives in archeological traceology. *Stratum Plus* **1**:131–143, 2019.
- [8] M. Cihla. *Trasology in stone as a documentation method in selected Etruscan sites in the period 1st millennium BC. (Trasologie v kameni, jako dokumentační metoda ve vybraných etruských lokalitách v období 1. tisíciletí př.n.l. [in Czech])*. Bachelor's thesis, University of Jan Evangelista Purkyně in Ústí nad Labem, 2019.
- [9] I. Aicardi, F. Chiabrando, A. M. Lingua, F. Noardo. Recent trends in cultural heritage 3D survey: The photogrammetric computer vision approach. *Journal of Cultural Heritage* **32**:257–266, 2018. <https://doi.org/10.1016/j.culher.2017.11.006>.
- [10] M. Cihla. Identification of work traces and activities of the stonemason. Types of tools and their brief. In *The Stone Prague. Topography of stone surface in the historic centre of Prague*, chap. 1.6. Institute of Theoretical and Applied Mechanics of the Czech Academy of Science, 2022. [in press].
- [11] M. Cihla, J. Valach. Digital traceological and mechanoscopic methods in the study of the stone surface of historical objects. In *Digital Heritage. Progress in Cultural Heritage: Documentation, Preservation, and Protection*, pp. 482–488. Springer, 2020. https://doi.org/10.1007/978-3-030-73043-7_40.
- [12] M. Cihla, L. Bartoš, K. Kovářová, et al. Database of traces and reconstruction of historical stone tools. (Vzorník stop a rekonstrukce historických kamenických nástrojů [in Czech]). [2012-11-07], <https://stonetopography.is.cvut.cz>.
- [13] M. Cihla, M. Tryml, L. Bartoš, et al. Stone surface finishing of selected Gothic buildings. In *The Stone Prague. Topography of stone surface in the historic centre of Prague.*, chap. 3.5. Institute of Theoretical and Applied Mechanics of the Czech Academy of Science, 2022. [in press].
- [14] M. Cihla, K. Kovářová, M. Tryml, et al. Opracování stavebního kamene románských domů pražské podhradní aglomerace. *Staletá Praha* **37**(2):2–38, 2021.
- [15] M. Tryml. Poznámky k výstavbě opevnění Většího (Starého) Města pražského. *Časopis společnosti přátel starožitností* (2):65–73, 2020.
- [16] R. Lehr. Pläner: a traditional building stone in Saxo-Bohemian Cretaceous and Münsterland Cretaceous Basin. *Environmental Earth Sciences* volume **81**(7):219, 2022. <https://doi.org/10.1007/s12665-022-10218-x>.
- [17] Z. Dragoun. Stav a perspektivy poznání staroměstského opevnění. *Staletá Praha* **17**:39–70, 1987.
- [18] J. Soukupová. *Anežský klášter v Praze*. Second edition. Vyšehrad, 2011. xxi+463 p.

PARAMETRIC STUDY OF THE ENERGY POTENTIAL OF A BUILDING'S ENVELOPE WITH INTEGRATED ENERGY-ACTIVE ELEMENTS

DANIEL KALÚS^a, DANIELA KOUDELKOVÁ^a, VERONIKA MUČKOVÁ^a,
MARTIN SOKOL^a, MÁRIA KURČOVÁ^a, PATRIK ŠŤASTNÝ^{b,*}

^a Slovak University of Technology in Bratislava, Faculty of Civil Engineering, Department of Building Services, Radlinského 11, 810 05 Bratislava, Slovakia

^b Slovak University of Technology in Bratislava, Faculty of Civil Engineering, Department of Building Technology, Radlinského 11, 810 05 Bratislava, Slovakia

* corresponding author: patrik.stastny@stuba.sk

ABSTRACT.

Building structures with integrated energy-active elements (BSIEAE) present a progressive alternative for building construction with multifunctional energy functions. The aim was to determine the energy potential of a building envelope with integrated energy-active elements in the function of direct-heating, semi-accumulation and accumulation of large-area radiant heating. The research methodology consists in an analysis of building structures with energy-active elements, creation of mathematical-physical models based on the simplified definition of heat and mass transfer in radiant large-area heating, and a parametric study of the energy potential of individual variants of technical solutions. The results indicate that the increase in heat loss due to the location of the tubes in the structure closer to the exterior is negligible for Variant II, semi-accumulation heating, and Variant III, accumulation heating, as compared to Variant I, direct heating, it is below 1 % of the total delivered heat flux. The direct heat flux to the heated room is 89.17 %, 73.36 %, and 58.46 % of the total heat flux for Variant I, Variant II and Variant III, respectively. For Variant II and Variant III, the heat storage accounts for 14.84 %, and 29.86 % of the total heat flux, respectively. Variants II and III appear to be promising in terms of heat/cool accumulation with an assumption of lower energy demand (at least 10 %) than for low inertia walls. We plan to extend these simplified parametric studies with dynamic computer simulations to optimise the design and composition of the panels with integrated energy-active elements.

KEYWORDS: Building Structures with Integrated Energy-Active Elements (BSIEAE), Active Thermal Protection (ATP), Thermal Barrier (TB), Large-Scale Radiant Heating/Cooling (LSRHC), Heat/Cool Accumulation (HCA), Absorption of Solar and Ambient Energy, Thermally Activated Building Structure (TABS).

1. INTRODUCTION

Mass production of prefabricated panels and standardised building modules with integrated energy-active elements represents a variant of building construction with advantages in the form of fast assembly of building objects with combined building-energy systems without significant technological downtime, higher economic efficiency, high potential for the use of renewable energy sources (RES) and waste heat. These facts inspire and motivate us to research different variants of technical solutions of self-supporting panels with an internal energy source, active thermal protection (ATP), which we have described in the utility model SK5729 Y1 [1], thermal insulation panels for systems with active heat transfer control in utility model SK5725 Y1 [2], and in the European patent EP 2 572 057 B1 “Heat insulating panel with active regulation of heat transition” [3].

Active thermal protection (ATP) is a dynamic process characteristic of building structures with integrated energy-active elements characterised by one or more functions in different energy systems' operation modes. The energy functions of ATP are a thermal barrier, large-scale radiant low-temperature heating/high-temperature cooling, heat/cold storage, solar and ambient energy capture, heat/cold recovery, heat recovery, etc. This study aims to determine the energy potential of a building envelope with integrated energy-active elements in the function of direct-fired, semi-accumulation (TABS system), and accumulation of large-area radiant heating.

2. CURRENT SITUATION

Various designs of prefabricated panels and standardised building modules with integrated energy-active elements are known. According to the energy function, building structures with active thermal protection (ATP) are divided into:

- building structures with large-scale radiant low-temperature heating or high-temperature cooling (BSHC) function, Figure 1,
- building structures with thermally activated building structure (TABS) function, Figure 2,

FUNCTIONALITY

The functional modules get arranged to each other in order to create a variety of individual space or living solutions.

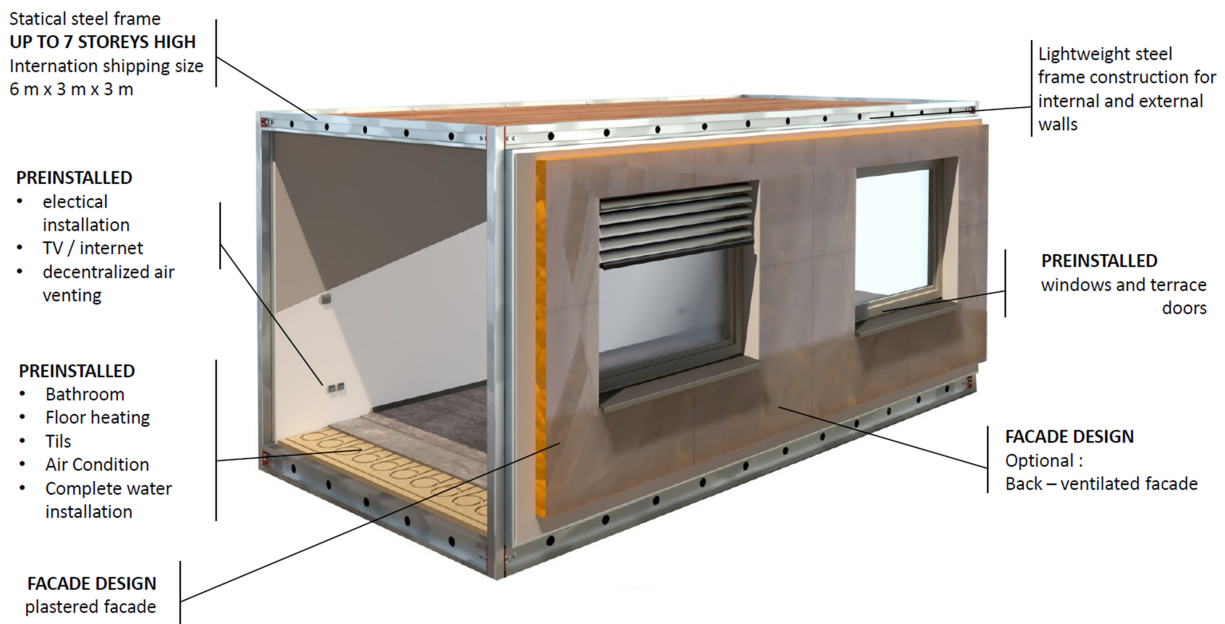


FIGURE 1. Standardised SUNOMAXCUBE building module with integrated energy-active elements in the building structures [4].

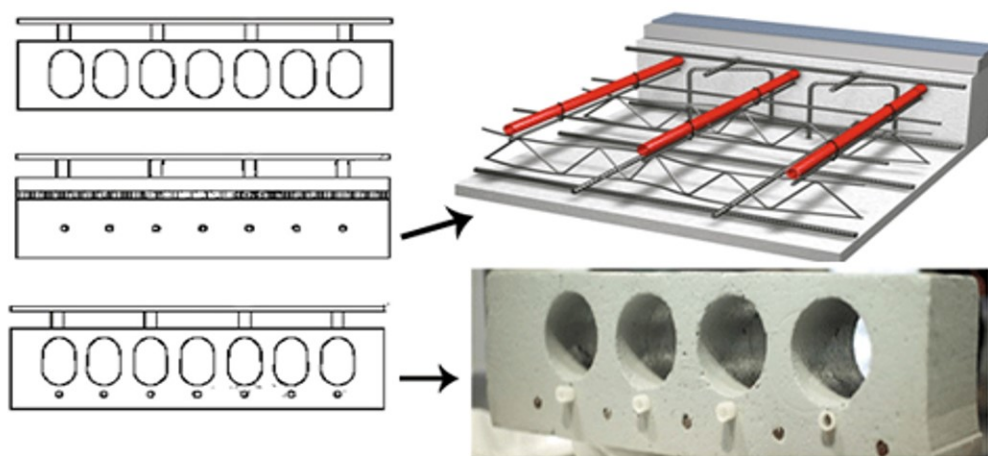


FIGURE 2. Division of TABS according to the position of the heat transfer medium: In the upper part: the heat transfer medium is air distributed through the cavities in the ceiling panel, in the middle: the heat transfer medium is a liquid in a pipe – monolithic ceiling, in the lower part: the heat transfer medium is a liquid in a pipe – prefabricated ceiling panel [5].

- building structures with thermal barrier function (TB), Figure 3,
- building structures with an absorber (BSA) built into the building structure on the outside of the building envelope to capture solar or ambient energy in synergy with heat pumps, Figure 4,
- building structures with combined energy functions (BSCE), Figure 5.

Figure 1 shows a standardised SUNOMAXCUBE building module with integrated energy-active elements in the building structures [4]. One of the pre-installed energy systems is a large-area low-temperature radiant floor heating [6].

Thermally activated building structures (TABS) can also implement large-scale, low-temperature heating and high-temperature cooling. The term 'thermally activated parts' is used for structures in which the flow of a heat transfer fluid heats or cools the entire structure, and consequently the surrounding spaces. They are also called hybrid systems since building structures have started to be used as heat exchange surfaces. These systems operate at a small temperature difference between the temperature of the heat transfer fluid and the surrounding space, allowing them to use low-temperature energy sources. TABS are made up of structures characterised by high density, and weight (walls, ceilings, columns...) and equipped with cavities for air circulation, pipes for water circulation, or pipes embedded in the monolithic ceilings of multi-story buildings, Figure 2.



FIGURE 3. Left and centre – ISOMAX thermal barrier (TB) perimeter panel made of lost-foam expanded polystyrene formwork, on the right – panels comprehensively manufactured in the panel factory [7].

ISOMAX perimeter panels with an integrated thermal barrier (TB) consist of a lost-foam expanded polystyrene formwork containing a steel reinforcing mesh with piping, Figure 3. Usually, their internal space is filled with a cast-in-place concrete mix only after they have been placed on site. In the next stage, the concrete must cure and reach the required strength (approx. 28 days). This construction technique is called 'wet construction'. This is only applied in new buildings. Alternatively, the production of these panels can be carried out comprehensively in a prefabrication plant [7].

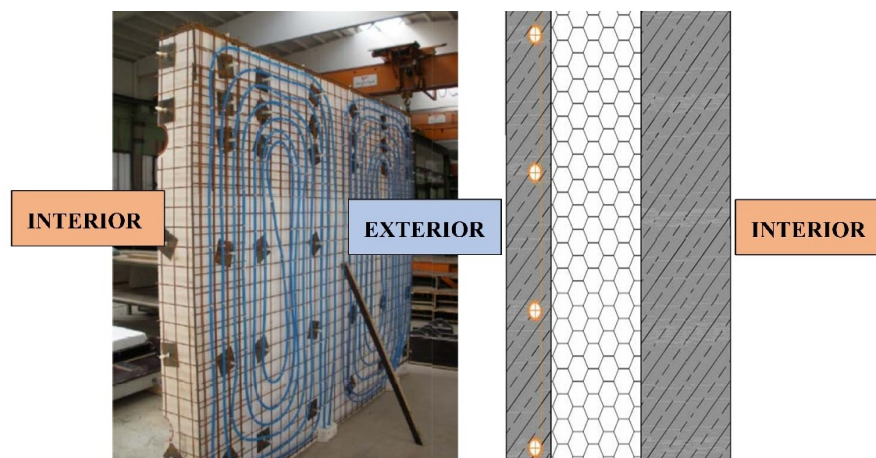


FIGURE 4. Single-pipe combined energy wall system with massive absorber [8].

One of the variants of building structures with absorber function embedded in the building structure on the exterior side of the building envelope used to capture solar or ambient energy in synergy with heat pumps is

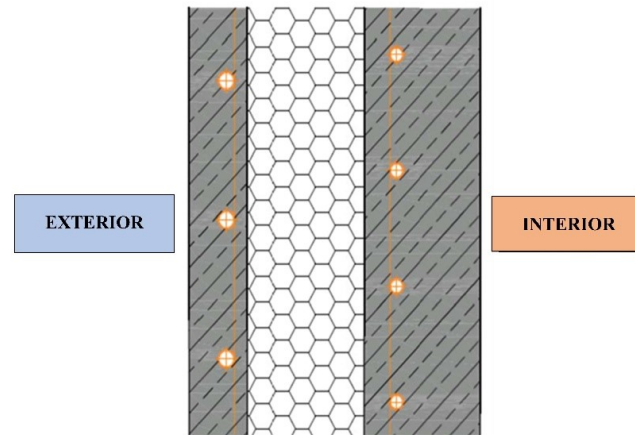


FIGURE 5. Double-pipe combined energy wall system with massive absorber [8].

shown in Figure 4. The composition of the wall structure is precisely defined. The first design solution used in practice is a wall with a reinforced concrete massive absorber (MA) on the outside, in which a plastic pipe is embedded [8]. The inner reinforced concrete core is separated from the massive absorber by a polyurethane foam layer separating the two reinforced concrete slabs. It is a polyurethane core that is sheathed on both sides with reinforced concrete. The single-walled combined energy wall system with a solid absorber is primarily used to capture energy from the exterior for further use with a heat pump. In theory, this system should also recover heat from the interior (without the use of a heat pump).

The two-tube combined energy wall system with a massive RIEDER absorber [8], Figure 5, is an improved version of the single-tube system, shown in Figure 4, by adding the energy functions of low-temperature heating and high-temperature cooling. The composition of the wall structure is well defined. The first design solution used in practice is a wall with a reinforced concrete massive absorber (MA) on the outside, in which a plastic pipe is embedded. The inner reinforced concrete core is separated from the MA by a layer of polyurethane foam which separates the two reinforced concrete slabs. It is a polyurethane core that is sheathed on both sides with reinforced concrete. In the inner reinforced concrete core, a plastic pipe is encased, which is used for heating and cooling. This system is also still in the experimental verification stage. It is envisaged that the massive absorber (MA) should capture heat from the exterior and serve as the primary circuit for the heat pump. The theoretical assumption is that the system should not only collect heat from the exterior but also recuperate the heat that spreads from the interior without the aid of the heat pump. The system will only be suitable for practical use if it absorbs more energy than the electrical energy required to drive the heat pump and circulators. The internal piping is used for the interior's low-temperature heating and high-temperature cooling.

Many researchers from all over the world have been involved in the analysis of building structures with integrated energy-active elements. We provide references to some of the main scientific studies in this area of research [9–25].

3. METHODOLOGY

The aim of this paper is a parametric study of the energy potential of precast reinforced concrete building envelope panels with integrated energy active elements in three energy functions, viz:

- direct heating; large-scale radiant low-temperature heating, VARIANT I,
- semi-accumulative (TABS system), VARIANT II,
- accumulation; large area radiant low-temperature heating, VARIANT III.

Based on the analysis of building structures with energy-active elements, Section 2, we have developed mathematical-physical models for selected variants of technical solutions of the panels based on a simplified definition of heat and mass transfer in radiant large-area heating, Figure 6–8. The parametric study of the energy potential of the different variants of the technical solutions is based on a simplified calculation according to [26–28]. In building structures with ATP, heat transfer is combined by convection and radiation. The heat exchange occurs on the inner and outer surfaces of the building structure. On the inside of the building structure, the following occurs:

- airflow, as the air is warmer in the higher positions and colder in the lower positions,
- radiation because of the heat exchange of a given structure with all other room structures.

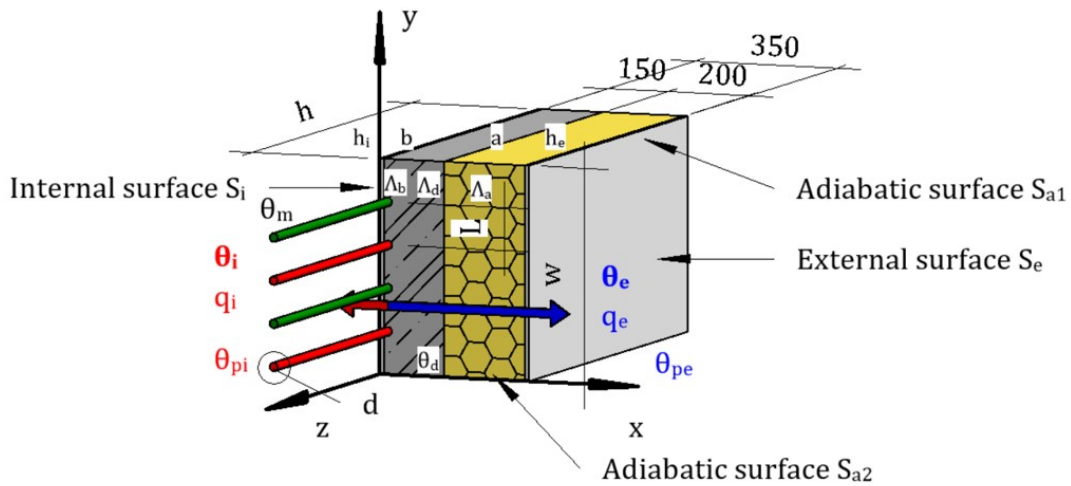


FIGURE 6. VARIANT I: Mathematical-physical model of a wall with integrated energy-active elements in the function of direct heating and cooling.

q_i – heat flow towards the interior [W m^{-2}], q_e – heat flow towards the exterior [W m^{-2}], θ_i – inside air temperature [$^{\circ}\text{C}$], θ_e – outside air temperature [$^{\circ}\text{C}$], θ_{pi} – interior surface temperature [$^{\circ}\text{C}$], θ_{pe} – exterior surface temperature [$^{\circ}\text{C}$], L – an axial distance of pipes [m], d – pipe diameter [m], Λ_a – thermal permeability of the layer in front of the pipes towards the interior [$\text{W (m}^2 \text{K)}^{-1}$], Λ_d – thermal conductivity of the pipe material [$\text{W (m}^2 \text{K)}^{-1}$], θ_d – the average temperature of the structure in the axis of the pipes [$^{\circ}\text{C}$], θ_m – average heating water temperature [$^{\circ}\text{C}$], h_i – heat transfer coefficient towards the interior, h_e – heat transfer coefficient towards the exterior, a – thickness of the layer in front of the pipes [m], b – thickness of the layer behind the pipes [m].

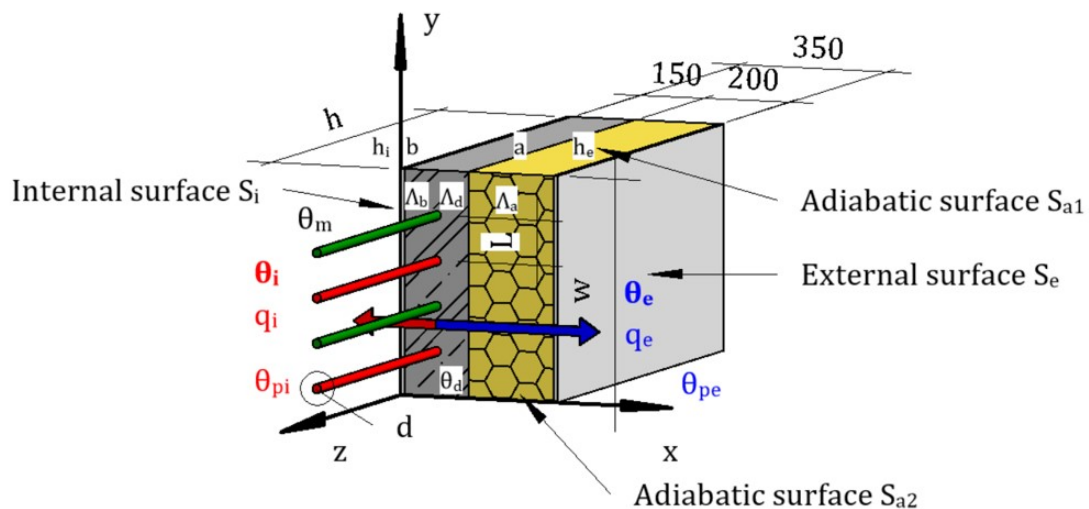


FIGURE 7. VARIANT II: Mathematical-physical model of a wall with an internal energy source located in the centre of the load-bearing part of a reinforced concrete panel, semi-accumulation heating and cooling, TABS system.

q_i – heat flow towards the interior [W m^{-2}], q_e – heat flow towards the exterior [W m^{-2}], θ_i – inside air temperature [$^{\circ}\text{C}$], θ_e – outside air temperature [$^{\circ}\text{C}$], θ_{pi} – interior surface temperature [$^{\circ}\text{C}$], θ_{pe} – exterior surface temperature [$^{\circ}\text{C}$], L – an axial distance of pipes [m], d – pipe diameter [m], Λ_a – thermal permeability of the layer in front of the pipes towards the interior [$\text{W (m}^2 \text{K)}^{-1}$], Λ_b – thermal permeability of the layer behind the pipes towards the exterior [$\text{W (m}^2 \text{K)}^{-1}$], Λ_d – thermal conductivity of the pipe material [$\text{W (m}^2 \text{K)}^{-1}$], θ_d – the average temperature of the structure in the axis of the pipes [$^{\circ}\text{C}$], θ_m – average heating water temperature [$^{\circ}\text{C}$], h_i – heat transfer coefficient towards the interior, h_e – heat transfer coefficient towards the exterior, a – thickness of the layer in front of the pipes [m], b – thickness of the layer behind the pipes [m].

On the outside of the building structure, there is:

- airflow mostly along with the structure due to wind,
- diffuse sky radiation acting on the building's surface, and the heat exchange between surrounding buildings and terrain [29].

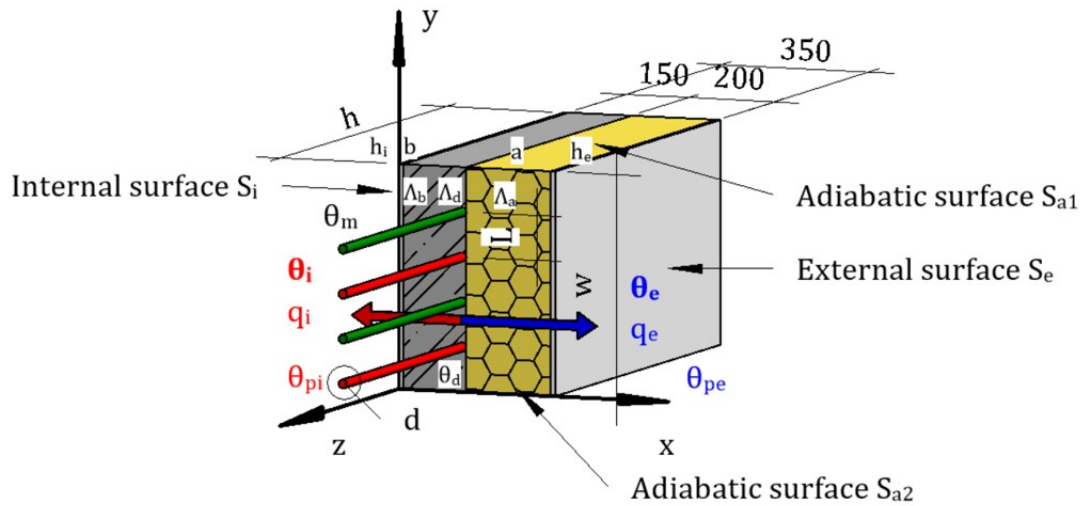


FIGURE 8. VARIANT III: Mathematical-physical model of a wall with integrated energy-active elements located at the interface between the load-bearing part and the thermal insulation part of the reinforced concrete panel, accumulation heating, and cooling system.

q_i – heat flow towards the interior [W m^{-2}], q_e – heat flow towards the exterior [W m^{-2}], θ_i – inside air temperature [$^{\circ}\text{C}$], θ_e – outside air temperature [$^{\circ}\text{C}$], θ_{pi} – interior surface temperature [$^{\circ}\text{C}$], θ_{pe} – exterior surface temperature [$^{\circ}\text{C}$], L – an axial distance of pipes [m], d – pipe diameter [m], Λ_a – thermal permeability of the layer in front of the pipes towards the interior [$\text{W (m}^2 \text{K)}^{-1}$], Λ_b – thermal permeability of the layer behind the pipes towards the exterior [$\text{W (m}^2 \text{K)}^{-1}$], Λ_d – thermal conductivity of the pipe material [$\text{W (m}^2 \text{K)}^{-1}$], θ_d – the average temperature of the structure in the axis of the pipes [$^{\circ}\text{C}$], θ_m – average heating water temperature [$^{\circ}\text{C}$], h_i – heat transfer coefficient towards the interior, h_e – heat transfer coefficient towards the exterior, a – thickness of the layer in front of the pipes [m], b – thickness of the layer behind the pipes [m].

To calculate the heat flux q [W m^{-2}] from ATP, we followed the procedure of [26–28]. The average temperature of the structure in the axis of the pipes:

$$\theta_d - \theta_i = (\theta_m - \theta_i) \cdot \frac{\tanh\left(m\frac{L}{2}\right)}{m\frac{L}{2}}, \tag{1}$$

where:

- θ_d the average temperature of the structure in the axis of the pipes [$^{\circ}\text{C}$],
- θ_i internal design temperature [$^{\circ}\text{C}$],
- θ_m average heating water temperature [$^{\circ}\text{C}$],
- L axial distance of pipes [m],
- m coefficient characterising the heating plate in terms of heat dissipation [m^{-1}] [26–28].

Coefficient characterising the heating plate in terms of heat dissipation:

$$m = \sqrt{\frac{2 \cdot (\Lambda_a + \Lambda_b)}{\pi^2 \lambda_d d}}, \tag{2}$$

where:

- m coefficient characterising the heating plate in terms of heat dissipation [m^{-1}],
- Λ_a thermal permeability of the layer in front of the pipes towards the interior [$\text{W (m}^2 \text{K)}^{-1}$],
- Λ_b thermal permeability of the layer behind the pipes towards the exterior [$\text{W (m}^2 \text{K)}^{-1}$],
- λ_d thermal conductivity of the material into which the tubes are inserted [W (m K)^{-1}],
- d pipe diameter [m] [26–28].

Thermal permeability of the layer in front of the pipes towards the interior:

$$\Lambda_a = \sqrt{\frac{1}{\sum \frac{a}{\lambda_a} + \frac{1}{h_i}}}. \tag{3}$$

Thermal permeability of the layer behind the pipes towards the exterior:

$$\Lambda_a = \sqrt{\frac{1}{\sum \frac{b}{\lambda_b} + \frac{1}{h_e}}}, \quad (4)$$

where:

- Λ_a thermal permeability of the layer in front of the pipes towards the interior [$\text{W (m}^2 \text{K)}^{-1}$],
- Λ_b thermal permeability of the layer behind the pipes towards the exterior [$\text{W (m}^2 \text{K)}^{-1}$],
- a thickness of the layer in front of the pipes [m],
- b thickness of the layer behind the pipes [m],
- λ_a, λ_b thermal conductivity of the material of the respective layer [W (m.K)^{-1}],
- h_i heat transfer coefficient towards the interior [$\text{W (m}^2 \text{K)}^{-1}$],
- h_e heat transfer coefficient towards the exterior [$\text{W (m}^2 \text{K)}^{-1}$] [26–28].

The average surface temperature of the structure θ_p [$^{\circ}\text{C}$]:

$$\theta_{pi} - \theta_i = \frac{\Lambda_a}{h_i} \cdot (\theta_d - \theta_i) = \frac{\lambda_a}{h_i} \cdot (\theta_m - \theta_i) \cdot \frac{\tanh\left(\frac{mL}{2}\right)}{m\frac{L}{2}}, \quad (5)$$

where:

- θ_{pi} the average surface temperature of the structure [$^{\circ}\text{C}$],
- θ_d the average temperature of the structure in the axis of the pipes [$^{\circ}\text{C}$],
- θ_i internal design temperature [$^{\circ}\text{C}$],
- θ_m average heating water temperature [$^{\circ}\text{C}$],
- Λ_a thermal permeability of the layer in front of the pipes towards the interior [$\text{W (m}^2 \text{K)}^{-1}$],
- Λ_b thermal permeability of the layer behind the pipes towards the exterior [$\text{W (m}^2 \text{K)}^{-1}$],
- h_i heat transfer coefficient towards the interior [$\text{W (m}^2 \text{K)}^{-1}$],
- L axial distance of pipes [m],
- m coefficient characterising the heating plate in terms of heat dissipation [m^{-1}] [26–28].

Specific heat output (flow) from the structure towards the interior:

$$q_i = \Lambda_a \cdot (\theta_d - \theta_i) = \alpha_p \cdot (\theta_p - \theta_i), \quad (6)$$

and specific heat output (flow) from the structure towards the exterior:

$$q_e = \Lambda_b \cdot (\theta_d - \theta_i) = \Lambda_b \cdot \frac{h_i}{\Lambda_a} \cdot (\theta_{pi} - \theta_i) + \Lambda_b \cdot (\theta_i - \theta_e) \quad (7)$$

where:

- q_i heat flux from the structure towards the interior [W m^{-2}],
- q_e heat flux from the structure towards the exterior [W m^{-2}],
- θ_{pi} the average surface temperature of the structure [$^{\circ}\text{C}$],
- θ_d the average temperature of the structure in the axis of the pipes [$^{\circ}\text{C}$],
- θ_i calculated internal room temperature [$^{\circ}\text{C}$],
- θ_e calculated external temperature [$^{\circ}\text{C}$],
- Λ_a thermal permeability of the layer in front of the pipes towards the interior [$\text{W (m}^2 \text{K)}^{-1}$],
- Λ_b thermal permeability of the layer behind the pipes towards the exterior [$\text{W (m}^2 \text{K)}^{-1}$],
- h_i heat transfer coefficient towards the interior [$\text{W (m}^2 \text{K)}^{-1}$] [26–28].

4. RESULTS AND DISCUSSION

Based on the analysis of building structures with energy-active elements, Section 2, the developed mathematical-physical models, and the simplified calculation procedure according to [26–28], Section 3, we have developed an application calculator in Excel. We then calculated the following values for panel variants I, II, and III:

- θ_d average design temperature in the pipe axis [$^{\circ}\text{C}$],
- θ_{pi} average surface temperature of the structure in the interior [$^{\circ}\text{C}$],

- q_i heat flux from the structure towards the interior [W m^{-2}],
- q_e heat flux from the structure towards the exterior [W m^{-2}].

The calculation was conducted for a heating season. Boundary conditions include the following: the thickness of the reinforced concrete bearing part of the panel $b_{\text{panel}} = 150 \text{ mm}$; thickness of the thermal insulation $b_{TI} = 200 \text{ mm}$; outer dimension of the ATP pipe $d = 15 \text{ mm}$; distance between pipes $L = 0.150 \text{ m}$; heat transfer coefficient h_p towards the interior $h_p = 10 \text{ W (m}^2 \text{ K)}^{-1}$ (according to EN 15377-1 [30] and STN 73 0540-2+Z1+Z2 [31]). According to [26–28], the average design temperature along the pipe’s axis and the average surface temperature were calculated using simplified calculation relations that took into account the identical wall mass temperature in front of and behind the pipe. Figure 9 and Table 1 show the outcomes of the calculations for the heating period. The temperatures that were taken into account were the average working medium temperature in the ATP pipe $\theta_m = 30 \text{ }^\circ\text{C}$, the outside air temperature $\theta_e = -11 \text{ }^\circ\text{C}$, and the internal air temperature $\theta_i = 20 \text{ }^\circ\text{C}$.

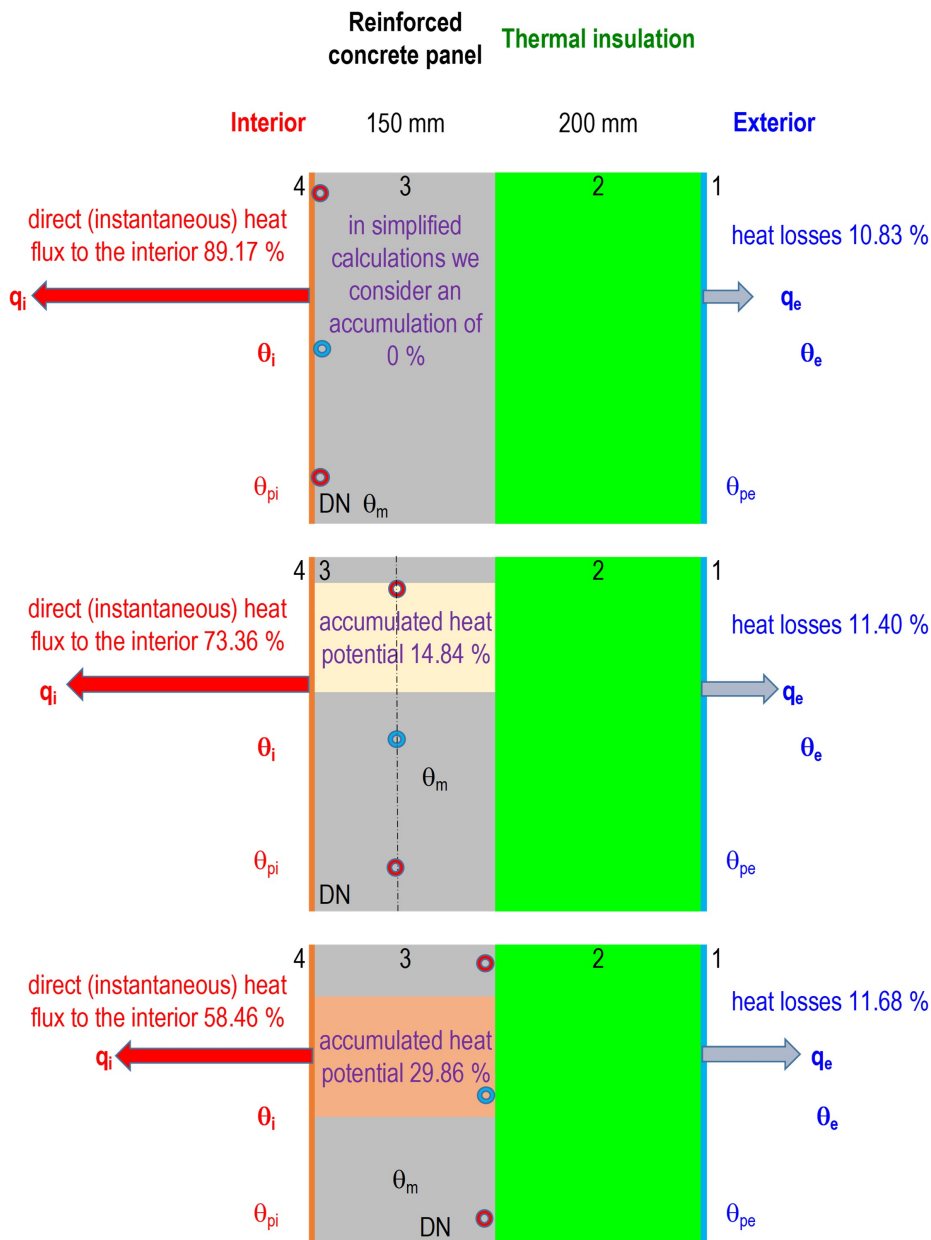


FIGURE 9. Heat flux analysis of the investigated variants of mathematical-physical models of perimeter reinforced concrete panels.

q_i – heat flow towards the interior [W m^{-2}], q_e – heat flow towards the exterior [W m^{-2}], θ_i – inside air temperature [$^\circ\text{C}$], θ_e – outside air temperature [$^\circ\text{C}$], θ_{pi} – interior surface temperature [$^\circ\text{C}$], θ_{pe} – exterior surface temperature [$^\circ\text{C}$].

Marginal conditions																
Interior temperature θ_i [°C]	20	Classic large-area radiant heating	7.984	0.176	25.4855	54.854	6.663	61.517	0.000	61.517	10.83 %	10.83 %	100.00 %	0.00 %	0.00 %	Thermal transmittance behind/below the pipes towards the exterior Λ_a ($\text{W (m}^2 \text{K)}^{-1}$)
Exterior temperature θ_e [°C]	-11															Thermal transmittance behind/below the pipes towards the exterior Λ_b ($\text{W (m}^2 \text{K)}^{-1}$)
Mean temperature of the heat transfer medium θ_m [°C]	30															Surface temperature θ_p (°C)
Heat transfer coefficient before/above pipes to interior h_{pi} [$\text{W (m}^2 \text{K)}^{-1}$]	10	Thermally Activated Building Systems (TABS)	6.152	0.183	24.538	45.378	7.012	52.390	9.127	61.517	13.38 %	11.40 %	85.16 %	4.97 %	0.57 %	Direct (instantaneous) heat flux to interior q_i (W m^{-2})
Heat transfer coefficient behind the pipes to the exterior h_{pe} [$\text{W (m}^2 \text{K)}^{-1}$]	7															Direct (instantaneous) heat flux to exterior q_e (W m^{-2})
Thermal conductivity coefficient TI λ [W/(mK)]	0.037															Total direct (instantaneous) heat flux q_{direct} (W m^{-2})
Pipe spacing L [mm]	150	Active thermal protection (ATP)	4.542	0.185	23.596	35.963	7.186	43.149	18.368	61.517	16.65 %	11.68 %	70.14 %	7.28 %	0.85 %	Accumulated heat flux in the building structure $q_{\text{accumulation}}$ (W m^{-2})
Pipe diameter [mm]	15															Total delivered heat flux q_{total} (W m^{-2})
Thermal insulation thickness (TI) [mm]	200															ratio of direct (instantaneous) heat flux to the exterior to the total direct (instantaneous) heat flux (%)
																ratio of direct (instantaneous) heat flux to the exterior (instantaneous) heat flux to the exterior to the total delivered heat flux (%)
																Comparison of direct (instantaneous) heat flux to the interior with conventional large area radiant heating (%)
																Increase in losses of direct (instantaneous) heat flux to the exterior to losses to the exterior of conventional large area radiant heating (%)
																Increase in losses of direct (instantaneous) heat flux to the exterior to the total delivered heat flux (%)

TABLE 1. Partial results of the parametric study from the comparison of 3 variants of mathematical-physical models of panel design solutions.

In the parametric study of the stationary state based on mathematical-physical models and the analysis of the energy potential of the subject variants of panels with integrated energy-active elements, we considered heat and mass transfer with theoretical simplifications. For the panel with direct-fired large-area radiant heating, Variant I, we do not consider the accumulation of the delivered heat flux in the mass of the building structure. Table 1 shows the partial results from the parametric study, where all 3 variants of the mathematical-physical models of the panel design solutions are compared.

For thermal insulation in the thickness range of 50–100 mm, the heat flux to the interior q_i [W m^{-2}] increases while the heat loss q_e [W m^{-2}] decreases rapidly. For thicknesses above 100 mm, the effect of adding more insulation becomes relatively small. This is true regardless of the thickness of the concrete core, which has almost no effect on the heat flux. Conversely, the effect of pipe spacing on the heating performance is evident; despite the small effect on the heat flux to the interior, increasing the thickness of the concrete, and hence the inertia of the wall, can reduce the energy demand for heating [32]. For a system with a pipe embedded in a solid concrete core, the storage capacity, which is defined as a time constant, can range from roughly 2.5 to over 8 hours [33]. N. Aste, A. Angelotti, and M. Buzzetti, for instance, claim that in Milan, Italy, high-inertia walls can have an energy demand that is up to 10% lower than low-inertia walls. S.A. Al-Sanea, M.F. Zedan, and S.N. Al-Hussain computed a reduction in energy demand for increasing wall thickness and heating energy savings of up to 35% owing to thermal mass optimisation for the climate of Riyadh, Saudi Arabia [34]. In other research [35–37], the significance of concrete thickness for the thermal dynamics of buildings is highlighted. This importance must be taken into account when designing a new structure, a restoration, or a control system.

Based on the analysis of the energy potential of the various technical solutions for the envelope panels with integrated energy-active elements, it can be said that the increase in heat losses caused by the tubes' placement in the structure being closer to the exterior for Variant II, semi-accumulation heating (TABS system), and Variant III, accumulation heating, in comparison to Variant I, direct heating, is negligible, below 1% of the total delivered heat flux, Table 1 and Figure 9.

Of the total supplied heat flux shown in Table 1 and Figure 9, the direct heat flux to the heated room is 89.17% for direct heating, 73.36% for semi-accumulation heating (TABS system), and 58.46% for accumulation heating for Variant III.

VARIANT I ignores heat accumulation in favour of the panel's simplicity. According to Table 1 and Figure 9, Variant II represents 14.84% and Variant III up to 29.86% of the total supplied heat flux for the panel design (TABS system).

5. CONCLUSIONS

Variants II and III appear promising in heat/cool accumulation with an assumption of lower energy demand (at least 10%) than for low inertia walls. We plan to extend these simplified parametric studies with dynamic computer simulations to optimise the design and composition of panels with integrated energy-active elements.

Research in building structures with integrated energy-active elements brings many inspirations, innovations, and completely new sustainable technical solutions that point to a high potential for energy savings, increased economic efficiency, and environmental friendliness. The predetermination of these building structures for the application of renewable energy sources and waste heat represents an energy-secure and self-sufficient technical solution as a fully-fledged alternative to energy systems dependent on fossil fuels.

ACKNOWLEDGEMENTS

This research was supported by the Ministry of education, Science, Research and Sport of the Slovak republic grant VEGA 1/0304/21. This research was supported by the Ministry of education, Science, Research and Sport of the Slovak republic grant KEGA 005STU-4/2021.

LIST OF SYMBOLS

ATP Active Thermal Protection

BSA Building structures with an absorber

BSCE Building structures with combined energy functions

BSIEAE Building structures with integrated energy-active elements

BSHC Building structures with large-scale radiant low-temperature heating or high-temperature cooling

EP European patent

HCA Heat/cool accumulation

LSRHC Large-scale radiant heating/cooling

MA Massive absorber

RES Renewable Energy Sources

TABS Thermally Activated Building Structure

TB	Thermal Barrier
TI	Thermal insulation
a	Thickness of the layer in front of the pipes [m]
b	Thickness of the layer behind the pipes [m]
d	Pipe diameter [m]
h_e	Heat transfer coefficient towards the exterior [$\text{W}(\text{m}^2 \text{K})^{-1}$]
h_i	Heat transfer coefficient towards the interior [$\text{W}(\text{m}^2 \text{K})^{-1}$]
L	Axial distance of pipes [m]
m	Coefficient characterising the heating plate in terms of heat dissipation [m^{-1}]
q	The heat flux [W m^{-2}]
q_i	Heat flow towards the interior [W m^{-2}]
q_e	Heat flow towards the exterior [W m^{-2}]
θ_d	The average temperature of the structure in the axis of the pipes [$^{\circ}\text{C}$]
θ_e	Outside air temperature [$^{\circ}\text{C}$]
θ_i	Inside air temperature [$^{\circ}\text{C}$]
θ_m	Average heating water temperature [$^{\circ}\text{C}$]
θ_{pi}	Interior surface temperature [$^{\circ}\text{C}$]
θ_{pe}	Exterior surface temperature [$^{\circ}\text{C}$]
Λ_a	Thermal permeability of the layer in front of the pipes towards the interior [$\text{W}(\text{m}^2 \text{K})^{-1}$]
Λ_b	Thermal permeability of the layer behind the pipes towards the exterior [$\text{W}(\text{m}^2 \text{K})^{-1}$]
Λ_d	Thermal conductivity of the pipe material [$\text{W}(\text{m}^2 \text{K})^{-1}$]
λ_a, λ_b	Thermal conductivity of the material of the respective layer [$\text{W}/(\text{m K})$]
λ_d	Thermal conductivity of the material into which the tubes are inserted [$\text{W}/(\text{m K})$]

REFERENCES

- [1] D. Kalús, P. Páleš, L. Pelachová. Samonosný tepelnoizolačný panel pre systémy s aktívnym riadením prechodu tepla. [Self-supporting thermal insulation panel for systems with active heat transfer control.] (Utility model No. SK 5729 Y1). Úrad priemyselného vlastníctva Slovenskej republiky, 2011. [2022-08-13], <https://wbr.indprop.gov.sk/WebRegistre/UzitkovyVzor/Detail/5030-2010>.
- [2] D. Kalús, P. Páleš, L. Pelachová. Tepelnoizolačný panel pre systémy s aktívnym riadením prechodu tepla. [Thermal insulation panel for systems with active heat transfer control.] (Utility model No. SK 5725 Y1). Úrad priemyselného vlastníctva Slovenskej republiky, 2011. [2022-08-13], <https://wbr.indprop.gov.sk/WebRegistre/UzitkovyVzor/Detail/5031-2010>.
- [3] D. Kalús, P. Páleš, L. Pelachová. Heat insulating panel with active regulation of heat transition (Patent No. EP 2 572 057 B1). European Patent Office, 2011. [2022-08-05], <https://patents.google.com/patent/WO2011146025A1/und>.
- [4] SUNOMAXCUBE. [2022-08-13], <https://sunomaxcube.com/>.
- [5] REHAU. [2022-08-13], <https://www.rehau.com/sk-sk>.
- [6] SUNOMAXCUBE. Individuality in series. [2022-08-13], <https://sunomaxcube.com/files/sunomaxcube/sunomaxcube-en.pdf>.
- [7] Isomax-Terrasol. [2022-08-13], <http://www.isomax-terrasol.eu/home.html>.
- [8] Rieder. [2022-08-13], <https://www.rieder.cc/us/>.
- [9] P. Michalak. Selected aspects of indoor climate in a passive office building with a thermally activated building system: A case study from Poland. *Energies* **14**(4):860, 2021. <https://doi.org/10.3390/en14040860>.
- [10] C. Zhang, M. Pomianowski, P. K. Heiselberg, T. Yu. A review of integrated radiant heating/cooling with ventilation systems- Thermal comfort and indoor air quality. *Energy and Buildings* **223**:110094, 2020. <https://doi.org/10.1016/j.enbuild.2020.110094>.
- [11] X. Wu, L. Fang, B. W. Olesen, et al. Comparison of indoor air distribution and thermal environment for different combinations of radiant heating systems with mechanical ventilation systems. *Building Services Engineering Research and Technology* **39**(1):81–97, 2018. <https://doi.org/10.1177/0143624417710105>.
- [12] M. Krajčík, O. Šikula. The possibilities and limitations of using radiant wall cooling in new and retrofitted existing buildings. *Applied Thermal Engineering* **164**:114490, 2020. <https://doi.org/10.1016/j.applthermaleng.2019.114490>.
- [13] B. Lehmann, V. Dorer, M. Koschrenz. Application range of thermally activated building systems tabs. *Energy and Buildings* **39**(5):593–598, 2007. <https://doi.org/10.1016/j.enbuild.2006.09.009>.
- [14] M. Krajčík, M. Arıcı, O. Šikula, M. Šimko. Review of water-based wall systems: Heating, cooling, and thermal barriers. *Energy and Buildings* **253**:111476, 2021. <https://doi.org/10.1016/j.enbuild.2021.111476>.

- [15] M. Schmelas, T. Feldmann, P. Wellnitz, E. Bollin. Adaptive predictive control of thermo-active building systems (TABS) based on a multiple regression algorithm: first practical test. *Energy and Buildings* **129**:367–377, 2016. <https://doi.org/10.1016/j.enbuild.2016.08.013>.
- [16] K.-N. Rhee, K. W. Kim. A 50 year review of basic and applied research in radiant heating and cooling systems for the built environment. *Building and Environment* **91**:166–190, 2015. Fifty Year Anniversary for Building and Environment, <https://doi.org/10.1016/j.buildenv.2015.03.040>.
- [17] J. Xie, X. Xu, A. Li, Q. Zhu. Experimental validation of frequency-domain finite-difference model of active pipe-embedded building envelope in time domain by using Fourier series analysis. *Energy and Buildings* **99**:177–188, 2015. <https://doi.org/10.1016/j.enbuild.2015.04.043>.
- [18] F. Niu, Y. Yu. Location and optimization analysis of capillary tube network embedded in active tuning building wall. *Energy* **97**:36–45, 2016. <https://doi.org/10.1016/j.energy.2015.12.094>.
- [19] M. Krzaczek, J. Florczuk, J. Tejchman. Improved energy management technique in pipe-embedded wall heating/cooling system in residential buildings. *Applied Energy* **254**:113711, 2019. <https://doi.org/10.1016/j.apenergy.2019.113711>.
- [20] T. Kisilewicz, M. Fedorczyk-Cisak, T. Barkanyi. Active thermal insulation as an element limiting heat loss through external walls. *Energy and Buildings* **205**:109541, 2019. <https://doi.org/10.1016/j.enbuild.2019.109541>.
- [21] R. Karadağ. New approach relevant to total heat transfer coefficient including the effect of radiation and convection at the ceiling in a cooled ceiling room. *Applied Thermal Engineering* **29**(8):1561–1565, 2009. <https://doi.org/10.1016/j.applthermaleng.2008.07.005>.
- [22] M. Krzaczek, Z. Kowalczyk. Thermal barrier as a technique of indirect heating and cooling for residential buildings. *Energy and Buildings* **43**(4):823–837, 2011. <https://doi.org/10.1016/j.enbuild.2010.12.002>.
- [23] C. Shen, X. Li. Energy saving potential of pipe-embedded building envelope utilizing low-temperature hot water in the heating season. *Energy and Buildings* **138**:318–331, 2017. <https://doi.org/10.1016/j.enbuild.2016.12.064>.
- [24] B. V. Stojanović, J. N. Janevski, P. B. Mitković, et al. Thermally activated building systems in context of increasing building energy efficiency. *Thermal science* **18**(3):1011–1018, 2014. <https://doi.org/10.2298/TSCI1403011S>.
- [25] Y. Yu, F. Niu, H.-A. Guo, D. Woradechjumnroen. A thermo-activated wall for load reduction and supplementary cooling with free to low-cost thermal water. *Energy* **99**:250–265, 2016. <https://doi.org/10.1016/j.energy.2016.01.051>.
- [26] J. Babiak, B. W. Olesen, D. Petras. Low temperature heating and high temperature cooling. Embedded water based surface heating and cooling systems. Finnish Association of HVAC Societies FINVAC, 2009. [2022-08-05], <https://www.osti.gov/etdweb/biblio/1030138>.
- [27] D. Petráš. *Nízkoteplotní vytápění a obnovitelné zdroje energie*. Bratislava. JAGA group, 2008. ISBN 978-80-8076-069-4.
- [28] D. Petráš, D. Kalús, D. Koudelková. *Vykurovacie systémy, cvičenie a ateliérová tvorba*. STU, Bratislava, 2012. ISBN 978-80-227-3795-1.
- [29] P. Janík. *Optimization of energy systems with long-term heat accumulation*. Ph.D. thesis, Slovak University of Technology in Bratislava, Faculty of Civil Engineering, 2013. SvF-13422-16657.
- [30] European Committee for Standardization. Heating systems in buildings - Design of embedded water based surface heating and cooling systems - Part 1: Determination of the design heating and cooling capacity (Standard No. EN 15377-1:2008).
- [31] Úrad pre normalizáciu, metrológiu a skúšobníctvo SR. Thermal protection of buildings. Thermal performance of buildings and components. Part 2: Functional requirements (Standard No. STN 73 0540-2+Z1+Z2).
- [32] M. Šimko, M. Krajčík, O. Šikula, et al. Insulation panels for active control of heat transfer in walls operated as space heating or as a thermal barrier: Numerical simulations and experiments. *Energy and Buildings* **158**:135–146, 2018. <https://doi.org/10.1016/j.enbuild.2017.10.019>.
- [33] B. Ning, S. Schiavon, F. S. Bauman. A novel classification scheme for design and control of radiant system based on thermal response time. *Energy and Buildings* **137**:38–45, 2017. <https://doi.org/10.1016/j.enbuild.2016.12.013>.
- [34] S. A. Al-Sanea, M. Zedan, S. Al-Hussain. Effect of thermal mass on performance of insulated building walls and the concept of energy savings potential. *Applied Energy* **89**(1):430–442, 2012. <https://doi.org/10.1016/j.apenergy.2011.08.009>.
- [35] M. Schmelas, T. Feldmann, P. Wellnitz, E. Bollin. Adaptive predictive control of thermo-active building systems (TABS) based on a multiple regression algorithm: First practical test. *Energy and Buildings* **129**:367–377, 2016. <https://doi.org/10.1016/j.enbuild.2016.08.013>.
- [36] E. Nemethova, D. Petras, M. Krajcik. Indoor environment in a high-rise building with lightweight envelope and thermally active ceiling. In *CLIMA 2016: Proceedings of the 12th REHVA World Congress*, vol. 22. 2016.
- [37] J. Široký, F. Oldewurtel, J. Cigler, S. Prívvara. Experimental analysis of model predictive control for an energy efficient building heating system. *Applied Energy* **88**(9):3079–3087, 2011. <https://doi.org/10.1016/j.apenergy.2011.03.009>.

APPLICATION OF STRUT-AND-TIE MODELS FOR ASSESSING RC HALF-JOINTS NOT COMPLYING WITH CURRENT CODE SPECIFICATIONS

GREGORIA KOTSOVOU^a, EMMANOUIL VOUGIOUKAS^b,
DEMETRIOS M. COTSOVOS^{c,*}

^a Independent consultant, Athens, Greece

^b National Technical University of Athens (NTUA), Laboratory of Reinforced Concrete Structures, 5 Iroon Polytechniou, Zografou, Athens 15780, Greece

^c Heriot-Watt University, Institute of Infrastructure and Environment, School of Energy, Geoscience, Infrastructure & Society, Edinburgh EH14 4AS, UK

* corresponding author: D.Cotsovos@hw.ac.uk

ABSTRACT.

The work described is concerned with an investigation of the effectiveness of the use of strut-and-tie models for the structural assessment of half joints. Such elements form a part of many existing bridges which, although not complying with current code specifications, have not as yet displayed any significant signs of distress in spite of the increase in traffic volume and loads over the years. The work is based on a comparative study of the predicted and experimentally established values of load-carrying capacity and location and causes of failure of half-jointed beams with reinforcement layouts that replicate those found in structures designed in accordance with previous code specifications. The results obtained show significant shortcomings of the assessment method as this is found not only to underestimate load-carrying capacity by a margin ranging between 40 % and 65 %, but also to often fail to identify the location and causes of failure. Therefore, there is a need for an alternative assessment method that will be based on concepts capable of both providing a realistic description of structural-concrete behaviour and identifying the causes of failure leading to the loss of load-carrying capacity.

KEYWORDS: Half joint, reinforced concrete, structural assessment, strut-and-tie models.

1. INTRODUCTION

Strut-and-Tie Models (STMs) are widely used to describe the function of reinforced concrete (RC) members at their ultimate limit state (ULS). It is considered that through them, it is possible to obtain a realistic representation of the flow of internal stresses developing in the RC members during the transfer of the applied load to the supports [1]. This flow of internal stresses is assumed to form a triangulated, statically determinate truss and the forces in individual struts and ties can be calculated in a straightforward manner solely based on principles of equilibrium.

While designing new structures, the selection of appropriate STM geometry requires skill and understanding of the flow of stresses within a deformable solid; reinforcing bars are then selected so as to have the required strength and checks conducted to verify that a failure of the concrete struts cannot occur before the strength of the ties is exhausted. Transfer of forces between struts and ties must also be checked. Such a calculation approach is widely considered to be capable of producing design solutions that satisfy the requirements of current codes for structural performance, such as those of EC2 [2] and EC8 [3].

However, in recent years there has been an increasing need for the assessment of structures designed in

accordance with past codes of practice as they do not conform with current design specifications and do not satisfy the corresponding requirements for structural performance. In spite these shortcomings many such structures have not displayed, to date, any significant sign of distress even in the case of existing bridges where there has been an increase in traffic volume and loads over the years. Nevertheless, the need for the available margin of safety to be realistically assessed remains. Therefore, a question arises: can STMs be as effective for the assessment of existing structures as they are considered to be for the design of new structures?

The work presented herein attempts to provide an answer to the above question through a comparative study of STM predictions and published experimental results on the behaviour of half-jointed RC beams with different arrangements of transverse reinforcement. The RC members assessed in the present work have been selected from the literature due to their practical significance as, in accordance with Transport Scotland [4], they are relevant to over 400 half-jointed concrete bridges in the UK Highways England network alone that do not comply with current design specifications.

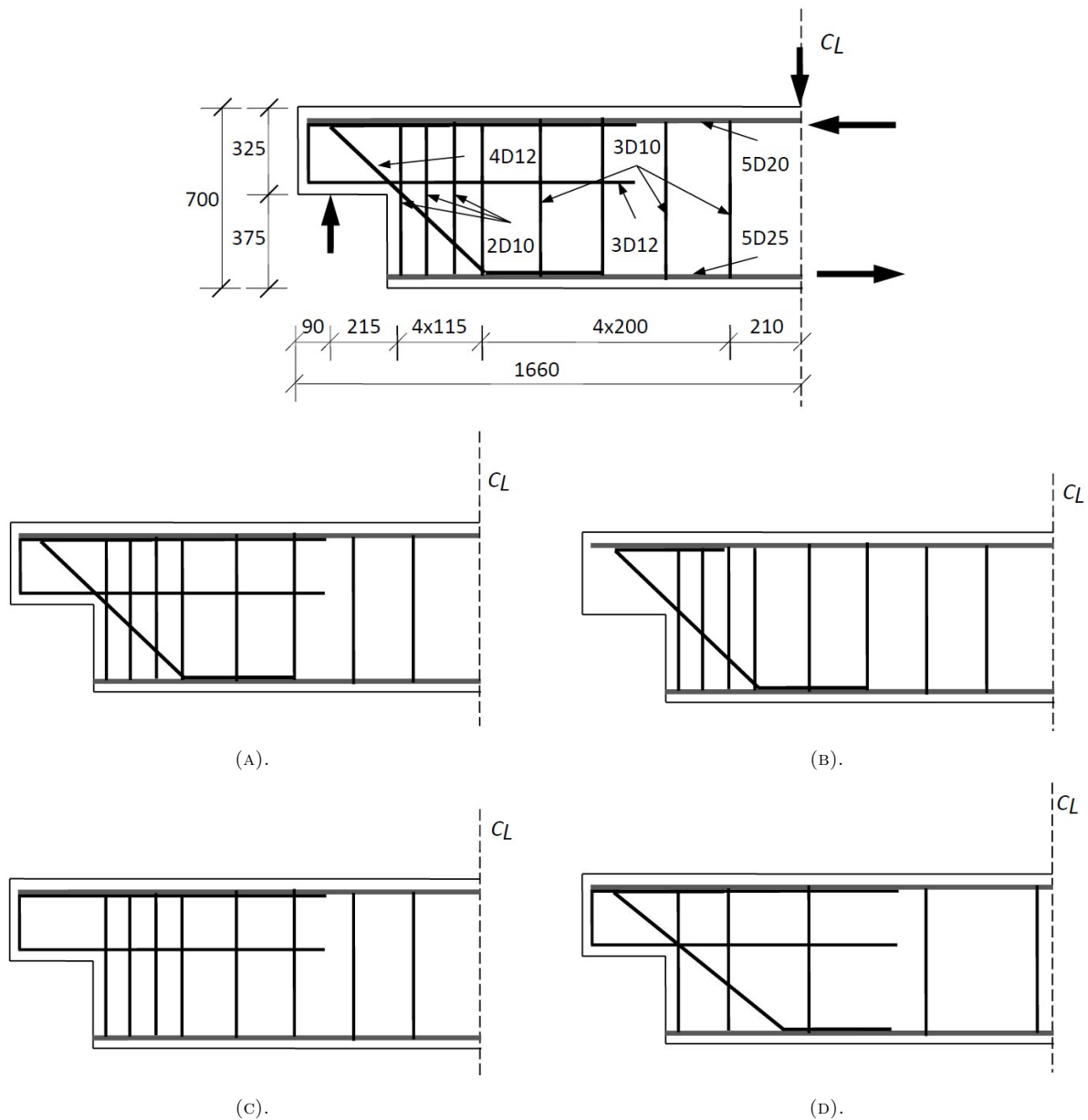


FIGURE 1. Top: Geometry, dimensions and reinforcement details of half-joint specimens. Bottom: Reinforcement layouts for the different test scenarios: (A) NS-REF, (B) NS-NU, (C) NS-ND, and (D) NS-RS.

2. HALF-JOINT BEAMS ASSESSED

The design details of the half-jointed beams used for investigating the suitability of STMs for a structural assessment are shown in Figure 1. These beams were tested under point loading (applied monotonically to failure) as described in [5], where a detailed description of the experimentally established behaviour of the specimens is presented. The uniaxial cylinder compressive strength of concrete at the time of testing was around 37 MPa and the yield stress of the steel reinforcement was 539 MPa and 529 MPa for the 10 mm and 12 mm diameter bars, respectively, and 578 MPa for the bars with a diameter of 20 mm or 25 mm.

Four different specimens were tested:

- One reference specimen, NS-REF, by considering the nib as the region with geometrical discontinuities (D-region) while the other regions of the beam are referred as beams or Bernoulli regions (B-regions). In the latter regions, the design was based on bending and shear theory and the Bernoulli assumption of “plane sections remain plane” is valid. In D-regions, due to the discontinuities, this assumption is not valid and the design was based on alternative methods such as strut-and-tie approaches [6].
- One specimen without the diagonal reinforcing bars, RS-ND, but where the reinforcement layout was otherwise identical to that of specimen NS-REF.

- One specimen without the U-bars, NS-NU, but also in all other aspects identical to specimen NS-REF, and, finally,
- One specimen identical to NS-REF in all aspects, but with a reduced number of shear links, NS-RS.

The three beams in which the reinforcing bars were removed replicate rebar layouts that can be found in practice in structures from previous decades. The latter layouts would no longer comply with current design codes and standards and hence no design load can be specified for these specimens. The different reinforcement layouts are also shown in Figure 1.

3. STRUT-AND-TIE MODELS ADOPTED

The selection of STMs for a structural assessment follows a common design practice. Such a selection is constrained by the reinforcement layout. Ties are taken to be parallel to the reinforcement, whereas struts may be inclined at any angle selected by the assessor, although typically the inclination will not be far outside the code specified limits. The assessor does, however, have some discretion in the number of reinforcement bars allocated to each tie. As there may be a number of STMs that satisfy the above requirements, the most suitable STM for a particular structure is that exhibiting the highest load-carrying capacity [1].

On the basis of the above, the STMs considered herein to provide a realistic description of the ULS function of the beams with the reinforcement layout indicated in Figure 1, are shown in Figure 2. The figure also shows, in light grey colour, the outline and reinforcement details of the beams. It is important to note that when tie and reinforcement directions coincide, only that particular reinforcement contributes to the formation of the tie. Such is the case of ties T1, T2, T3, T5 and T6 in Figure 2a, T1 and T2 in Figure 2b, T1, T4 and T5 in Figure 2c and T1, T2, T3, T4, T5 T6 and T7 in Figure 2d. Also, when a tie is shown to form in between two successive reinforcement bars, then, only these bars contribute to the formation of the tie. Such is the case of ties T4 in Figure 2a, and T2 and T3 in Figure 2c.

The STMs have been constructed so as to ensure the transfer of the applied load to the supports without violating the equilibrium conditions of the STM nodes. The failure load of the beams selected in the present work for the structural assessment is determined by the weakest individual element (relative to the calculated force to be resisted) of the STM. As discussed later, the STMs adopted in [7] for the structural assessment of beams NS-REF, NS-NU and NS-ND are also used in the present work for purposes of comparison. These models are shown in Figure 3.

4. STRUCTURAL ASSESSMENT

4.1. BEAM NS-REF

The STM adopted for describing the function of beam NS-REF at ULS is shown in Figure 2a. The figure shows the portion of the beam between the cross section where the load is applied and the left-hand side support. The applied load V , the support reaction $R (= V)$, and the horizontal couple of internal forces F developing on account of bending at the cross section through the load point are also shown in the figure.

Calculating the strength of the struts (designated as S1 to S6 in Figure 2a) in accordance with current code provisions (e.g. [2]) produces values significantly larger than those corresponding to flexural capacity. Since the latter is attained at a load V_f over 40% larger than its experimentally-established counterpart $V_{EXP} = 402$ kN, a strut failure cannot be the cause of loss of load-carrying capacity. For example, the strength of strut S3 calculated through the use of equation (6.5) in [2] is 737 kN, whereas, as will be seen later, the force developing under the experimentally-established load-carrying capacity $V_{EXP} = 402$ kN is only 354 kN. Therefore, a strut failure cannot be the cause of loss of load-carrying capacity. The latter can only occur due to a failure of the weaker (relative to the force to be resisted) of the ties designated as T1 to T6 in Figure 2a.

From Figure 2a, it can be seen that V is initially transferred along a single path comprising the STM members S6, T4 and S5. At the lower end of S5, this path bifurcates along T3 and T2, the latter transferring portions of V equal to xV and $(1-x)V$, respectively, from their lower to their upper end, with x being calculated as discussed later. Thereafter, the two portions of V are transferred to the support via struts S3 and S1.

The values of the forces developing in the STM members when the beam attains its experimentally-established load-carrying capacity $V_{EXP} = 402$ kN are calculated as follows:

- (1.) From the moment equilibrium condition of the portion of the beam in Figure 2a, $F = 993.92$ kN,
- (2.) Making use of the geometric characteristics of the STM, also indicated in Figure 2a, and considering the equilibrium conditions of the STM nodes yields the forces developing in the STM members as functions of x , with $x = 0.371$ being obtained by considering the equilibrium of the horizontal components of the forces acting on the STM node where members S2, S3, T3 and S4 meet,
- (3.) With x already known, the forces developing in the struts and ties can be easily obtained from the equilibrium conditions of the STM nodes; they are as follows: $F_{S1} = 252.86$ kN, $F_{S2} = 544.22$ kN, $F_{S3} = 354.23$ kN, $F_{S4} = 544.44$ kN, $F_{S5} = 514.58$ kN, $F_{S6} = 603.02$ kN, $F_{T1} = 321.23$ kN, $F_{T2} = 337.15$ kN, $F_{T3} = 149.14$ kN, $F_{T4} = 402$ kN,

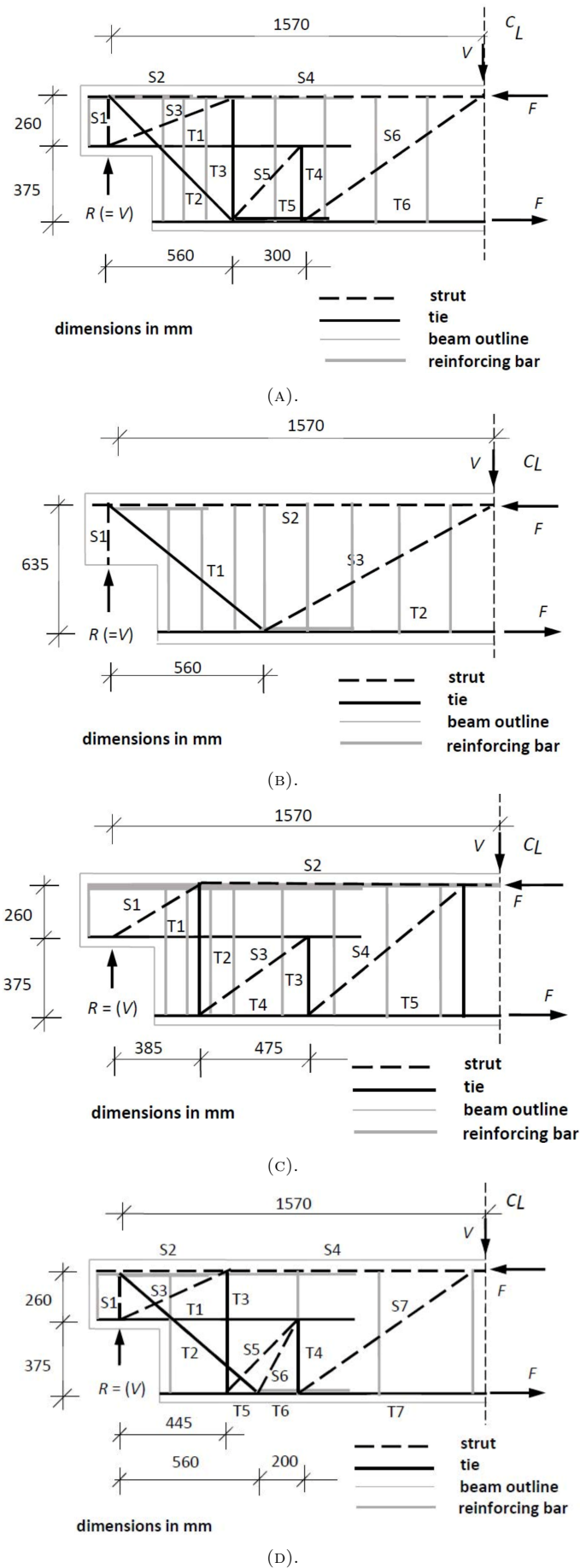


FIGURE 2. STMs of the beams with the different reinforcement layouts in Figure 1: (A) NS-REF, (B) NS-NU, (C) NS-ND, and (D) NS-RS.

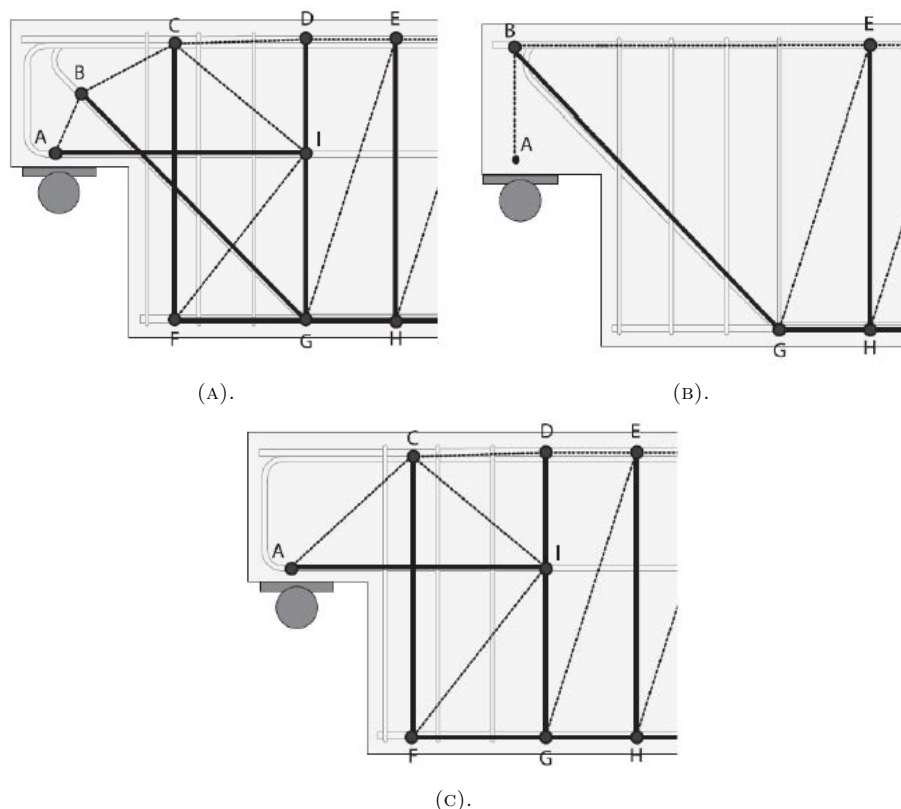


FIGURE 3. STMs adopted in Desnerck et al. [7] for beams: (A) NS-REF, (B) NS-NU, and (C) NS-ND.

$F_{T5} = 544.44$ kN, and $F_{T6} = 993.92$ kN, where F_{S_i} and F_{T_i} with $i = 1$ to 6, are the forces developing at the struts and ties, respectively.

The strength of each tie depends on the number of reinforcing bars considered to contribute to its formation. As discussed in Section 3, the horizontal and diagonal ties comprise all available bars aligned in the direction and level of the ties, whereas, of the vertical ties, Figure 2a shows that only one two-legged 10 mm diameter link contributes to the formation of T3 and two three-legged 10 mm diameter links to the formation of T4.

The values of strength of the ties (obtained as the product of the cross-sectional area of the ties and the yield stress of the steel) together with the values of the forces expected to develop in the ties when the experimentally-established value of load-carrying capacity of beam NS-REF is attained (see item iii above) are provided in Table 1, which also includes the number of reinforcing bars forming each tie and the values of the yield stress of the reinforcing bars. From the table, it can be seen that the loss of load-carrying capacity is predicted to be controlled by a failure of tie T1 (weakest element relative to the calculated force to be resisted) comprising the U-bars of the nib reinforcement, with failure of the tie occurring at a load of about 56 % of the experimentally established peak load.

The alternative STM of beam NS-REF adopted by [7] is shown in Figure 3a, with the forces developing in the ties AI, BG, CF, IG and EH at the experimentally-established peak load being given in Table 2. The table also includes the number of reinforcing bars forming each tie, the yield stress of the bars together with the resulting strength of the ties. From the table, it can be seen that the tie controlling the failure of the STM is tie EH, which is predicted to fail at a load of about 31 % of the experimentally-established value; this value is significantly smaller than the 56 % predicted by the STM adopted in the present work. Since STMs are developed within the context of the lower-bound theory of plasticity [1], the proposed model is considered more preferable for a structural assessment than the model proposed in [7].

4.2. BEAM NS-NU

The STM of the beam at ULS is shown in Figure 2b. The internal forces F developing on account of bending at the mid-span cut are found equal to 731.84 kN by considering (as for beam NS-REF) the moment equilibrium condition of the beam when it reaches its experimentally-established load-carrying capacity $V_{EXP} = 296$ kN. By solving the equations of equilibrium of the STM nodes it is found that the forces developing in the STM members are $F_{S1} = 296$ kN, $F_{S2} = 261.04$ kN, $F_{S3} = 556.12$ kN, $F_{T1} = 394.66$ kN, and $F_{T2} = 731.84$ kN.

Ties	Number of bars	Cross-sectional area of tie [mm ²]	Yield stress f_y [MPa] of reinforcement	Calculated Value strength F_u [kN] of tie	Forces in ties at experimental load-carrying capacity F_{EXP} [kN]	F_u/F_{EXP}
T1	3D12	339.29	529	179.49	321.23	0.56
T2	4D12	452.39	529	239.15	337.15	0.69
T3	2D10	157.08	539	84.67	149.14	0.57
T4	2×3D10	471.24	539	253.00	402.00	0.63
T5	5D25	2454.37	578	1418.43	544.44	2.61
T6	5D25	2454.37	578	1418.43	993.92	1.43

TABLE 1. Ties' strength and forces developing in the ties of the STM of beam NS-REF at the experimentally-established load-carrying capacity $V_{EXP} = 402$ kN.

Ties	Number of bars	Cross-sectional area of tie [mm ²]	Yield stress f_y [MPa] of reinforcement	Calculated Value strength F_u [kN] of tie	Forces in ties at experimental load-carrying capacity F_{EXP} [kN]	F_u/F_{EXP}
AI	3D12	339.29	529	179.49	216.46	0.83
BG	4D12	452.39	529	239.15	220.51	1.08
CF	2×2D10	314.16	539	169.33	243.85	0.69
IG	2×D10	157.08	539	84.67	243.85	0.35
EH	3×D10	235.62	539	127.00	402.00	0.31

TABLE 2. Ties' strength and forces developing in the ties of the STM adopted in [7] for beam NS-REF at the experimentally-established load-carrying capacity $V_{EXP} = 402$ kN.

Failure can only be linked with a failure of the inclined tie, T1, since, as for the STM of beam NS-REF, the load-carrying capacity of the struts calculated in accordance with [2], is found significantly larger than the value corresponding to the experimentally-established failure load of the beams; also, the large cross-sectional area of tie T2 (comprising five 25 mm diameter bars) precludes failure of the tie under the load that caused the failure of the beam. The strength of T1 (comprising four 12 mm diameter bars with a total cross-sectional area of 452.39 mm² and a yield stress of 529 MPa) is $F_u = 231.31$ kN, whereas the force expected to develop in the tie when the beam attains its experimentally-established load-carrying capacity F_{EXP} was found, as discussed earlier, to be $F_{T1} = 394.66$ kN, i.e. $F_{EXP} = F_{T1}$. Therefore, $F_u/F_{EXP} = 0.61$.

The alternative STM of beam NS-NU adopted in [7] is shown in Figure 3b. From the conditions of equilibrium of nodes B, G and E, it is easily established that the forces developing in ties BG and EH at the experimentally-established peak load of 296 kN are $F_{BG}^{EXP} = 394.66$ kN and $F_{EH}^{EXP} = 296$ kN. As ties BG and EH comprise four 12 mm diameter bars with a yield stress of 529 MPa and three 10 mm diameter bars with a yield stress of 539 MPa, respectively, the forces that they carry at yield are $F_{BG}^{STM} = 231.31$ kN

and $F_{EH}^{STM} = 68.18$ kN, which are about 61% and 23%, respectively, of the values of F_{BG}^{EXP} and F_{EH}^{EXP} , i.e. $F_{BG}^{STM}/F_{BG}^{EXP} = 0.61$ and $F_{EH}^{STM}/F_{EH}^{EXP} = 0.23$. Therefore, tie EH controls the failure and, on the basis of this, the STM of Figure 3b is predicted to fail at a load significantly lower than that of the STM adopted in the present work (see Figure 2b). Thus, as for the STM of beam NS-REF, the adopted model in the present work is found to be more suitable for the structural assessment than the STM adopted in [7].

4.3. BEAM NS-ND

The STM adopted for this beam at its ULS is shown in Figure 2c. As for beams NS-REF and NS-NU, the internal forces at the beam mid-span cut and the forces developing at the STM members are calculated from the equation of moment equilibrium of the beam and the equations of equilibrium of the STM nodes, respectively. They are found to be $F = 605.75$ kN, $F_{S1} = 438.13$ kN, $F_{S2} = 362.79$ kN, $F_{S3} = 395.39$ kN, $F_{S4} = 345$ kN, $F_{T1} = 362.79$ kN, $F_{T2} = 245$ kN, $F_{T3} = 245$ kN, $F_{T4} = 362.79$ kN, and $F_{T5} = 605.75$ kN.

As for beams NS-REF and NS-NU, the STM struts and the ties comprising five 25 mm diameter bars have a strength significantly larger than the forces developing in these STM members when the experimentally-established value of the failure load $V_{EXP} = 245$ kN

Ties	Number of bars	Cross-sectional area of tie [mm ²]	Yield stress f_y [MPa] of reinforcement	Calculated Value strength F_u [kN] of tie	Forces in ties at experimental load-carrying capacity F_{EXP} [kN]	F_u/F_{EXP}
T1	3D12	339.29	529	179.49	362.79	0.49
T2	2×2D12	314.16	529	169.33	245.00	0.69
T3	2×3D10	471.24	539	254.00	245.00	1.04

TABLE 3. Ties' strength and forces developing in the ties of the STM of beam NS-ND at the experimentally-established load-carrying capacity $V_{EXP} = 245$ kN.

Ties	Number of bars	Cross-sectional area of tie [mm ²]	Yield stress f_y [MPa] of reinforcement	Calculated Value strength F_u [kN] of tie	Forces in ties at experimental load-carrying capacity F_{EXP} [kN]	F_u/F_{EXP}
T1	3D12	339.29	529	179.49	233.49	0.77
T2	4D12	452.39	529	239.15	296.77	0.81
T3	2D10	157.08	539	84.67	136.47	0.62
T4	3D10	235.62	539	127.00	359.00	0.35

TABLE 4. Ties' strength and forces developing in the ties of the STM of beam NS-RS at the experimentally-established load-carrying capacity $V_{EXP} = 359$ kN.

is attained. Therefore, failure of the STM can only occur due to a failure of the weakest of ties T1, T2 and T3 relative to the force expected to develop when the beam's V_{EXP} is attained. The values of strength and the values of the forces developing in these ties when the applied load reaches the value of V_{EXP} are shown in Table 3 together with the number of the steel bars comprising each tie and the yield stress of the bars. From the table, it can be seen that the tie controlling the loss of load-carrying capacity of the adopted STM is tie T1, which fails at a load of about 49% of the experimentally-established peak value of beam NS-ND.

The alternative STM of beam NS-ND adopted in [7] is shown in Figure 3c. From the figure, it is apparent that the tie controlling failure of the STM is tie IG which comprises two 10 mm diameter bars with a yield stress of 539 MPa and, therefore, can carry a force $F_{IG}^{STM} = 2 \cdot (\pi \cdot 10^2/4) \cdot 539 = 84.67$ kN. Since the force that would develop in this tie, had it been possible for the STM to sustain the experimentally-established peak load of 245 kN, is $F_{IG}^{EXP} = 245$ kN, the STM's load-carrying capacity is only $F_{IG}^{STM}/F_{IG}^{EXP} = 84.67/245 \approx 0.35 = 35\%$ that of the beam tested. The latter value is significantly smaller than the value of 49% obtained for the STM adopted in the present work, which, yet again, is found to be a more suitable model for the structural assessment.

4.4. BEAM NS-RS

The STM adopted for beam NS-RS at its ULS is shown in Figure 2d. As for beam NS-REF, the load transfer is initially accomplished along a single path which, later on, bifurcates and, eventually, the applied load reaches the support via struts S1 and S3. The forces developing in the STM members when the beam reaches the experimentally established failure load $V_{EXP} = 359$ kN are calculated as for beam NS-REF and found to be: $F_{S1} = 228.58$ kN, $F_{S2} = 196.29$ kN, $F_{S3} = 310.51$ kN, $F_{S4} = 429.07$ kN, $F_{S5} = 178.19$ kN, $F_{S6} = 882.87$ kN, $F_{S7} = 581.88$ kN, $F_{T1} = 233.49$ kN, $F_{T2} = 296.77$ kN, $F_{T3} = 136.42$ kN, $F_{T4} = 359$ kN, $F_{T5} = 929.67$ kN, and $F_{T6} = 887.61$ kN.

For the reasons discussed in the preceding section, the STM struts and the ties comprising five 25 mm diameter bars are unlikely to fail before the applied load reaches its experimentally-established peak value. Therefore, failure of the STM can only occur due to a failure of the weakest of T1, T2, T3 and T4 relative to the force expected to develop when the applied load attains its experimental peak value of 359 kN.

The values of strength and the values of the forces developing in the above ties at peak load are shown in Table 4 together with the number of the bars comprising each tie and the yield stress of the steel bars. From the table, it can be seen that the tie controlling the failure of the STM is tie T4, which yields at a value of the applied load of about 35% of the experimentally-established value of the peak load of the beam.

5. DISCUSSION

From the results presented in the preceding section, it is seen that the STMs adopted for the beams tested predict values of load-carrying capacity that underestimate their experimentally-established counterparts by a margin which varies between approximately 40 % and 65 %.

More specifically, for beam NS-REF, the load-carrying capacity is underestimated by about 44 % with the weakest tie of the STM being the longitudinal tie T1, which, as indicated in Figure 2a, extends between the node at the beam support and the node where T1 intersects with S5 and T4. Therefore, the STM, by its nature, predicts that failure may initiate at any point along the length of T1. However, the experiment established that failure was preceded by yielding and/or rupture, in the region of the re-entrant corner, of not only the three 12 mm diameter U bars comprising tie T1, but also the four 12 mm diameter diagonal bars comprising tie T2 and the two-legged 10 mm diameter link closest to the re-entrant corner; moreover, the specimen suffered horizontal splitting of concrete in the compressive zone in the region of the nib (see Figure 4) [5].

The STM of beam NS-NU was found to exhibit a load-carrying capacity of 61 % of the value of its counterpart established from the tests. However, as for beam NS-REF, the STM predicts that failure may occur anywhere along the length of the weakest tie which is T1 (see Figure 2b) and the test results indicate that the loss of load-carrying capacity is preceded by yielding, in the region of the re-entrant corner, of not only the four 12 mm diameter diagonal bars comprising T1, but also yielding of the two-legged 10 mm diameter stirrup nearest to the re-entrant corner, as well as horizontal splitting of concrete in the compressive zone in the region of the nib (see Figure 4) [5].

Similar predictions were obtained for beam NS-ND. The loss of load-carrying capacity was linked with tie T1 (see Figure 2c that was found to be the weakest tie (see Table 2) with the experimental results showing that the failure of the beam is preceded by yielding, in the region of the re-entrant corner, of not only the three 12 mm diameter U-bars comprising T1, but also the two-legged 10 mm diameter stirrup closest to the re-entrant corner, as well as horizontal splitting of concrete in the compressive zone in the region of the nib as for beams NS-REF and NS-NU (see Figure 4). However, yet again, the predicted load-carrying capacity was less than half the experimentally-established value (see Table 3).

It should be noted at this stage that predicting failure of the longitudinal and diagonal ties precludes the likelihood of improvement of the STM predicted value of load-carrying capacity through an alternative STM with transverse ties comprising a larger number of links. Moreover, from the experimental results presented in [5], failure of the beam discussed above appears to be linked with flexural failure of the

beams' cross section that includes the inclined crack that invariably forms at the re-entrant corner (at an angle of about 45° with respect to the longitudinal axis) and penetrates deeply into the compressive zone. Assuming that the Bernoulli assumption is sufficiently accurate for practical purposes, the calculation of flexural capacity is rather straightforward by considering the conditions of equilibrium of the internal forces developing in concrete of the compressive zone and the reinforcing bars crossing the inclined crack as indicated in Figure 5. In the figure, $F_{c,c}$ is the force sustained by concrete in the compressive zone, $F_{s,c}$ the force sustained by the longitudinal steel reinforcement of the compressive zone, $F_{s,v}$ the force sustained by the vertical steel reinforcement crossing the inclined crack, $F_{s,u}$ the resultant of the forces developing in the U-bars in the region of the re-entrant corner and $F_{s,Dh}$ and $F_{s,Dv}$ the horizontal and vertical components of the resultant of the forces developing in the diagonal bars.

After the calculation of flexural capacity in accordance with current code methods, the solution of the equation of moment equilibrium of the portion of the beam between the cross section considered and the support results in the following values of load-carrying capacity: $R_{f,REF} = 352$ kN, $R_{f,ND} = 170$ kN, $R_{f,NU} = 261$ kN, for beams NS-REF, NS-ND and NS-NU, respectively. Thus, the corresponding ratios of the calculated to the experimental values are 0.88, 0.7 and 0.88, respectively. Moreover, a flexural type of failure is consistent with both the horizontal splitting of concrete in the compressive zone of the cross section and the yielding/rupture of the reinforcement crossing the inclined crack, as observed in the experiment. This is a significantly improved prediction of load-carrying capacity indicative of the advantages that may stem from adopting, as the basis for structural assessment, the modified beam theory first proposed in [8] and described in more detail in [9] and [10].

As regards beam NS-RS, not only the deviation of the predicted value of load-carrying capacity from its experimentally-established counterpart was significantly larger than that of beams NS-REF, NS-NU and NS-ND – the predicted value was merely 35 % of that established experimentally – but also the predicted location of failure differed from that established by experiment. The failure was predicted to occur due to failure of the lower end of the links forming tie T4 (see Figure 2d), whereas the loss of load-carrying capacity was found, by experiment, to occur due to horizontal splitting of concrete in the region of the beam between the tips of the deep inclined cracks in the full depth region and the upper face of the beam (see Figure 4). In accordance with the work presented in [9] and Kotsovos [10] such horizontal splitting of the compressive zone is caused by the action of transverse tensile stresses that develop for purposes of transverse deformation compatibility that is not allowed for in strut-and-tie modelling.

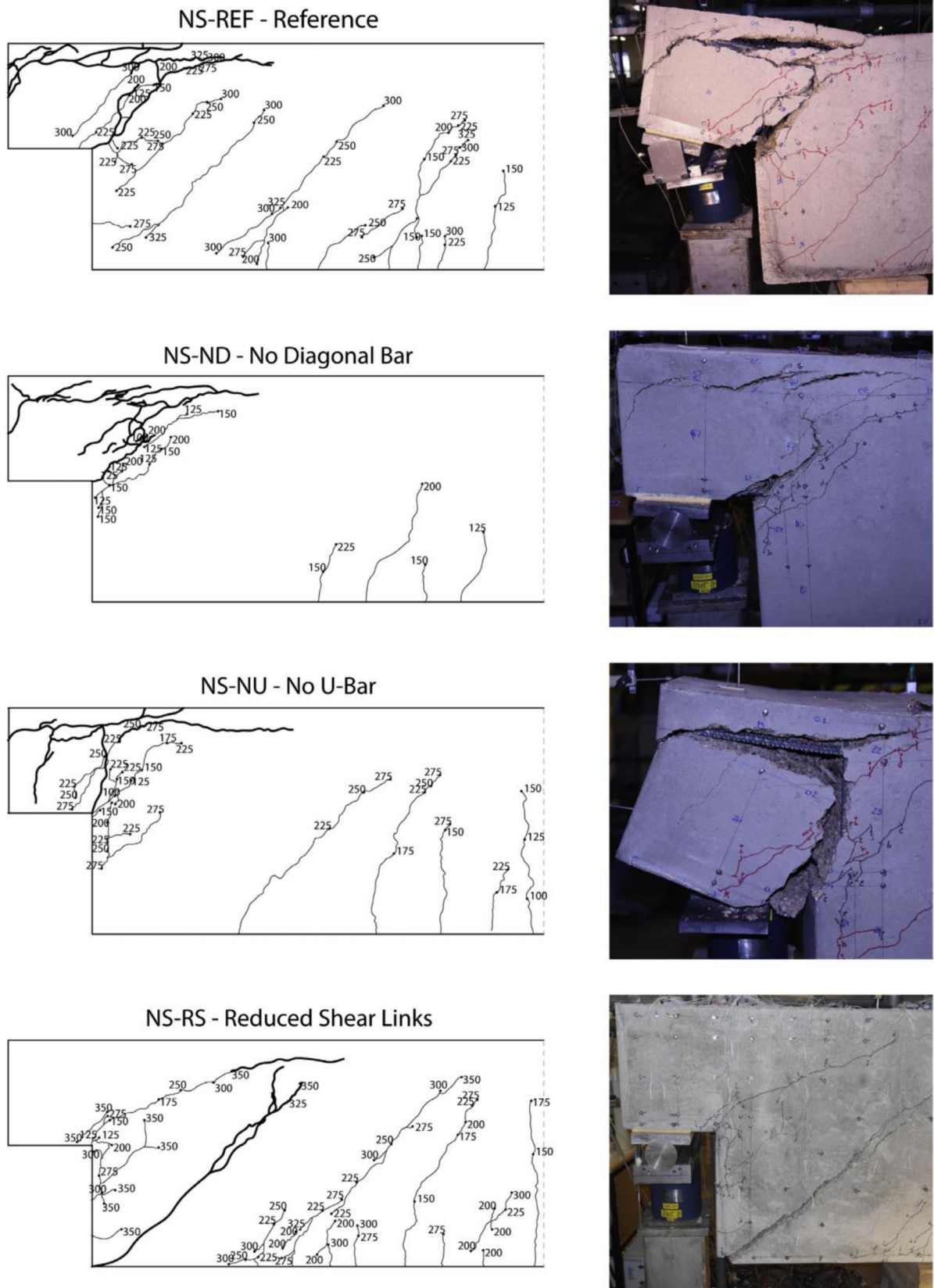


FIGURE 4. Final crack pattern of tested RC half-joint beams tested by Desnerck et al. [5].

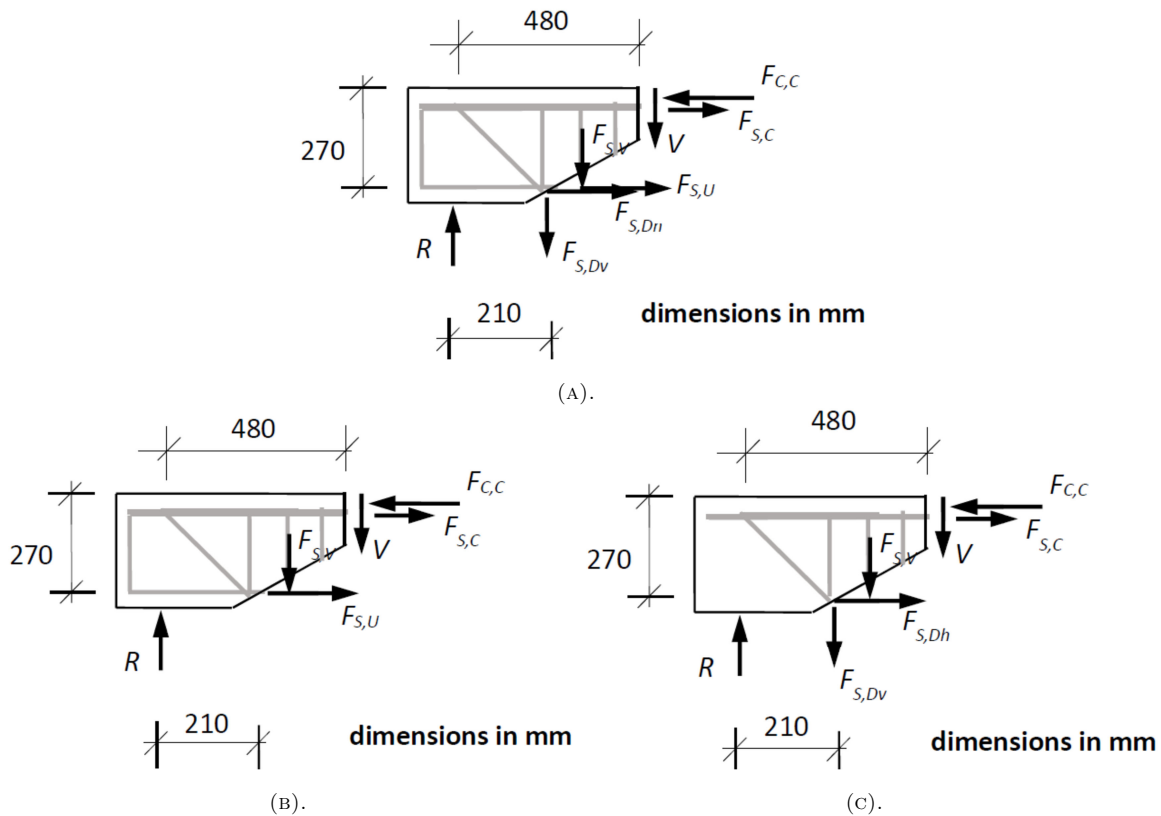


FIGURE 5. Internal forces in cross section including diagonal crack at re-entrant corner of beam (A) NS-REF, (B) NS-ND, and (C) NS-NU.

It appears from the above, therefore, that the use of STM for the structural assessment of half-jointed beams has two significant drawbacks not recognized until now: it underestimates load-carrying capacity by a factor larger than two, and, even when the causes of failure are correctly identified, cannot predict the location of the failure. Thus, there is a need for an alternative design method, the development of which could be based on concepts such as those presented in [8–10], capable of realistically describing both structural-concrete behaviour and the causes of failure underlying the loss of load-carrying capacity.

6. CONCLUSIONS

From the work presented in the paper, the following conclusions may be drawn:

In all cases considered, the predicted values of load-carrying capacity are significantly smaller than widely expected from their experimentally-established counterparts. The deviation of the predicted from the measured values ranges between 40% and 65%.

Moreover, they are found unable to predict the location of failure.

More specifically, strut-and-tie modelling is found unable to predict strut failure due to horizontal splitting of concrete in the compressive zone, which characterises the mode of failure of the beams tested. For beams NS-REF, NS-NU and NS-ND, such splitting occurred in the region of the nib, whereas for beam

NS-RS, in the full-depth region at a distance nearly equal to the cross-sectional depth from the re-entrant corner.

By nature, strut-and-tie models can only predict yielding and/or rupture of the reinforcement that comprises the tie controlling the failure of the model. For beams NS-REF, NS-NU and NS-ND, the tie predicted to control the failure consisted of reinforcing bars which did, in fact, yield before the loss of load-carrying capacity of the beams tested. However, as yielding can occur anywhere along the length of the tie, the location of the yielding of the reinforcement comprising this tie cannot be identified by the strut-and-tie model alone.

As regards beam NS-RS, the vertical tie predicted to control the failure is in the region of the applied load and not near the nib where the stirrups were found experimentally to yield before loss of load-carrying capacity of the specimen tested. Yet, failure was suffered due to horizontal splitting of concrete in the compressive zone of the full-depth region of the beam, which the model failed to predict.

In view of the above, there is a need for an alternative assessment method based on concepts capable of both realistically describing structural-concrete behaviour and identifying the causes of failure leading to loss of load-carrying capacity.

LIST OF SYMBOLS

F Internal forces developing on account of bending
 $F_{C,C}$ Force sustained by concrete in the compressive zone
 F_{EXP} Force developing at the weakest tie when $V = V_{EXP}$
 $F_{S,C}$ Force sustained by compression reinforcement
 $F_{S,V}$ Force sustained by links crossing inclined crack at re-entrant corner
 $F_{S,Dh}, F_{S,Dv}$ Horizontal and vertical components of force sustained by the diagonal reinforcement in a region of re-entrant corner
 $F_{S,U}$ Force sustained by U-bars in a region of re-entrant corner
 F_{S1} to F_{S7} Forces developing in the struts of STM
 F_{T1} to F_{T7} Forces developing in the ties of STM
 F_u Calculated force developing in the weakest tie
 R Reaction at support
 V Applied load
 V_{EXP} Experimentally established load-carrying capacity
 V_f Load at flexural capacity
 $V_{f,REF}, V_{f,ND}, V_{f,NU}$ Load at flexural capacity of cross section including inclined crack at re-entrant corner of beams NS-REF, NS-ND and NS-NU, respectively

Half-joint beams assessed

NS-REF Reference specimen
 NS-ND Specimen without diagonal reinforcement, but, in all other aspects, with reinforcement layout identical to that of NS-REF
 NS-NU Specimen without u-bar reinforcement, but, in all other aspects, with reinforcement layout identical to that of NS-REF
 NS-RS Specimen with reinforcement layout identical to that of NS-REF, but with a reduced number of stirrups

REFERENCES

- [1] J. Schlaich, K. Schafer, M. Jennewein. Toward a consistent design of structural concrete. *PCI Journal* **32**(3):74–150, 1987. <https://doi.org/10.15554/pci.j.05011987.74.150>.

- [2] The European Committee for Standardization. Eurocode 2: Design of concrete structures. Part 1-1: General rules and rules for buildings. (Standard No. EN 1992-1), 2004.
- [3] The European Committee for Standardization. Eurocode 8: Design of structures for earthquake resistance. Part 1-1: General rules, seismic standards and rules for buildings. (Standard No. EN 1998-1), 2004.
- [4] Transport Scotland (Agency of the Scottish Executive). TS interim amendment N°20 – Concrete half-joint deck structures, 2006. [2022-10-15], https://www.transport.gov.scot/media/6084/ts_ia_20.pdf.
- [5] P. Desnerck, J. M. Lees, C. T. Morley. Impact of the reinforcement layout on the load capacity of reinforced concrete half-joints. *Engineering Structures* **127**:227–239, 2016. <https://doi.org/10.1016/j.engstruct.2016.08.061>.
- [6] FIB Task Group 4.4. FIB bulletin 45 – Practitioners’ guide to finite element modelling of reinforced concrete structures, 2011. International Federation for Structural Concrete.
- [7] P. Desnerck, J. M. Lees, C. T. Morley. Strut-and-tie models for deteriorated reinforced concrete half-joints. *Engineering Structures* **161**:41–54, 2018. <https://doi.org/10.1016/j.engstruct.2018.01.013>.
- [8] M. D. Kotsovos. *Compressive Force-Path Method: Unified Ultimate Limit-State Design of Concrete Structures*. Springer, London, 2014.
- [9] M. D. Kotsovos. Conflicts between reinforced concrete design assumptions and actual concrete behaviour. *Proceedings of the Institution of Civil Engineers – Structures and Buildings* **175**(1):34–45, 2022. <https://doi.org/10.1680/jstbu.19.00003>.
- [10] M. D. Kotsovos. Beam theory – A proposed alternative basis for RC design. *Proceedings of the Institution of Civil Engineers – Structures and Buildings* 2021. [Ahead of print], <https://doi.org/10.1680/jstbu.20.00064>.

CONVERSION OF UNITS OF LENGTH FROM THE CZECH STATE STANDARD TO THE GEODETIC BASELINE JAVORIV

JIŘÍ LECHNER^{a,*}, NIKOLAI SERGEEVICH KOSAREV^a,
IGOR SERGEEVICH TREVOHO^b

^a *Research Institute of Geodesy, Topography and Cartography, Department of Metrology and Engineering Geodesy, Ústecká 98, 25066 Zdiby, Czech Republic*

^b *Lviv Polytechnic National University, Department of Geodesy, Karpinskoho 6, 79013 Lviv, Ukraine*

* corresponding author: jiri.lechner@vugtk.cz

ABSTRACT.

Modern society cannot do without high quality geospatial data. This need constantly strengthens with the growth of the information society and the emerging cyber society. Validity and quality of geospatial data is strongly connected to the level of its metrological service. It is necessary to conduct National metrological comparisons, in order to maintain an effective measuring infrastructure both inside a single country and in the whole Europe. The main result of such a comparison is a validation of actual values of key parameters of state standards.

The article presents results of a conversion of unit of length of the state standard of the Czech Republic to the geodetic baseline Javoriv (Ukraine), as performed by the staff of the Research Institute of Geodesy, Topography and Cartography (RIGTC). The conversion was realised in cooperation with Lviv Polytechnic National University (Ukraine). High-precision measuring equipment used during the conversion includes: the Leica AT401 laser tracker and the Leica Nova MS50 electronic total station.

A comparison of the measured length sections of the geodetic baseline Javoriv, performed by VUGTK employees, with the measurement results performed on a geodetic baseline Javoriv by specialists of the National Science Center (NSC) Institute of Metrology, gave a very good consistency. This is a sign of high quality results of comparative international measurement. It is planned to continue with the common efforts in the field of comparative international measurements between the Czech Republic and Ukraine in order to determine the actual values of the length sections of the geodetic baseline Javoriv.

KEYWORDS: The geodetic baseline Košnice, the geodetic baseline Javoriv, the state standard of the Czech Republic, conversion of unit of length.

1. INTRODUCTION

Geospatial industry is a key factor of global economy and social sphere development [1]. This is due to the general trend of the post-industrial era, which implies strengthening of the virtual component of the emerging hybrid world, a significant part of which is geospatial data [2]. Active integration of European countries is being ensured thanks to geospatial data, and a single European research and development space is being created in this area [3].

As a result of constant integration, there is a pressing need for high-precision geospatial support for a whole range of tasks in the field of geodesy, cartography, construction, cadastre and many others [4–6]. At the same time, obtaining reliable high-precision geospatial data is directly related to the level of their metrological service. The quality and objectivity of which is established with the help of national metrological services, as well as responsible organizations conducting a metrological comparison of measuring instruments used for these purposes [7, 8].

To date, in the field of geodetic instrumentation technology, there is an obvious tendency associated with the increase in the production of new measuring instruments. In this regard, there is an obvious need for constant modernisation of reference complexes to ensure the uniformity of length measurement as well as for constant international metrological comparisons. To achieve this, the European Association of National Metrology Institutes (EURAMET) was established in 2007 within the European Union. This association develops and distributes an integrated, cost-effective, and internationally competitive measuring infrastructure for Europe [9].

The EURAMET development strategy until 2030 presents the main directions for the modernisation of Europe's measuring infrastructure, the key tasks that the organization solves, and the main mission of the organisation, which includes the following four key points [10]:

- to develop and maintain an appropriate, integrated, and cost-effective measurement infrastructure for

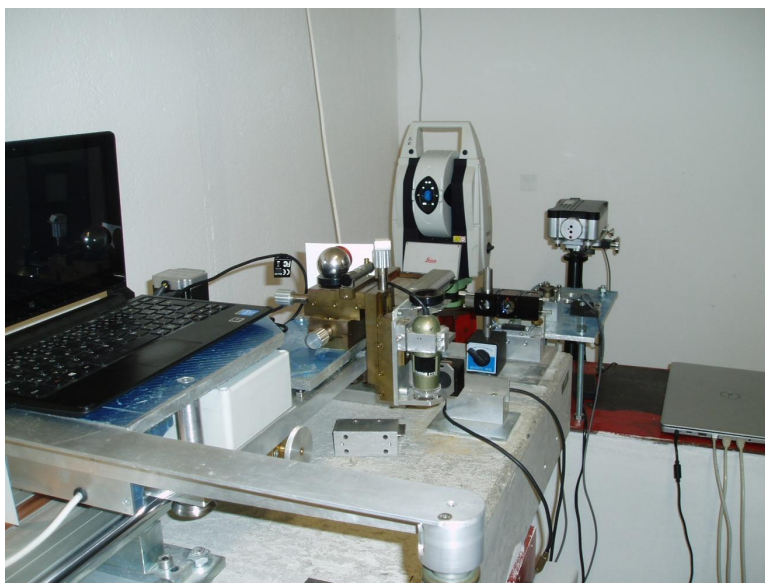


FIGURE 1. The laser interference comparator RIGTC.

Europe aligned to the needs of the society and industry;

- to ensure that the European measurement infrastructure is internationally competitive and recognised, and is based on a world-class R&D;
- to support policy and decision makers where metrology is the key;
- to support members of EURAMET in meeting their national requirements through collaboration and a balanced European measurement infrastructure.

EURAMET also includes RIGTC as a laboratory of the Czech Metrological Institute (CMI). Since 2006, RIGTC has been actively participating in length comparisons both inside and outside the Czech Republic. In April 2019, in the framework of a cooperation agreement with the National Lviv Polytechnic University (Ukraine), the first measurement for the conversion of unit of length of the State Standard to the Czech Republic on the geodetic baseline Javoriv (Ukraine) was performed. The measurements were completed in October 2021. This article presents the results of the conversion of unit of length of the state standard of the Czech Republic to the geodetic baseline Javoriv (Ukraine). The conversion was performed by employees of the RIGTK.

2. MATERIALS AND METHODS

2.1. REFERENCE COMPLEX FOR ENSURING THE UNIFORMITY OF LENGTH'S MEASUREMENTS RIGTC

The reference complex for ensuring the uniformity of length's measurement consists of a thirty-meter laser interference comparator and the geodetic baseline Koštice [10]. The laser interference comparator is located in a separate air-conditioned laboratory; it

is protected from noise, vibrations, and electromagnetic interference. The laboratory is equipped with a system maintaining a constant temperature and atmospheric pressure monitoring system. The comparator is equipped with a laser interferometer Renishaw XL-80, which allows calibrating geodetic measuring instruments with an error of $\pm(22 + 6 \cdot L \text{ (m)})$ (Figure 1).

The laser interferometer is the main standard of RIGTC and the main measuring and calibration equipment of the Institute.

2.2. THE GEODETIC BASELINE KOŠTICE (CZECH REPUBLIC)

The geodetic baseline Koštice is located along the road Koštice – Libčeves. It was built between 1979 and 1980 near the Koštice village in Louny district (Figure 2). The geodetic baseline Koštice consists of 12 pillars established to the depth from 5 to 9 m, situated at distances from 25 to 1450 meters. The pillars are equipped with devices for forced centring. The standard uncertainty of determining the length sections ranges from $\pm 0.3 \text{ mm}$ to $\pm 3.4 \text{ mm}$ [11]. From 2008, the geodetic baseline Koštice is the Czech State Long Distances Measuring Standard.

2.3. THE GEODETIC BASELINE JAVORIV (UKRAINE)

At present, the geodetic baseline Javoriv consists of 19 tubular metal pillars with a diameter of 200 mm established to the depth of up to 4 m. The total length of the baseline is approximately 2260 m. The pillars of the baseline protrude above the ground surface up to 1.3 m and end with a horizontal plate with a screw hole and a side oval cut-out in the pipe for an easy access to it. The precision of centring geodetic instruments is not less than 0.2 mm. The design of the construction is unique – it consists of a 10-meter phase section,

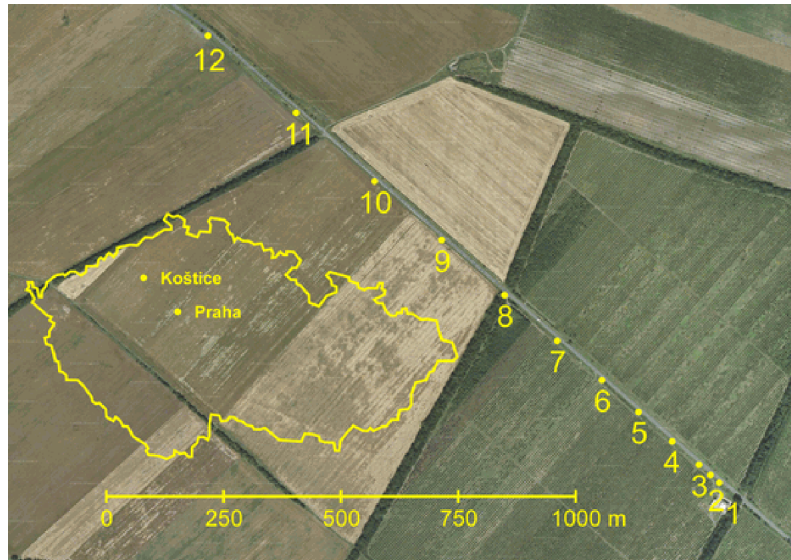


FIGURE 2. The schematic of the geodetic baseline Košnice.

fixed with points 1 m from pillar No. 4 to pillar No. 14. It allows us to determine the additive constant of any laser rangefinder, electronic total station, etc [12]. The general view of the geodetic baseline Javoriv is shown in Figure 3.

Metrological certification of the geodetic baseline Javoriv has been performed since 2003. The first metrological certification was carried out with a PLD-1M laser rangefinder (of an increased accuracy), and the subsequent ones were conducted with the help of precise electronic total stations and GNSS technologies (Table 1). The length sections of the geodetic baseline Javoriv were measured with a RMSE from 0.2 mm to 0.5 mm [13].

3. RESULTS

In April 2019, on the geodetic baseline Javoriv, employees of the RIGTC performed measurements according to the program in all combinations from pillar 1 to pillar 14 using Leica AT401 laser tracker [14]. These measurements were performed in accordance with a cooperation agreement with the National Lviv Polytechnic University (Ukraine). Each baseline section was measured no less than 10 times. From ten measurements, the average value was calculated.

Before performing the measurements, the additive constants of the Leica AT401 laser tracker and the Leica RRR 1.5 spherical prism in the accredited metrological laboratory RIGTC were determined (Figure 4). It is necessary to determine the additive constant of the tracker-prism measuring system because this value is of the time-varying nature of this correction, in addition, depending on the spherical prism chosen, the additive constant of the tracker-prism measuring system will be different [15, 16].

The difference of the additive constant of the Leica AT401 laser tracker and the Leica RRR 1.5 spherical prism in the period between June 2011 and August



FIGURE 3. The General view of geodetic baseline Javoriv.

2021 is shown in Figure 5. The magnitude of the additive constant change, in micrometres along the y-axis, is shown.

No	Year of measurements	Instrument
1	2003	PLD-1M (laser rangefinder)
2	2006	Trimble 5700 (receivers GPS)
3	2006	Trimble 5601 DR-Standard (electronic total station)
4	2007	Trimble 5601 DR-Standard (electronic total station)
5	2009	Leica TCR1201+R400 (electronic total station)
6	2009	Trimble 5700 (receivers GPS)
7	2010	Trimble 5700 and Leica GX1230GG (receivers GNSS)
8	2011	Leica TM 30R (electronic total station) and Trimble S8 (electronic total station)
9	2011	Trimble 5700, Leica GX1230GG and Novatel DL-V3 (receivers GNSS)
10	2012	Leica TM 30R (electronic total station) and ET Trimble S8 (electronic total station)
11	2012	Trimble 5700 and Leica GX1230GG (receivers GNSS)
12	2013	Leica TCR1201 (electronic total station) and Trimble S8 (electronic total station)
13	2014	Trimble 5700, Trimble R7, Leica GX1230GG and South S82T (receivers GNSS)
14	2015	Trimble S8 (electronic total station)
15	2017	Trimble S8 (electronic total station)
16	2018	Trimble S8 (electronic total station)

TABLE 1. Metrological certification of the geodetic baseline Javoriv.



FIGURE 4. The accredited metrological laboratory RIGTC.

The contractual measurements were continued in October 2021 using the Leica Nova MS50 electronic total station. The measurements were performed according to the program in all combinations from pillar No. 1 to pillar No. 19. During the measurements, the temperature, pressure and relative humidity of the air

at all pillars of the baseline using two different devices were recorded. After the measurements, atmospheric corrections and a constant of the Leica Nova MS50 electronic total station were added into each length section of the baseline.

The line lengths made by the Leica Nova MS50 electronic total station and the Leica AT401 laser tracker were compared at the accredited metrological laboratory RIGTC before the measurements. According to the results of the comparison, the RMSE in determining the differences was 0.19 mm.

The length sections of the geodetic baseline Javoriv collected from measurements of the Leica AT401 laser tracker, the Leica Nova MS50 electronic total station, and an assessment of their accuracy are shown in Table 2.

Measurements were not performed on the baseline section 1–4, because pillar No. 4 is damaged. In addition, it is necessary to additionally conduct control measurements with the Leica Nova MS50 electronic total station on the baseline sections 1–5 and 1–13 due to the problems with the centring of the reflector on the pillars No. 5 and No. 13.

The standard uncertainties given in Table 2 were calculated as follows

$$u_i = Q [a; b \cdot L_i(m)], \quad (1)$$

where:

- a* standard uncertainty of the additive constant of the Leica AT 401 laser tracker or the Leica Nova MS50 electronic total station (type A uncertainty);
- b* standard uncertainty of the multiplicative constant of the Leica AT401 laser tracker or the

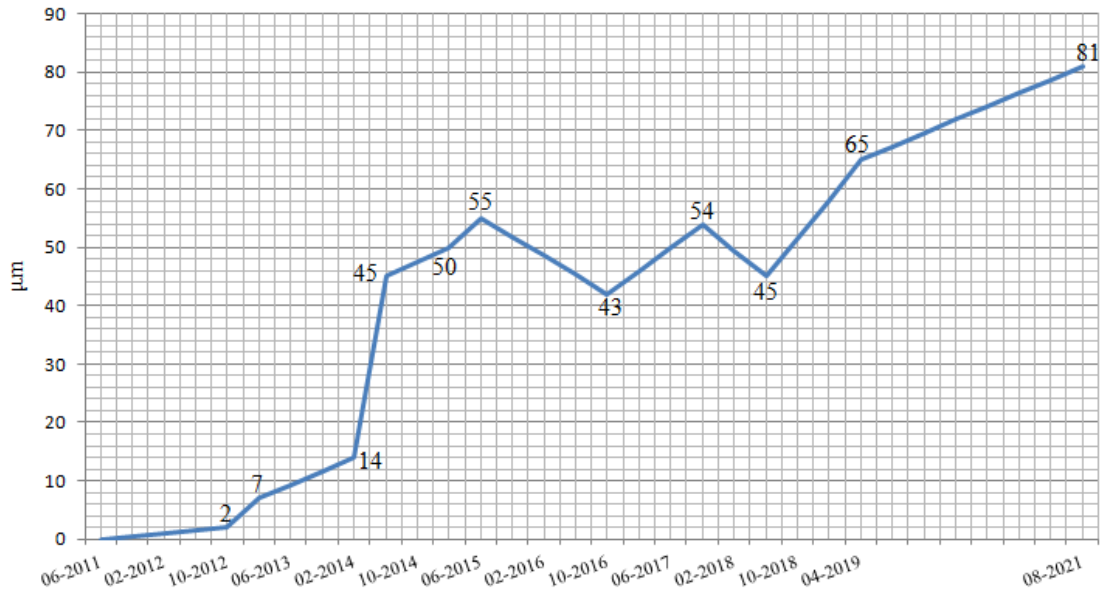


FIGURE 5. The difference of the additive constant of the Leica AT401 laser tracker and the Leica RRR 1.5 spherical prism in the period between June 2011 and August 2021.

Pillars	Length sections [m]		Standard uncertainty Leica AT401 [μm]	Standard uncertainty Leica Nova MS50 [mm]
	Leica AT401	Leica Nova MS50		
1-2	4.9822	4.9823	99	0.21
1-3	10.5331	10.5332	104	0.22
1-4	15.0297	–	108	–
1-5	16.0349	–	108	–
1-6	17.0345	17.0350	109	0.23
1-7	18.0298	18.0299	110	0.23
1-8	19.0254	19.0252	111	0.23
1-9	20.0284	20.0286	112	0.23
1-10	21.0212	21.0209	112	0.24
1-11	22.0232	22.0230	113	0.24
1-12	23.0208	23.0205	114	0.24
1-13	24.0203	–	115	–
1-14	25.0294	25.0292	116	0.24
1-15	–	129.6616	–	0.42
1-16	–	239.9904	–	0.61
1-17	–	589.3688	–	1.20
1-21	–	977.6581	–	1.86
1-20	–	2259.8946	–	4.04

TABLE 2. The length sections of the geodetic baseline Javoriv and their accuracy.

Leica Nova MS50 electronic total station (type B uncertainty);

L_i the measured length sections of the baseline (in meters);

Q quadratic sum of all partial uncertainties.

Standard uncertainties for the Leica AT401 laser tracker and the Leica Nova MS50 electronic total station were calculated based on the following documents [17–19]. The obtained values are given in Tables 3 and 4.

Quantity	Standard uncertainty	Unit	Probability distribution	Sensitivity coefficient	Uncertainty contribution $u_i(y)$	
					Additive constant	Scale correction
X_i	$u(x_i)$		i	c_i	$[\mu\text{m}]$	$[\mu\text{m}/\text{m}]$
Additive part of the uncertainty of the laser interferometer standard	0.01	μm	normal	1	0	–
Additive part of the uncertainty of the AT401	65.00	μm	normal	1	65	–
Multiplicative part of the uncertainty of the laser interferometer	0.22	$\mu\text{m}/\text{m}$	normal	1	–	0.22
Multiplicative part of the uncertainty of the AT401	0.70	$\mu\text{m}/\text{m}$	normal	1	–	0.70
Measurement uncertainty for temperature measurement accuracy	0.10	$^{\circ}\text{C}$	normal	0.924	–	0.09
Air temperature change in the path of the air measuring beam	0.30	$^{\circ}\text{C}$	normal	0.924	–	0.28
Measurement uncertainty for the accuracy of atmospheric pressure measurement	0.25	hPa	normal	0.271	–	0.07
Measurement uncertainty for determining of atmospheric pressure	0.50	hPa	normal	0.271	–	0.13
Measurement uncertainty for determining of the air humidity	5.00	%	normal	0.015	–	0.00
Effect of centering and horizontality of the CMM and RRR prism	50.00	μm	normal	1.4	70	–
Effect of uncertainty of cant determination	0.0471	$\mu\text{m}/\text{m}$	logarithmically normal	1	–	0.00
Uncertainty for straightening lengths to a straight line	0.00845	μm	logarithmically normal	1	0	–
Overall uncertainty u					96	0.80

TABLE 3. The uncertainty of the geodetic baseline Koštice in connection with Leica AT 401.

After, the length sections of the geodetic baseline Javoriv measured by the Leica AT401 laser tracker and the Leica Nova MS50 electronic total station were compared with the measurement results performed by specialists of the NSC Institute of Metrology (Ukraine) in 2003 using the PLD-1M laser rangefinder of increased accuracy (Table 5).

Based on the results of the comparison, the following conclusions can be drawn. The measured length sections of the geodetic baseline Javoriv using the Leica AT401 laser tracker and the Leica Nova MS50 electronic total station are generally consistent with the measurement results performed on the geodetic baseline Javoriv by specialists of the NSC Institute of Metrology (Ukraine), in 2003 using the PLD-1M laser rangefinder of increased accuracy.

In baseline section 1–3, measurement results contained differences that exceed the permissible values of the accuracy of determining the characteristics of the geodetic baseline Javoriv. This may be due to the fact that there may be individual shifts, which are most likely periodic in nature. In the baseline section 1–20, the maximum deviation from the measurement results performed by specialists of the NSC Institute of Metrology on a geodetic baseline Javoriv was obtained, which is 15.3 mm. It can be explained by the difficult observation conditions of this length section, namely the maximum temperature drop on the path of propagation of the electromagnetic signal, the high atmospheric turbulence at the time of the measurement and the influence of lateral refraction. In addition, this may be due to the instability

Quantity	Standard uncertainty	Unit	Probability distribution	Sensitivity coefficient	Uncertainty contribution $u_i(y)$	
					Additive constant	Scale correction
X_i	$u(x_i)$		i	c_i	[μm]	[$\mu\text{m}/\text{m}$]
Additive part of the uncertainty of the AT 401 standard	65	μm	normal	1	65	-
Additive part of the uncertainty of the MS 50 standard	170	μm	normal	1	170	-
Multiplicative part of the uncertainty of the AT401	0.75	$\mu\text{m}/\text{M}$	normal	1	-	0.75
Multiplicative part of the uncertainty of the MS50	2	$\mu\text{m}/\text{M}$	normal	1	-	2.00
Measurement uncertainty for temperature measurement accuracy	0.1	$^{\circ}\text{C}$	normal	0.924	-	0.09
Air temperature change in the path of the air measuring beam	0.3	$^{\circ}\text{C}$	normal	0.924	-	0.28
Measurement uncertainty for the accuracy of atmospheric pressure measurement	0.5	hPa	normal	0.271	-	0.13
Measurement uncertainty for determining of the air humidity	5	%	normal	0.015	-	0.08
Effect of centering and horizontality of the CMM and RRR prism	50	μm	normal	1.4	70	-
Effect of uncertainty of cant determination	0.0471	$\mu\text{m}/\text{m}$	logarithmically normal	1	-	0.00
Uncertainty for straightening lengths to a straight line	0.00845	μm	logarithmically normal	1	0.0	-
Overall uncertainty u					195	1.70

TABLE 4. The uncertainty of the geodetic baseline Koštice in connection with Leica MS 50.

of pillar No. 20, therefore, it is planned to repeat the measurement of baseline section 1–20.

4. CONCLUSION

A developing modern society cannot do without high-quality geospatial data. This need constantly strengthens with the growth of the information society and the emerging cyber society. As noted above, the reliability and quality of geospatial data is inextricably connected with the level of its metrological support. It is necessary to conduct National metrological comparisons, in order to maintain an effective measuring infrastructure both inside a single country and in the whole Europe. The main result of such a comparison is a validation of actual values of key parameters of state standards.

As part of the comparisons, the staff of the RIGTC conducted work on the conversion of unit of length of the state standard of the Czech Republic to the geode-

tic baseline Javoriv (Ukraine). When transmitting a unit of length, a high-precision measuring equipment was used: the Leica AT401 laser tracker and the Leica Nova MS50 electronic total station. As the result of comparing the measured length sections of the geodetic baseline Javoriv, performed by RIGTC employees, with the measurement results performed on a geodetic baseline Javoriv by specialists of the NSC Institute of Metrology, a good consistency of the measured data was obtained. This testifies the high quality of the international comparison and the stability of the baseline pillars.

The maximum deviations in the comparison results are obtained only for baselines 1–3 and 1–20. In baseline section 1–3, measurement results contained differences that exceed the permissible values of the accuracy of determining the characteristics of the geodetic baseline Javoriv. This may be due to the fact that there may be individual shifts, which are

Pillars	Length sections [m]			Difference [mm]		
	Leica MS50	Leica AT401	PLD-1M			
1	2	3	4	2-3	3-4	4-2
1-2	4.9823	4.9822	4.9816	-0.1	-0.6	-0.7
1-3	10.5332	10.5331	10.5285	-0.1	-4.6	-4.7
1-4	–	15.0297	15.0316	–	1.9	–
1-5	–	16.0349	16.0362	–	1.3	–
1-6	17.0350	17.0345	17.0344	-0.5	-0.1	-0.6
1-7	18.0299	18.0298	18.0287	-0.1	-1.1	-1.2
1-8	19.0252	19.0254	19.0241	0.2	-1.3	-1.1
1-9	20.0286	20.0284	20.0277	-0.2	-0.7	-0.9
1-10	21.0209	21.0212	21.0222	0.3	1.0	1.3
1-11	22.0230	22.0232	22.0215	0.2	-1.7	-1.5
1-12	23.0205	23.0208	23.0211	0.3	0.1	0.4
1-13	–	24.0203	24.0211	–	0.8	–
1-14	25.0292	25.0294	25.0294	0.2	0.0	0.2
1-15	129.6616	–	129.6612	–	–	-0.4
1-16	239.9904	–	239.9903	–	–	-0.1
1-17	589.3688	–	589.3680	–	–	-0.8
1-21	977.6581	–	977.6590	–	–	0.9
1-20	2259.8946	–	2259.9100	–	–	15.3

TABLE 5. The results of the comparison.

most likely periodic in nature. In the baseline section 1–20, the maximum deviation from the measurement results performed by specialists of the NSC Institute of Metrology on a geodetic baseline Javoriv was obtained, which is 15.3 mm. It can be explained by the difficult observation conditions of this length section, namely the maximum temperature drop on the path of propagation of the electromagnetic signal, the high atmospheric turbulence at the time of the measurement and the influence of lateral refraction. In addition, this may be due to the instability of pillar No. 20, therefore, it is planned to repeat the measurement of baseline section 1–20.

In the future, it is planned to continue the joint work in the field of comparative international measurements between the Czech Republic and Ukraine in order to determine the actual values of the length sections of the geodetic baseline Javoriv.

REFERENCES

- [1] A. P. Karpik, D. V. Lisitsky. Surveying industry: Prospective development directions in the post-industrial era and the digital economy. *Geodezia i Kartografia* **80**(4):55–64, 2019. <https://doi.org/10.22389/0016-7126-2019-946-4-55-64>.
- [2] H. Guo, S. Nativi, D. Liang, et al. Big earth data science: An information framework for a sustainable planet. *International Journal of Digital Earth* **13**(7):743–767, 2020. <https://doi.org/10.1080/17538947.2020.1743785>.
- [3] A. Annoni, M. Craglia. Towards a directive establishing an infrastructure for spatial information in Europe (INSPIRE). In *FIG Congress 2005*. 2005. [2022-04-10], https://fig.net/resources/proceedings/fig_proceedings/cairo/papers/ts_47/ts47_01_annoni_graglia.pdf.
- [4] United Nations Initiative on Global Geospatial Information Management (UM-GGIM). Future trends in geospatial information management: the five to ten year vision, 2020. [2022-04-10], https://ggim.un.org/meetings/GGIM-committee/10th-Session/documents/Future_Trends_Report_THIRD_EDITION_digital_accessible.pdf.
- [5] P.-O. Olsson, J. Axelsson, M. Hooper, L. Harrie. Automation of building permission by integration of BIM and geospatial data. *ISPRS International Journal of Geo-Information* **7**(8):307, 2018. <https://doi.org/10.3390/ijgi7080307>.
- [6] A. M. Tararin, V. L. Belyaev. Spatial data in urban planning. *Geodezia i Kartografia* **81**(11):29–39, 2020. <https://doi.org/10.22389/0016-7126-2020-965-11-29-39>.
- [7] A. P. Karpik, N. S. Kosarev, K. M. Antonovich, et al. Operational experience of GNSS receivers with Chip Scale Atomic Clocks for baseline measurements. *Geodesy and Cartography* **44**(4):140–145, 2018. <https://doi.org/10.3846/gac.2018.4051>.
- [8] M. Zrinjski, D. Barković, K. Špoljar. Pregled metoda preciznog umjeravanja kalibracijskih baza [in Croatian; Review of precise calibration methods of geodetic calibration baselines]. *Geodetski list* **76**(1):25–52, 2022.

- [9] L. Pendrill. EURAMET: European Association of National Metrology Institutes. *NCSLI Measure* 4(4):40–44, 2009. <https://doi.org/10.1080/19315775.2009.11721493>.
- [10] EURAMET 2030 strategy. [2022-04-10], https://sim-metrologia.org/wp-content/uploads/2021/10/EURAMET-Report_SIM_2021-11-02.pdf.
- [11] J. Lechner, L. Cervinka, I. Umnov. Geodetic surveying tasks for establishing a National long length standard baseline. In *FIG Congress 2008*. 2008. [2022-04-10], https://fig.net/resources/proceedings/fig_proceedings/fig2008/papers/ts03h/ts03h_02_lechner_etal_%203076.pdf.
- [12] I. S. Trevoho. Geodezicheskiy poligon dlya metrologicheskoy attestatsii priborov i aprobatsii tekhnologii [in Russian; Geodetic polygon for metrological certification of devices and approbation of technologies]. *Geoprofi* 1:6–11, 2009.
- [13] I. S. Trevoho, I. Tsyupak. Prospects of metrological provision linear geodetic of measurements on the geodetic test field. *Reports on Geodesy and Geoinformatics* 94(1):56–63, 2013. <https://doi.org/doi:10.2478/rgg-2013-0007>.
- [14] I. S. Trevoho, J. Lechner, B. Tora, et al. Geodetic activity for compatibility of the unit of length of geodetic bases Koštice (Czech Republic) and Javoriv (Ukraine). *Inżynieria Mineralna* 1(1):35–40, 2020. <https://doi.org/10.29227/IM-2020-01-05>.
- [15] J. Braun, M. Štroner, R. Urban, F. Dvořáček. Suppression of systematic errors of electronic distance meters for measurement of short distances. *Sensors* 15(8):19264–19301, 2015. <https://doi.org/10.3390/s150819264>.
- [16] F. Dvořáček. Laboratory testing of the Leica AT401 laser tracker. *Acta Polytechnica* 56(2):88–98, 2016. <https://doi.org/10.14311/AP.2016.56.0088>.
- [17] Joint Committee for Guides in Metrology. Evaluation of measurement data – Guide to the expression of uncertainty in measurement (JCGM 100:2008), 2008. [2022-04-10], http://www.bipm.org/utils/common/documents/jcgm/JCGM_100_2008_E.pdf.
- [18] ISO/IEC Guide 98-3:2008 Uncertainty of measurement – Part 3: Guide to the expression of uncertainty in measurement (GUM:1995). [2022-04-10], <https://www.iso.org/ru/standard/50461.html>.
- [19] EA Laboratory Committee. Evaluation of the uncertainty of measurement in calibration (EA-4/02 M:2022), 2021. [2022-04-10], <https://www.enac.es/documents/7020/635abf3f-262a-4b3b-952f-10336cdfae9e>.

THEORETICAL ANALYSIS OF THE INFLUENCE OF THE CHEVRON INCLINATION ANGLE ON THE THERMAL PERFORMANCE OF A GASKET PLATE HEAT EXCHANGER

ÉLCIO NOGUEIRA

State University of Rio de Janeiro, Department of Mechanic and Energy, Rio de Janeiro, Brazil

correspondence: elcionogueira@hotmail.com

ABSTRACT.

Different models are applied for an experimental and theoretical determination of the thermal and hydraulic performance of gasket plate heat exchanger. One of the relevant aspects of recent works is the influence of the chevron inclination angle between the heat exchanger plates. This work aims to analyse the impact of the chevron inclination angle by applying an effective concept in a sunflower vegetable oil cooler. Comparisons are made with theoretical and experimental results from the literature for works that consider angles of inclination equal to 30° , 45° , and 60° . An analysis model that does not consider the inclination angle as an explicit parameter is included for comparison purposes. In addition to the angle of inclination, two other parameters, the mass flow rate of the cold fluid (water) and the number of plates, are considered crucial for determining and analysing the results. Nusselt number, global heat transfer coefficient, effectiveness, heat transfer rate, and outlet temperatures for hot and cold fluids are presented in a graphical format. The results point to the need to improve models applied to gasket plate heat exchangers concerning the influence of the inclination angle since there are significant differences between those obtained and analysed in this work

KEYWORDS: Gasket plate heat exchanger, chevron inclination angle, vegetable oil cooler, theoretical analysis, second law of thermodynamics.

1. INTRODUCTION

Researchers have made numerous efforts to increase the performance of gasket plate heat exchangers; however, regarding the influence of the inclination angle of the chevron plates, there are different procedures recommended for determining the performance of the gasket plate heat exchanger. The work analyses three of these procedures [1–3], which have different degrees of refinement. The objective is to present the observed differences and emphasize them so that the differences between them are evident. To achieve the goal, two aspects that strongly influence the performance of the heat exchanger are included in the present analytical model: the number of plates and the mass flow rate of the working fluid. The inclusion of these two aspects, added to the inclination angle, emphasizes the significant differences between the procedures under analysis.

The present work theoretically analyses the influence of the three abovementioned parameters, but with a greater emphasis on the aspect related to the inclination angle. This parameter has been the object of a recent analysis [1, 2] through different methodologies, that is, a model that applies computational fluid dynamics (CFD) and another, more comprehensive, that uses a semi-analytical model coupled to an experimental procedure in an industrial plant. These procedures contrast with many works in which the influence of the angle of inclination is not considered

in determining the thermal performance of a gasket plate heat exchanger. Instead, most works use the Kumar correlation to determine the Nusselt number, as mentioned by Kacaç et al. [3].

In summary, the present work aims to analyse the impact of the chevron inclination angle on a Gasketed Plate Heat Exchanger, applying the concept of effectiveness in a sunflower vegetable oil cooler. The points under analysis are equal to 30° , 45° , and 60° .

The gasket plate heat exchanger consists of a package of thin corrugated metal plates pressed together, with the plates of the heat exchanger arranged so that the two fluids flow alternately in the channels. The heat exchanger's geometry enables high heat transfer coefficients and has low fabrication and maintenance costs. In addition, gasket plate heat exchangers have a solid and robust structure and are very effective for heat transfer. The search to improve the performance of these types of exchangers continues today, and experiments are carried out with the introduction of chevron-type plates. The improvement in the thermal performance depends on reliable correlations for Nusselt number determination and, consequently, accurate determination of heat transfer coefficients in the heat exchanger. This determination is vital for the design of industrial plants and the analysis of actual installations.

The work carried out by Skočilas and Palaziuk [1] applies computational fluid dynamics (CFD) to determine heat transfer through a chevron plate. They

provide expressions for tilt angle-dependent Nusselt number and use experimental results from the literature and results obtained by a numerical simulation to compare with the developed model. They state that the model of turbulent water flow between two corrugated chevron plates can provide relevant information about the momentum transfer and thermal diffusivity process. They fit the developed model using a numerical model and experimental data. They consider that the model can predict essential performance characteristics in plate heat exchangers concerning the dimensions, angles of inclination of the corrugations, etc. In addition, they claim that the performed simulation demonstrates the advantages of using chevron ripples as compared to using smooth plates since they allow high heat transfer coefficients. They conclude by saying that the simulation results can help find geometries with the lowest possible value of hydraulic resistance.

Neagu and Konsag [2] validate Lévêque's semi-analytical model using experimental data obtained in four heat exchangers of different sizes. The model considers the flow in the cell's sine duct in the furrow direction, and Nusselt numbers are calculated considering the construction of the channels. The model was validated for corrugation inclination angle relative to vertical direction equal to 30° . The analysis of relative errors and the statistical analysis concluded for predicting Nusselt number in gasket plate exchangers, showed promising results.

The correlation for the Nusselt number independent of the chevron plate inclination angle obtained by Kumar, referenced by Kakaç et al. [3], was also used in the analysis.

Élcio Nogueira [4] uses the concept of entropy generation to analyse the thermo-hydraulic performance of a gasket plate heat exchanger for cooling vegetable oil and uses volumetric fractions of non-spherical nanoparticles in a water-ethylene glycol mixture as a coolant. He concludes that it is possible to work with relatively low flow rates using non-spherical nanoparticles, emphasizing platelet-shaped nanoparticles. The analysis of thermal entropy generation versus viscous entropy generation shows that high flow rates dissipate a large part of the valuable energy available and do not contribute to oil cooling, increasing the operating cost of the heat exchanger.

Tovazhnyansky et al. [5] present the development and study of constructing a specially welded plate heat exchanger. They investigate heat transfer and hydraulic performance in a single-pass model under laboratory conditions, and propose an equation that relates the effectiveness and the number of thermal units. They develop a mathematical model for multi-pass heat exchangers from the results obtained, and validate the model through results obtained in an industrial prototype confirming the reliability and efficiency of the heat exchanger under analysis compared to a tubular heat exchanger. In addition, they devel-

oped a method that makes it possible to determine the height of the undulations and the number of passes for specified operating conditions.

Nguyen et al. [6] present a study where nickel, copper, and silver electrolytic coating is applied to stainless steel plate heat exchangers to improve the thermo-hydraulic performance. An experiment was conducted where the efficiency was evaluated using the global heat transfer coefficient, friction factor, number of transfer units, and effectiveness. It was found that all coated plate heat exchangers showed an increase in performance, especially for silver, followed by copper and nickel. Finally, they pointed out that the study shows a potential regarding applications in environments of severe and corrosive wear or with hygiene requirements.

Kumar and Singh [7] conducted an experimental study on a plate heat exchanger and presented thermal and hydraulic performance results with Reynolds numbers ranging between 800 and 5900. They use a chevron plate with an angle equal to 60° in isothermal or non-isothermal conditions. They compare the Nusselt number developed based on experimental data with analytical and numerical expressions from the literature, and conclude that the global heat transfer coefficient increases with the Reynolds number and decreases with the number of plates. They state that considering uniform flux distribution for many plates is undesirable.

Grigore et al. [8] present a theoretical and experimental study and perform a numerical simulation for a counterflow plate heat exchanger using the finite element method. They develop an iterative model that considers characteristics related to the channel geometry and determines heat transfer and fluid flow results. They conclude that the developed model agrees with experimental results, despite being a complex and labour-intensive simulation and presenting an excessive consumption of computational resources. In addition, they claim that the numerical simulation does not capture the influence of the angle and height of the ripple. However, the model offers a good understanding of the temperature distribution and fluid flow in turbulent conditions.

Jamil et al. [9] developed a theory to analyse heat exchangers through exergoeconomic concepts and normalised sensitivity analysis. The model allows the investigation of thermodynamic effects associated with fiscal parameters and is more comprehensive and significant than the conventional thermodynamic or economic analyses used separately. They present a practical example in a plate exchanger used in a desalination system. The sensitivity analysis demonstrates that the most critical input variables for determining the heat transfer rate are the mass water flows and the salinity. Essential variables of input for the cost of operation are the mass flow rates of hot and cold fluids, followed by the cost of electricity, interest rate, and pump efficiency. The parametric analysis demon-

strates that the $h/\Delta P$ ratio decreases with increasing Reynolds number and that the cold stream outlet cost is higher for $\beta = 30^\circ$ than for $\beta = 60^\circ$.

D. dos S. Ferreira et al. [10] study the application of the Wilson-Plot method for analysis and verify if the fluid inlet temperatures significantly influence the thermal behaviour of a plate heat exchanger. The research is performed by varying the inlet temperature and the mass flow of the hot fluid with the mass flow of the cold fluid, fixed. The experimental data presented a relative error of less than 15%, within the scope of uncertainties of the analysed correlations. It is concluded that the Wilson plotting method is highly effective for analysing the thermal behaviour of a plate heat exchanger.

Mota et al. [11] present two methods for analysing the thermal and hydraulic performance. The first simulates a configuration of a heat exchanger operating in a steady state. The parameters considered in the analysis are the number of channels, number of passes, the locations of the connections, and the type of flow. The second model applies to multi-pass heat exchangers with a large number of plates, which can be reduced to a single pass. In this particular case, they established that most multi-pass plate heat exchangers are equivalent to combinations of single-pass exchangers. They observed that the first model is limited to heat exchangers with a large number of plates and that industrial heat exchangers have more than 40 thermal plates. They highlight the advantage of using the first model as it has an applicability to any configuration. However, the implementation is highly complex, contrary to the second approach.

Anusha and Kishore [12] present an experimental work in a heat exchanger with 249 stainless steel welded metal sheets used in hydraulic cooling. They determine the correlation for Nusselt number as a function of Reynolds number, Prandtl number, and chevron angle. They get results for the heat transfer coefficient, overall heat transfer coefficient, and effectiveness. Graphical results are used to demonstrate the performance of the Gasket Plate Heat Exchanger. They conclude that the maximum effectiveness for counterflow arrangement is equal to 0.949 and that with increasing Reynolds number from 20 to 60, the Nusselt number increased by 10.01%, the friction factor decreased by 25.7%, the overall heat transfer coefficient increased by 10.44%, and the effectiveness increased by 12.53%.

Khond et al. [13] worked to optimise the performance of the plate heat exchanger by reducing the number of plates and, for that, they present a mathematical model that allows to reach the optimum in certain operational restrictions. The results obtained through applying the mathematical model demonstrate that the effect of the initial and final plates and the transverse flow distribution are considerable and affect the performance of the heat exchanger. They conclude that the model proposed in the work

meets the thermal and hydraulic demand and makes it possible to determine the smallest number of plates necessary for the adequate performance of the heat exchanger. However, they note that a more advanced algorithm is needed to achieve greater precision in determining the minimum number of plates.

In this context, the present work aims to analyse the impact of the chevron inclination angle in a Gasket Plate Heat Exchanger by applying the effective concept in a sunflower vegetable oil cooler. The tips under analysis are equal to 30° , 45° , and 60° .

2. METHODOLOGY

The geometric characteristic and physical parameters of the heat exchangers used in the present work were those tested by Neagu and Koncsag [2]. The relevant fact regarding the models is that Skočilas and Palaziuk [1] used water as the working fluid and two chevron plates for the numerical simulation (CFD). The work developed by Neagu and Koncsag [2] was theoretical and experimental in an industrial plant, using water and vegetable oil as working fluids, and presented comparisons with relative errors below 20%.

The fluids that exchange heat are water and sunflower vegetable oil. The water at 30° is used to cool vegetable oil that enters the heat exchanger at a temperature of 110° . The heat exchanger used for the analysis uses 63 plates, and the original chevron plate has an angle of inclination equal to 30° . The empirical expressions used to determine the Nusselt number were taken from three independent works [1–3]. Sunflower properties were taken from numerical tables provided in the literature [13] and determined through 3rd and 4th-degree polynomial interpolations (Equations (1)–(5)). Angles of 45° and 60° were introduced in the analysis for comparison purposes. The results independent of the inclination angle are arbitrarily referenced as the angle of inclination equal to 0° . Two parameters independent of the angle of inclination, the flow rate of the cold fluid and the number of plates of the heat exchanger, are predominant for determining the thermal performance. Therefore, their variations were included in the analysis.

Figure 1 shows geometric features of a chevron-type plate. Recent works [1, 2] use the chevron angle, β , the corrugation depth, b , and the corrugation wavelength, l , to look for local influences that can improve empirical expressions for the Nusselt number, which generally depends on the Reynolds number and the Prandtl number. In the present work, fixed values are adopted for b and l . In contrast, in most simulations, empirical expressions for Nusselt number are used in which the chevron angle appears explicitly.

Table 1 presents properties for the fluids used in this work as a function of average temperatures. Water is used to cool the vegetable oil in the case under analysis.

$T_{c_i} = 30^\circ\text{C}$ and $T_{h_i} = 110^\circ\text{C}$ are the inlet temperatures of water and vegetable oil. $\bar{T}_c = 35^\circ\text{C}$,

	ρ [kg/m ³]	k [W/(m K)]	C_p [J/(kg K)]	μ [kg/(m s)]	ν [m/s ²]	α [m/s ²]	Pr
Water	993.80	0.610	4186	$0.725 \cdot 10^{-3}$	$7.29 \cdot 10^{-7}$	$1.47 \cdot 10^{-7}$	4.96
Sunflower	913.00	0.163	2346	$11.54 \cdot 10^{-3}$	$1.26 \cdot 10^{-5}$	$0.76 \cdot 10^{-7}$	166

TABLE 1. Physical properties for cold (water) and hot (sunflower vegetable oil) fluids.

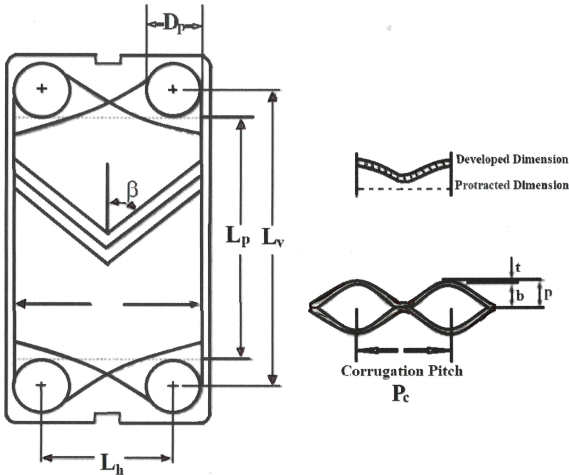


FIGURE 1. Basic geometrical dimensions of chevron corrugated plate heat exchanger [2].

$\bar{T}_h = 75^\circ\text{C}$ and $\bar{T}_W = 55^\circ\text{C}$.

$$\begin{aligned} \rho_h = & 920.8893939 - 0.09046037296 \bar{T}_h \\ & - 0.0003712121212 \bar{T}_h^2 \\ & + 2.331002331 \cdot 10^{-6} \bar{T}_h^3, \end{aligned} \quad (1)$$

$$\begin{aligned} \mu_h = & 0.144681007 - 0.00571479528 \bar{T}_h \\ & + 9.81172771 \cdot 10^{-5} \bar{T}_h^2 \\ & - 7.880585664 \cdot 10^{-7} \bar{T}_h^3 \\ & + 2.402607809 \cdot 10^{-9} \bar{T}_h^4, \end{aligned} \quad (2)$$

$$\begin{aligned} \mu_W = & 0.144681007 - 0.00571479528 \bar{T}_W \\ & + 9.81172771 \cdot 10^{-5} \bar{T}_W^2 \\ & - 7.880585664 \cdot 10^{-7} \bar{T}_W^3 \\ & + 2.402607809 \cdot 10^{-9} \bar{T}_W^4, \end{aligned} \quad (3)$$

$$\begin{aligned} k_h = & 0.1595212121 + 7.626262626 \cdot 10^{-5} \bar{T}_h \\ & - 5.303030303 \cdot 10^{-7} \bar{T}_h^2 \\ & + 2.5252525 \cdot 10^{-9} \bar{T}_h^3, \end{aligned} \quad (4)$$

$$\begin{aligned} C_{p_h} = & 2046.651515 + 3.511130536 \bar{T}_h \\ & - 0.005606060606 \bar{T}_h^2 \\ & + 9.906759907 \cdot 10^{-6} \bar{T}_h^3, \end{aligned} \quad (5)$$

where ρ_h is the specific mass (density) of the hot fluid, μ_h is the dynamic viscosity of the hot fluid, μ_W is the dynamic viscosity of the hot fluid at the surface, k_h is

the thermal conductivity of the hot fluid and C_{p_h} is the specific heat of the hot fluid.

ν_h is the kinematic viscosity or momentum diffusivity of the hot fluid and α_h is the thermal diffusivity of the hot fluid and Pr_h is the Prandtl number of the hot fluid:

$$\nu_h = \frac{\mu_h}{\rho_h}, \quad (6)$$

$$\alpha_h = \frac{k_h}{\rho_h C_{p_h}}, \quad (7)$$

$$Pr_h = \frac{\nu_h}{\alpha_h}. \quad (8)$$

$Rf_c = 0.00018$ and $Rf_h = 0.00053$ are the fouling factors of the cold and hot fluids, respectively. $N_t = 63$ (original value) is the number of plates used in the reference work [1], $\rho_c = 993.8 \text{ kg/m}^3$ is the specific mass (density) of the cold fluid, $\mu_c = 0.725 \cdot 10^{-3}$ is the dynamic viscosity of the cold fluid, $k_c = 0.610$ is the thermal conductivity of the cold fluid and $C_{p_c} = 4183$ is the specific heat of the cold fluid.

ν_c is the kinematic viscosity or momentum diffusivity of the cold fluid and α_c is the thermal diffusivity of the cold fluid and Pr_c is the Prandtl number of the cold fluid:

$$\nu_c = \frac{\mu_c}{\rho_c}, \quad (9)$$

$$\alpha_c = \frac{k_c}{\rho_c C_{p_c}}, \quad (10)$$

$$Pr_c = \frac{\nu_c}{\alpha_c}. \quad (11)$$

$L_V = 1.070$ is the vertical distance between centres of ports, $L_p = 0.858$ is the plate length between ports, $L_w = 0.450$ is the plate width, $L_h = 0.238$ is the horizontal length between centres of ports, $D_P = 0.212$ is the port diameter, $\delta_W = 0.6 \cdot 10^{-3}$ is the plate thickness, $k_W = 17.5$ is the thermal conductivity of the plate, $L_C = 175.56 \cdot 10^{-3}$ is the compressed plate pack length. Pit is the plate pitch:

$$Pit = \frac{L_C}{N_t}, \quad (12)$$

b is the corrugation depth:

$$b = Pit - \delta_W, \quad (13)$$

$\varphi = 1.17$ is the surface enlargement factor, D_h is the hydraulic diameter:

$$D_h = \frac{2b}{\varphi}, \quad (14)$$

A_{ch} is the channel cross-sectional free flow area:

$$A_{ch} = bL_W, \quad (15)$$

N_e is the effective number of heat transfer plates:

$$N_e = N_t - 3, \quad (16)$$

$N_p = 1$ is the number of fluid passes, N_{cp} is the number of channels for one pass:

$$N_{cp} = \frac{N_t - 1}{2N_p}. \quad (17)$$

$A_1 = 0.331$ is the heat transfer area for a plate, A_e is the heat transfer total area:

$$A_e = A_1 N_e, \quad (18)$$

$Re_h = 30.0$ (fixed) is the Reynolds number for hot fluid, G_{ch} is the mass velocity:

$$G_{ch} = \frac{Re_h \mu_h}{D_h}, \quad (19)$$

\dot{m}_{ch} is the mass flow rate per channel:

$$\dot{m}_{ch} = G_{ch} A_{ch}, \quad (20)$$

\dot{m}_h is the total mass flow rate of the hot fluid:

$$\dot{m}_h = \dot{m}_{ch} N_{cp}. \quad (21)$$

$$G_{cc} = \frac{Re_c \mu_c}{D_h}. \quad (22)$$

Re_c is the Reynolds number for cold fluid.

$$\dot{m}_{cc} = G_{cc} A_{ch}, \quad (23)$$

$$\dot{m}_c = G_c A_{ch}, \quad (24)$$

$$C_c = \dot{m}_c p_c, \quad (25)$$

$$C_h = \dot{m}_c p_h, \quad (26)$$

where m_c is the total mass flow rate of the cold fluid and C_h is the thermal capacity of the hot fluid. C_{min} is the minimum thermal capacity between the hot and cold fluids:

$$C^* = \frac{C_{min}}{C_{max}}. \quad (27)$$

Equations (1)–(27) include the physical property determination and mass flowrates needed for the Nusselt calculation. In Table 2, the parameters determined by Skočilas and Palaziuk [1] and for Kumar correlation [3] are presented.

2.1. EQUATIONS FOR NO EXPLICIT ANGLE IN THE EXPRESSIONS OF NUSSULT NUMBER

This section presents the Equations (28)–(38) that depend only on the coefficients and exponents shown in Table 2. Nu_c is the Nusselt number for cold fluid:

$$Nu_c = c_2 Re_c^n Pr_c^m \left(\frac{\mu_c}{\mu_W} \right)^x, \quad (28)$$

$$Nu_h = c_2 Re_h^n Pr_h^m \left(\frac{\mu_h}{\mu_W} \right)^x. \quad (29)$$

β	C_2	n	m	x
No angle (Kumar)	0.348	0.663	1/3	0.17
30°	0.14	0.64	0.39	0.1
45°	0.14	0.645	0.395	0.1
60°	0.14	0.65	0.40	0.1

TABLE 2. Coefficient and exponents for the expression of Nusselt [2] determined by Skočilas and Palaziuk [1].

h_h is the coefficient of heat convection for hot fluid:

$$h_c = \frac{Nu_c k_c}{D_h}, \quad (30)$$

$$h_h = \frac{Nu_h k_h}{D_h}. \quad (31)$$

U_o is the global heat transfer coefficient:

$$U_o = \frac{1}{\frac{1}{h_c} + \frac{1}{h_h} + \frac{\delta_W}{k_W} + Rf_c + Rf_h}. \quad (32)$$

$$NTU = \frac{U_o A_e}{c_{min}}, \quad (33)$$

where NTU is the number of thermal units associated with the heat exchanger and A_e is the total heat transfer area, established by Equation (18). ε_T is the thermal effectiveness:

$$\varepsilon_T = \frac{1 - e^{-NTU(1-C^*)}}{1 + C^* e^{-NTU(1-C^*)}}. \quad (34)$$

\dot{Q} is the actual heat transfer rate and Q_{max} is the maximum heat transfer rate:

$$\dot{Q} = \varepsilon_T C_{min} (Th_i - Tc_i), \quad (35)$$

$$\dot{Q}_{max} = C_{min} (Th_i - Tc_i). \quad (36)$$

Tc_o and Th_o are the outlet temperatures for cold and hot fluids, respectively:

$$Tc_o = Tc_i + \frac{\dot{Q}}{\dot{m}_c C p_c}, \quad (37)$$

$$Th_o = Th_i + \frac{\dot{Q}}{\dot{m}_h C p_h}, \quad (38)$$

3. EQUATIONS FOR EXPLICIT ANGLE IN THE EXPRESSIONS OF NUSSULT NUMBER

This section introduces several parameters (39)–(55) that explicitly depend on the chevron inclination angle, emphasizing the Nusselt numbers (56) and (57).

β is the chevron inclination angle:

$$\beta = \frac{\pi \beta}{180}, \quad [\text{rad}], \quad (39)$$

l is the corrugation wavelength:

$$l = Pit \sin \beta, \quad (40)$$

L_{furr} and L_{long} are the furrow and longitudinal flow components:

$$L_{furr} = \frac{l}{\sin 2\beta}, \quad (41)$$

$$L_{long} = \frac{l}{\sin \beta}. \quad (42)$$

XX is the ratio corrugation depth:

$$XX = \frac{b}{Pit}. \quad (43)$$

$D_{h \sin e}$ is the hydraulic dynamic diameter of a sine duct:

$$D_{h \sin e} = (0.149 XX^3 - 0.623 XX^2 + 1.087 XX - 0.0014)l, \quad (44)$$

$A_{ch \sin e}$ is the channel cross-section transverse to the furrow:

$$A_{ch \sin e} = A_{ch} \cos \beta. \quad (45)$$

$$u_{\sin ec} = \frac{\dot{m}_{cc}}{\rho_c A_{ch \sin e}}, \quad (46)$$

$$u_{\sin eh} = \frac{\dot{m}_{ch}}{\rho_h A_{ch \sin e}}, \quad (47)$$

$$Re_{\sin ec} = \frac{2u_{\sin ec} D_{h \sin e}}{\nu_c}, \quad (48)$$

$$Re_{\sin eh} = \frac{2u_{\sin eh} D_{h \sin e}}{\nu_h}. \quad (49)$$

$$C = 2.6624 XX^4 - 10.586 XX^3 + 11.262 XX^2 - 1.036 XX + 9.6, \quad (50)$$

$$K_{\text{einf}} = 5.888 XX^4 + 9.4611 XX^3 - 4.248 XX^2 - 0.1333 XX + 2.648, \quad (51)$$

$$K_{\text{dinf}} = 1.7237 XX^4 + 2.7669 XX^3 - 1.2651 XX^2 - 0.0097 XX + 1.512, \quad (52)$$

$$K_{\text{inf}} = 2(K_{\text{einf}} - K_{\text{dinf}}), \quad (53)$$

$$B = \frac{K_{\text{inf}} D_{h \sin e}}{4l_{furr}}. \quad (54)$$

f_{appc} is the apparent friction coefficient:

$$f_{appc} = \frac{C}{Re_{\sin ec}} + B. \quad (55)$$

$$Nu_{c \sin e} = 0.40377 \left(4f_{appc} Re_{\sin ec}^2 + Pr_c \frac{D_{f \sin e}}{l_{furr}} \right)^{1/3}, \quad (56)$$

$$Nu_{h \sin e} = 0.40377 \left(4f_{apph} Re_{\sin eh}^2 + Pr_h \frac{D_{f \sin e}}{l_{furr}} \right)^{1/3}. \quad (57)$$

Then, the overall thermal transfer coefficient $U_{o \sin e}$, number of transfer units $NTU_{\sin e}$, thermal effectiveness $\varepsilon_{T \sin e}$, and thermal flux $\dot{Q}_{\sin e}$, can be calculated with Equations (58)–(65)).

$h_{c \sin e}$ is the coefficient of heat convection for cold fluid and $h_{h \sin e}$ is the coefficient of heat convection for hot fluid:

$$h_{c \sin e} = \frac{Nu_{c \sin e} k_c}{D_{h \sin e}}, \quad (58)$$

$$h_{h \sin e} = \frac{Nu_{h \sin e} k_h}{D_{h \sin e}}. \quad (59)$$

U_o is the global heat transfer coefficient and $\varepsilon_{T \sin e}$ is the thermal effectiveness:

$$U_o = \frac{1}{\frac{1}{h_{c \sin e}} + \frac{1}{h_{h \sin e}} + \frac{\delta_W}{k_W} + Rf_c + Rf_h}. \quad (60)$$

$$NTU_{\sin e} = \frac{U_{o \sin e} A_e}{C_{\min}}, \quad (61)$$

$$\varepsilon_{T \sin e} = \frac{1 - e^{-NTU_{\sin e}(1-C^*)}}{1 + C^* e^{-NTU_{\sin e}(1-C^*)}}. \quad (62)$$

$\dot{Q}_{\sin e}$ is the actual heat transfer rate:

$$\dot{Q}_{\sin e} = \varepsilon_{T \sin e} C_{\min}(Th_i - Tc_i). \quad (63)$$

Tc_o and Th_o are the outlet temperatures for cold and hot fluids, respectively:

$$Tc_o = Tc_i + \frac{\dot{Q}_{\sin e}}{\dot{m}_c C_{p_c}}, \quad (64)$$

$$Th_o = Th_i + \frac{\dot{Q}_{\sin e}}{\dot{m}_h C_{p_h}}. \quad (65)$$

4. RESULTS AND DISCUSSION

The results presented in this work are strongly dependent on the experimental parameters determined by Neagu and Koncsag [2]. In addition to the physical and geometric parameters, the most significant influence on obtaining the results are Reynolds number, inlet temperatures, and heat exchanger plates. The Reynolds number range adopted for cold fluid is obtained from Table 5 of reference [2], i.e. $Re_c = 979 < Re < Re_c = 1530$. The Reynolds number for the hot fluid was kept fixed, equal to 30. The original number of plates, taken from Table 1, equals to 63. The inlet temperatures of the hot and cold fluids are equal to 110 °C and 30 °C, respectively. The angle of inclination used in the experiment is equal to 30 °C.

Figure 2 presents the apparent friction factor as a function of the Reynolds number. The angles under analysis are equal to $\beta = 30^\circ$, $\beta = 45^\circ$, and $\beta = 60^\circ$. The highlight is for the angle equal to 30° since the friction factor variation range is compatible with the results of Figure 3 of reference [2]. The results graphically presented in reference [2] show that the

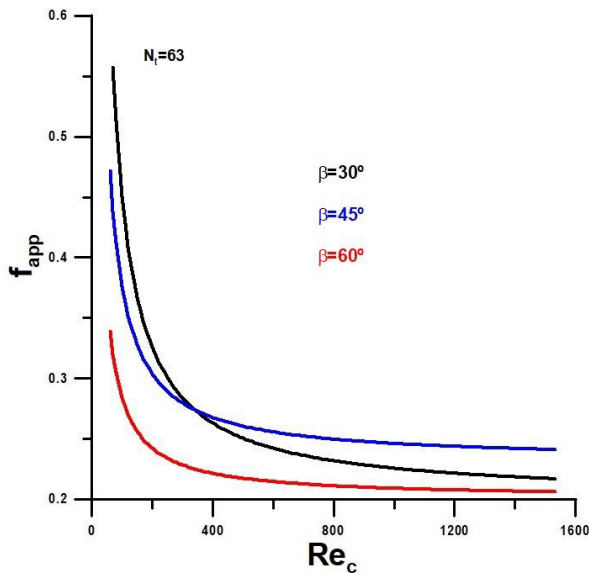


FIGURE 2. Apparent friction coefficient versus Reynolds number with slope angles as parameters.

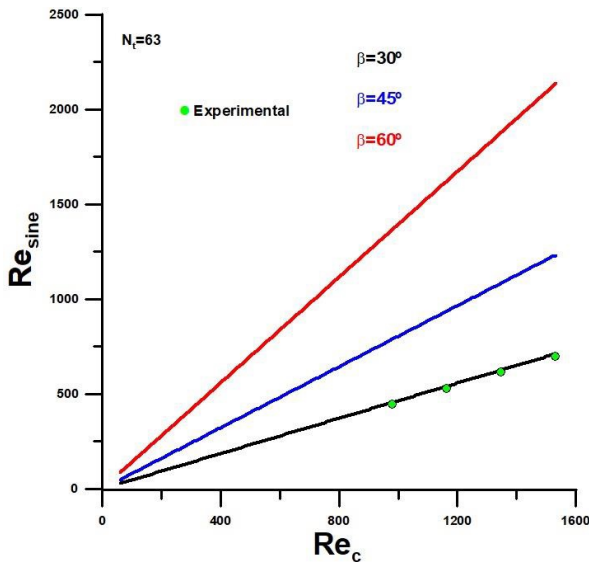


FIGURE 3. Resine versus Reynolds number for cold fluid (Experimental Ref. [2]).

lower limit value for the friction factor is equal to $f_{app} = 0.2$. In this specific situation (chevron angle equal to $\beta = 30^\circ$), the smallest value for the Reynolds number is equal to $Re_c = 60$, and the largest is equal to $Re_c = 1530$. The values obtained for angles equal to $\beta = 45^\circ$ and $\beta = 60^\circ$ show a slight variation concerning the reference angle but are compatible with the values and the trend presented by this one.

The relationship between the Reynolds numbers used in the expressions to determine the Nusselt numbers is shown in Figure 4, for a number of plates equal to $N_T = 63$. The Reynolds Re_{sine} number is dependent on the chevron in the inclination angle. The graph shows the relationship for the Reynolds number between $Re_c = 60$ and $Re_c = 1530$. The experimental values are taken from the reference [2], within

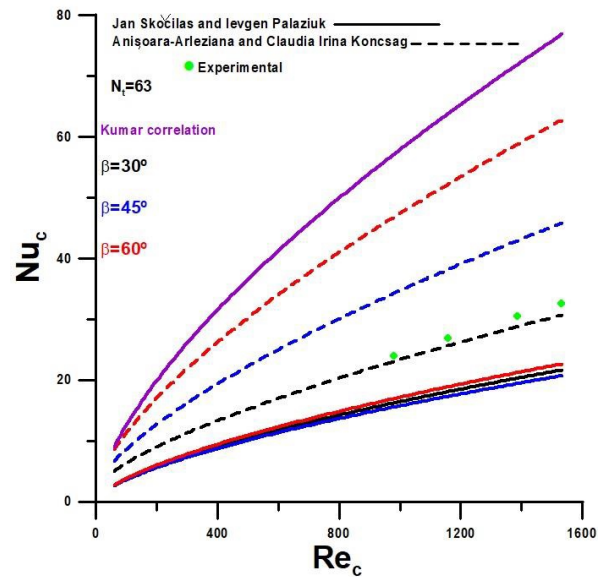


FIGURE 4. Nusselt number versus Reynolds number for cold fluid [1, 2].

the Reynolds number range between $Re_c = 979$ and $Re_c = 1530$, for an inclination angle equal to $\beta = 30^\circ$. The $\beta = 46^\circ$ and $\beta = 60^\circ$ angles are included in the analysis to compare and analyse the theoretical model.

The Nusselt number as a function of the Reynolds number, with slope angles as parameters, is represented in Figure 4. The models under analysis, already described above, were developed by Skočilas and Palaziuk [1], Neagu and Kocsag [2], and Kumar (in [3]). In Figure 4, the experimental values for an angle of $\beta = 30^\circ$ and Reynolds number in the range of $Re_c = 979$ to $Re_c = 1530$ are highlighted. The results obtained through the Skočilas and Palaziuk [1] model do not show great dispersion concerning the angles of inclination and present values significantly lower than the other models. Regarding the model developed by Neagu and Kocsag [2], a significant dispersion can be observed between the values obtained for the angles under analysis. In this case, the values for the Nusselt number increase with the angle of inclination. Regarding the Kumar correlation, regardless of the angle of inclination, it can be observed that the Nusselt number surpasses the other two models under analysis.

Figure 5 shows the global heat transfer coefficient for the models under analysis. It is noteworthy that the global heat transfer coefficient carries information related to the hot fluid and has a value for a Reynolds number equal to $Re_h = 30$. The results obtained through reference [3] do not present great numerical dispersion within the wide range of values obtained by the models. The highlight is the Kumar correlation, with intermediate values between the two models. There is a great difference between the models.

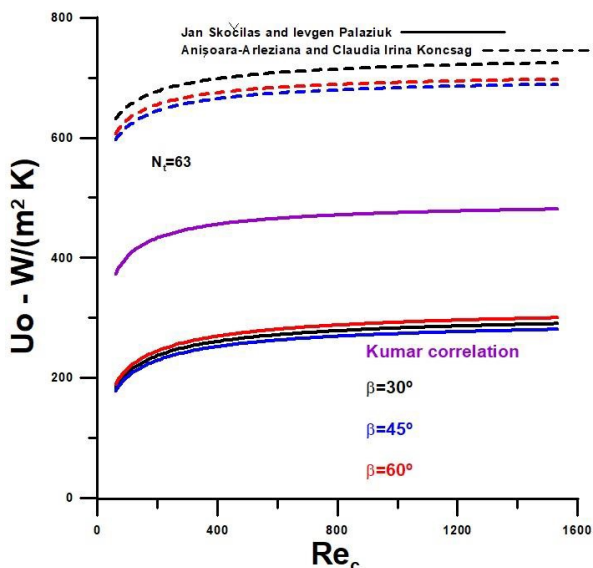


FIGURE 5. Global heat transfer coefficient versus Reynolds number for cold fluid [2].

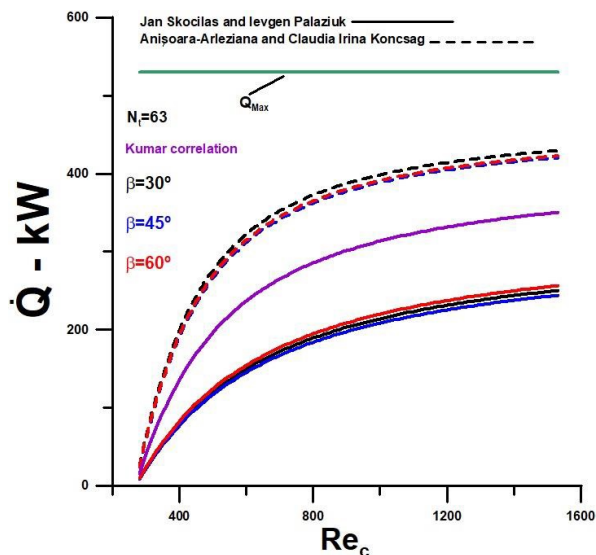


FIGURE 7. Heat transfer rate versus Reynolds number for cold fluid [2].

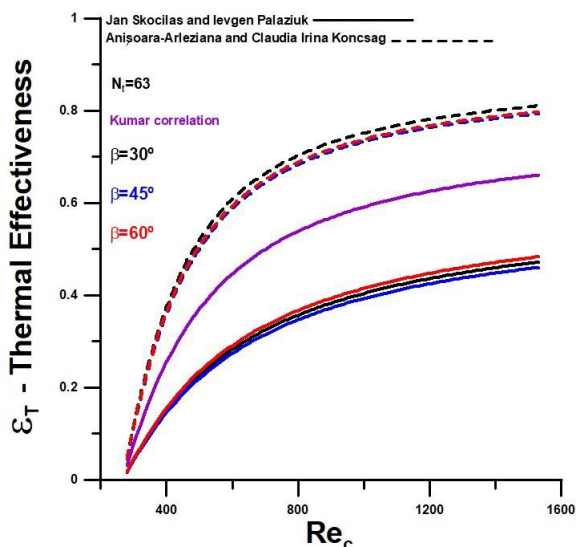


FIGURE 6. Thermal effectiveness versus Reynolds number for cold fluid [1, 2].

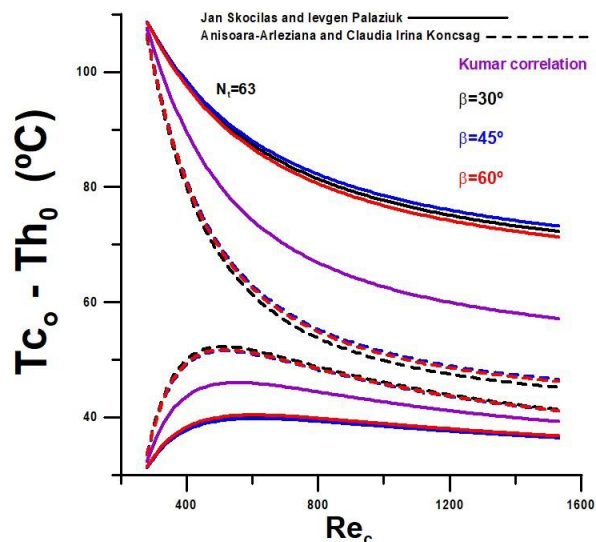


FIGURE 8. Outlet temperatures versus Reynolds number for cold fluid [2].

As expected, thermal effectiveness, represented by Figure 6, presents a behaviour similar to that obtained for the global heat transfer coefficient. Again, the attention is drawn to the great dispersion between the models, with significantly high values obtained through the reference model [1] concerning the reference values [3]. The effectiveness obtained by Neagu and Koncsag [2] is practically double that of the effectiveness obtained by the model developed by Skočilas and Palaziuk [1]. The Kumar model presents intermediate values, slightly closer to the results obtained through the reference [1].

Figure 7 shows the heat transfer rate and demonstrates, as already observed in Figure 5, that for plates equal to $N_t = 63$ and within the analysed flow rate, the maximum rate theoretically possible is significantly different from the values obtained by the model

associated with reference [2], the least conservative of the three under analysis.

Figures 8 and 9 show outlet temperatures for the fluids. The temperatures represented in Figure 8 demonstrate that the model developed and presented through reference [2], with an angle of 30° and plate number equal to $N_t = 63$, is close to the best possible result of the analysed heat exchanger. However, the model developed by Kumar tends to approach these results for higher flow rates. Figure 9 shows the outlet temperature for the hot fluid and demonstrates that the trend presented by the profiles is similar for all of them. The highlight for the model developed by Kumar shows intermediate values to the other two models. The flow variation is more significant as an influence on the thermal performance of the heat exchanger than the angle of inclination.

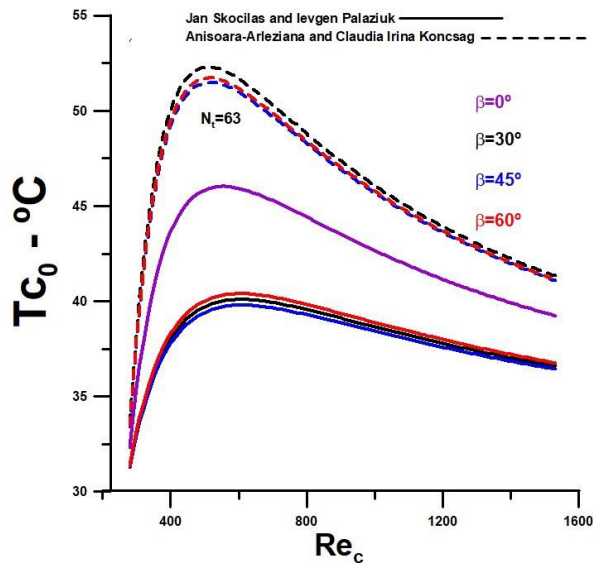


FIGURE 9. Outlet temperature for cold fluid versus Reynolds number for cold fluid.

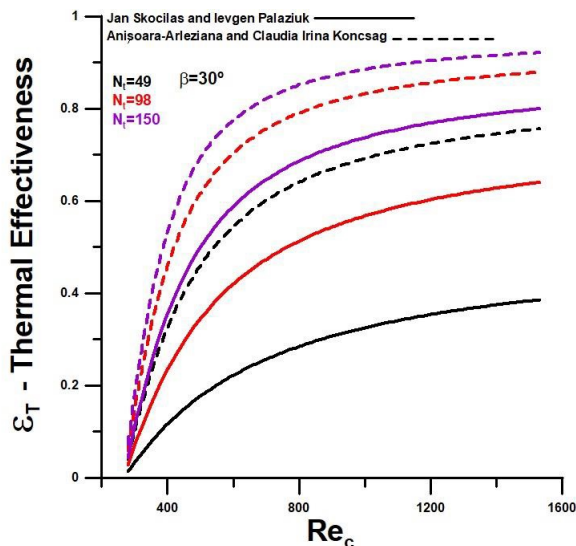


FIGURE 10. Thermal effectiveness versus Reynolds number for cold fluid with number of plates as a parameter.

Figure 10 shows the effectiveness for number of plates equal to $N_t = 49$, $N_t = 98$, and $N_t = 150$, and an inclination angle equal to $\beta = 30^\circ$. It can be observed that the differences between the models decrease with the increase in the number of plates. For example, with plates, in the case of the model developed by Neagu and Koncsag [2], the effectiveness is very close to 1, i.e., the heat transfer rate is very close to the maximum theoretically possible value.

The results shown in Figure 11 corroborate what was observed for effectiveness. The heat transfer rate increases with the number of plates and approaches the maximum theoretically possible for a plate number equal to $N_t = 150$ and a Reynolds number equal to $Re_c = 1530$. However, the values obtained for heat transfer rate through the model of Skočilas and

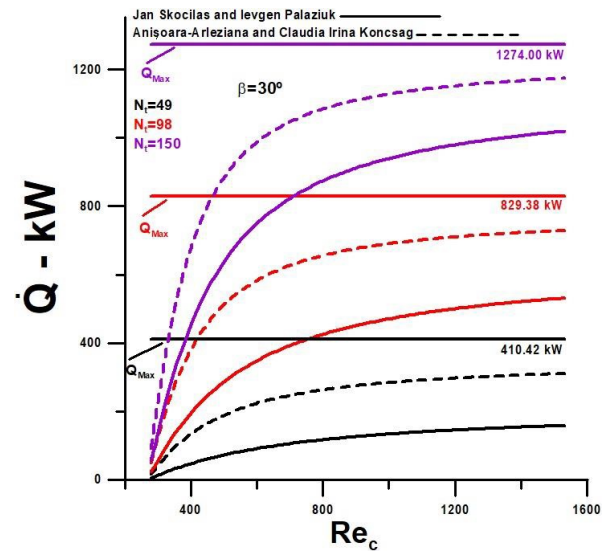


FIGURE 11. Heat transfer rate versus Reynolds number for cold fluid with the number of plates as a parameter [1].

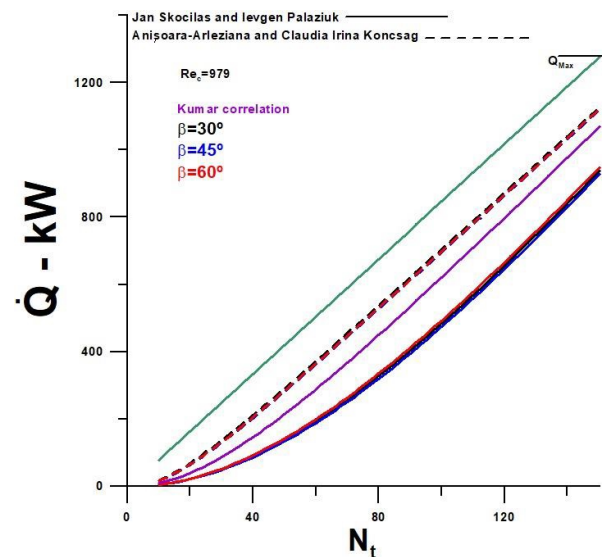


FIGURE 12. Heat transfer rate versus the number of plates for Reynolds number equal to 979 and with inclination angle as a parameter.

Palaziuk [1] are relatively different from the maximum possible for any number of plates within the range under analysis.

Figures 12 and 13 show results for heat transfer rate as a function of the number of plates, for Reynolds numbers equal to $Re_c = 979$ and $Re_c = 1530$, with slope angles as parameters. The heat transfer rate increases with the number of plates and approaches the maximum for the highest flow rates under analysis. For high plate numbers, the model developed by Kumar is close to the model presented by Neagu and Koncsag [2]. The inclination angle does not significantly affect the heat transfer rate, regardless of the model analysed.

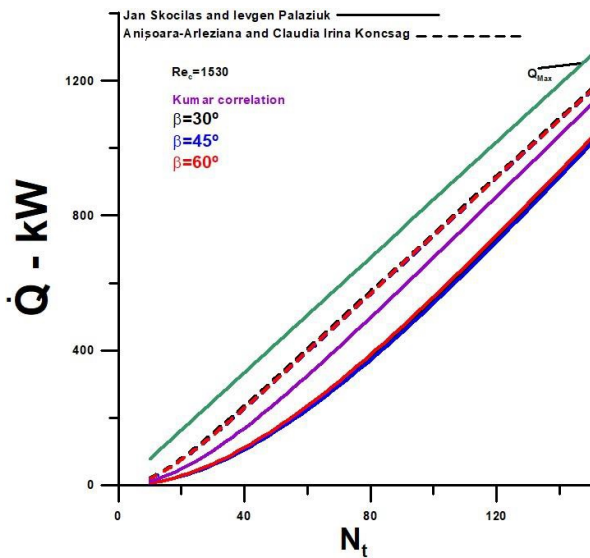


FIGURE 13. Heat transfer rate versus the number of plates for Reynolds number equal to 1530 and with inclination angle as a parameter.

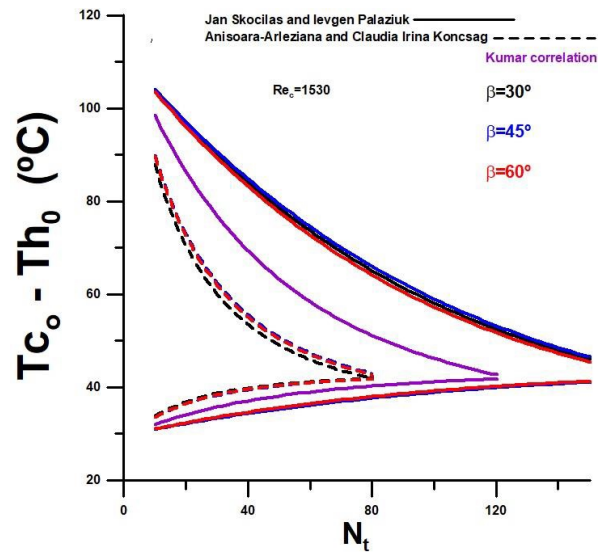


FIGURE 15. Outlet temperatures of fluids versus the number of plates for Reynolds number equal to 1530 and with inclination angle as a parameter [1, 2].

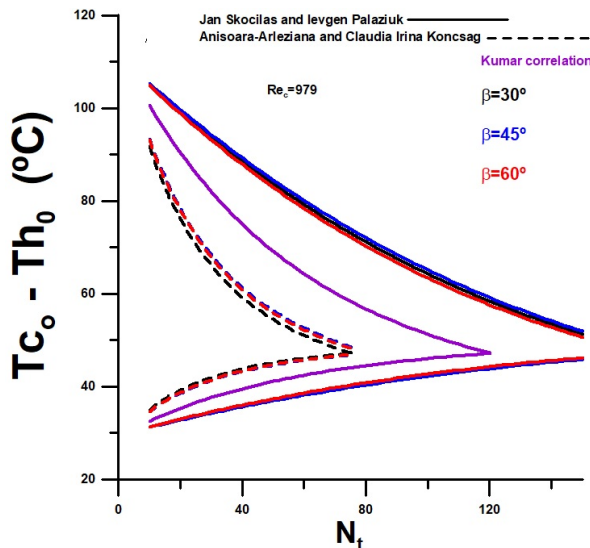


FIGURE 14. Outlet temperatures of fluids versus the number of plates for Reynolds number equal to 979 and with inclination angle as a parameter [1, 2].

The graphical results presented in Figures 14 and 15 show the outlet temperatures for the cold and hot fluids as a function of Reynolds numbers equal to $Re_c = 979$ and $Re_c = 1530$, respectively, with slope angles as parameters. The number of plate limit depends on the model used in the analysis since the second law of thermodynamics imposes a physical limitation. It is observed that this limit depends on the flow rates of the fluids and, again, is not much influenced by the chevron tilt angle. As the model presented by Neagu and Koncsag [2] significantly approaches 100% of effectiveness (ϵ_1) for both Reynolds numbers under analysis, the maximum possible number of plates is the smallest among the models. In this specific case, the maximum number of plates for

Reynolds number equal to $Re_c = 979$ is $N_t = 78$, and for Reynolds number equal to $Re_c = 1530$, $N_t = 82$. When it comes to the Kumar model, you can see that the limiting numbers are equal to $N_t = 120$ and $N_t = 122$. As the effectiveness is very low in the case of the model developed by Skočilas and Palaziuk [1], the maximum numbers for both flows under analysis are above $N_t = 150$.

5. CONCLUSION

The work analysed the influence of the chevron plate inclination angle on the thermal performance of a Gasket plate heat exchanger. Three models were used to determine the Nusselt number through theoretical and experimental correlations. The models were developed by Kumar, Skočilas and Palaziuk [1], and Neagu and Koncsag [2].

Regarding the analysed models, there is a great difference between them. It can be said that the values obtained by the authors are very different from each other. And in this sense, it is concluded that the maximum flow rate and the limit number of plates to be used in the heat exchanger strongly depend on the used model.

Based on the results presented, the model developed by Neagu and Koncsag [2] is the most efficient and effective. It obtains final results for exit temperatures very close to the other models, developed by Kumar and Skočilas and Palaziuk [1], with a smaller number of plates and a lower flow rate for the cold fluid. The model developed by Kumar does not explicitly consider the inclination angle, and the results obtained are intermediate to the other two and slightly approach the model developed by Neagu and Koncsag [2] for high flow rates.

The flow rate variation is more significant as an influence on the thermal performance of the heat ex-

changer than the angle of inclination, and the number of plates to be used in the heat exchanger are the other main factors responsible for the thermal performance.

The number of plates used in reference [2], $N_t = 63$, is quite adequate, following the analyses performed.

Based on the results obtained, the need for new theoretical and experimental works related to the influence of chevron inclination angles is evident.

LIST OF SYMBOLS

A_{ch} channel cross-sectional free flow area [m²]
 A_e heat transfer total area [m²]
 $A_{ch\ sine}$ channel cross-section transverse to the furrow [m²]
 b corrugation depth [m]
 C_{pc} specific heat of the cold fluid [J/(kg K)]
 C_{ph} specific heat of the hot fluid [J/(kg K)]
 C_h thermal capacity of the hot fluid [W/K]
 C_{min} minimum thermal capacity between the hot and cold fluids [W/K]
 $C^* = C_{min}/C_{max}$
 D_h hydraulic diameter [m]
 $D_{h\ sine}$ hydraulic dynamic diameter of a sine duct [m]
 D_P port diameter [m]
 f_{app} apparent friction coefficient
 G_{ch} mass velocity of the hot fluid [kg/(m² s)]
 G_{cc} mass velocity of the cold fluid [kg/(m² s)]
 h_h coefficient of heat convection for hot fluid [W/(m² K)]
 h_c coefficient of heat convection for cold fluid [W/(m² K)]
 $h_{c\ sine}$ coefficient of heat convection for cold fluid [W/(m² K)]
 $h_{h\ sine}$ coefficient of heat convection for hot fluid [W/(m² K)]
 k_h thermal conductivity of the hot fluid [W/(m K)]
 k_c thermal conductivity of the cold fluid [W/(m K)]
 k_W thermal conductivity of the plate [W/(m K)]
 l the corrugation wavelength
 L_C compressed plate pack length [m]
 L_h horizontal length between centres of ports [m]
 L_p plate length between ports [m]
 L_V vertical distance between centres of ports [m]
 L_w plate width [m]
 L_{furr} furrow flow components [m]
 L_{long} longitudinal flow components [m]
 \dot{m}_{ch} mass flow rate per channel [kg/s]
 \dot{m}_c total mass flow rate of the cold fluid [kg/s]
 \dot{m}_h total mass flow rate of the hot fluid [kg/s]
 N_{cp} number of channels for one pass
 N_e effective heat transfer number of plates
 N_p number of fluid passes
 N_t number of plates
 Nu_c Nusselt number for cold fluid
 Nu_h Nusselt number for hot fluid
 $Nu_{c\ sine}$ Nusselt number for cold fluid for a sine duct
 $Nu_{h\ sine}$ Nusselt number for hot fluid for a sine duct

Pr_c is the Prandtl number of the cold fluid

Pr_h is the Prandtl number of the hot fluid

Pit plate pitch [m]

\dot{Q} actual heat transfer rate [W]

\dot{Q}_{max} maximum heat transfer rate [W]

\dot{Q}_{sine} actual heat transfer rate [W]

Re_c Reynolds number for cold fluid

Re_h Reynolds number for hot fluid

Re_{sinec} Reynolds number for cold fluid in a sine duct

Re_{sineh} Reynolds number for hot fluid in a sine duct

T_{ci} inlet temperature of water [°C]

T_{hi} inlet temperature of vegetable oil [°C]

T_{co} outlet temperature for cold fluid [°C]

T_{ho} outlet temperature for hot fluid [°C]

U_o global heat transfer coefficient [W/(m² K)]

U_{osine} global heat transfer coefficient of a duct sine [W/(m² K)]

Greek symbols

α_c thermal diffusivity of the cold fluid [m²/s]

β corrugation angle of the plate

φ area enlargement factor

ρ density of the fluid [kg/m³]

μ dynamic viscosity of fluid [kg/(m s)]

ν_c the kinematic viscosity of the cold fluid [m²/s]

ε effectiveness

Acronyms

CFD computational fluid dynamics

GPHE gasket plate heat exchanger

NTU number of thermal units

REFERENCES

- [1] J. Skočilas, I. Palaziuk. CFD simulation of the heat transfer process in a chevron plate heat exchanger using the SST turbulence model. *Acta Polytechnica* **55**(4):267–274, 2015. <https://doi.org/10.14311/AP.2015.55.0267>.
- [2] A.-A. Neagu, C. I. Koncsag. Model validation for the heat transfer in gasket plate heat exchangers working with vegetable oils. *Processes* **10**(1):102, 2022. <https://doi.org/10.3390/pr10010102>.
- [3] S. Kakaç, H. Liu, A. Pramuanjaroenkij. *Heat Exchangers – Selection, Rating, and Thermal Design*. CRC Press, Taylor & Francis Groupe, Boca Raton, London, New York, 3rd edn., 2012.
- [4] E. Nogueira. Entropy generation analysis in a gasket plate heat exchanger using non-spherical shape of alumina boehmite nanoparticles. *Ovidius University Annals of Chemistry* **33**(1):41–49, 2022. <https://doi.org/10.2478/auoc-2022-0006>.
- [5] L. Tovazhnyanskyy, J. J. Klemeš, P. Kapustenko, et al. Optimal design of welded plate heat exchanger for ammonia synthesis column: An experimental study with mathematical optimisation. *Energies* **13**(11):2847, 2020. <https://doi.org/10.3390/en13112847>.
- [6] D. H. Nguyen, K. M. Kim, T. T. Nguyen Vo, et al. Improvement of thermal-hydraulic performance of plate heat exchanger by electroless nickel, copper and silver

- plating. *Case Studies in Thermal Engineering* **23**:100797, 2021. <https://doi.org/10.1016/j.csite.2020.100797>.
- [7] B. Kumar, S. N. Singh. Hydraulic and thermal studies on a chevron type plate heat exchanger. *Thermal Science* **22**(6):2759–2770, 2018. <https://doi.org/10.2298/TSCI160324312K>.
- [8] G. Roxana, P. Sorin, H. Aneta, H. Gheorghe. Study regarding numerical simulation of counter flow plate heat exchanger. In J. Awrejcewicz (ed.), *Numerical Analysis*. IntechOpen, Rijeka, 2011. ISBN 978-953-307-389-7, <https://doi.org/10.5772/24113>.
- [9] M. A. Jamil, T. S. Goraya, H. Yaqoob, et al. Exergoeconomic and normalized sensitivity analysis of plate heat exchangers: A theoretical framework with application. In L. C. Gómez, V. M. V. Flores, M. N. Procopio (eds.), *Heat Exchangers*, chap. 1. IntechOpen, Rijeka, 2021. <https://doi.org/10.5772/intechopen.99736>.
- [10] D. dos S. Ferreira, M. Mantelli, F. Milanese. Wilson plot method to obtain nusselt number for a plate heat exchanger. *Engenharia Térmica (Thermal Engineering)* **19**(2):25–30, 2020. <https://doi.org/10.5380/reterm.v19i2.78610>.
- [11] F. A. Mota, E. Carvalho, M. A. Ravagnani. Modeling and design of plate heat exchanger. In S. N. Kazi (ed.), *Heat Transfer*, chap. 7. IntechOpen, Rijeka, 2015. <https://doi.org/10.5772/60885>.
- [12] G. Anusha, P. S. Kishore. Heat transfer analysis of gasketed plate heat exchanger. *International Journal of Engineering Research* **5**(12):943–947, 2016. <https://doi.org/10.17950/ijer/v5s12/1215>.
- [13] K. Harshal, S. P. Dilpak, V. M. Kundalik. Design optimization algorithm for plate heat exchanger. *International Journal of Current Engineering and Technology* (Special Issue 4):149–155, 2016. <https://doi.org/10.14741/Ijcet/22774106/sp1.4.2016.31>.

DESIGN AND SIMULATION OF A BEARING HOUSING AEROSPACE COMPONENT FROM TITANIUM ALLOY (Ti6Al4V) FOR ADDITIVE MANUFACTURING

MOSES OYESOLA^a, KHUMBULANI MPOFU^a, ILESANMI DANIYAN^{a,*},
NTOMBI MATHE^b

^a Tshwane University of Technology, Department of Industrial Engineering, Staatsartillerie Road, Private Bag X680, Pretoria 0001, South Africa

^b National Laser Centre, Council for Scientific and Industrial Research, Laser Enabled Manufacturing, P. O. Box 395, Pretoria 0001, South Africa

* corresponding author: afolabiilesanmi@yahoo.com

ABSTRACT.

In evaluating emerging technology, such as additive manufacturing, it is important to analyse the impact of the manufacturing process on efficiency in an objective and quantifiable manner. This study deals with the design and simulation of a bearing housing made from titanium alloy (Ti6Al4V) using the selective laser melting (SLM) technique. The Finite Element Analysis (FEA) method was used for assessing the suitability of Ti6Al4V for aerospace application. The choice of Ti6Al4V is due to the comparative advantage of its strength-to-weight ratio. The implicit and explicit modules of the Abaqus software were employed for the non-linear and linear analyses of the component part. The results obtained revealed that the titanium alloy (Ti6Al4V) sufficiently meets the design, functional and service requirements of the bearing housing component produced for aerospace application. The designed bearing is suitable for a high speed and temperature application beyond 1900 K, while the maximum stress induced in the component during loading was 521 kPa. It is evident that the developed stresses do not result in a distortion or deformation of the material with yield strength in the region of 820 MPa. This work provides design data for the development of a bearing housing for AM under the technique of SLM using Ti6Al4V by reflecting the knowledge of the material behaviour under the operating conditions.

KEYWORDS: Additive manufacturing, bearing housing, FEA, titanium alloy.

1. INTRODUCTION

In evaluating emerging technology such as additive manufacturing, it is important to analyse the impact of the manufacturing process on efficiency in an objective and quantifiable manner. Over the years, several production methods, such as casting and conventional machining, have been used for the development of the high-value bearing housing component. However, the quest for efficiency in line with the Fourth Industrial Revolution (FIR) has brought about recent advancement in the use of additive manufacturing (AM), specifically the selective laser melting (SLM) process. Component simulations are very important in determining generic performances and can provide a comprehensive way to understand the behaviour of components or a material in service before the manufacturing process [1]. The process is usually iterative, thus, paving the way for adjustments of the process conditions in order to come up with the best component design that will meet the required service and functional requirements. This approach provides the required control right from the design phase in order to prevent expensive reworks. The use of titanium alloy is increasingly gaining widespread attention across the

fields of aerospace, medical, and automotive engineering, and many more, due to its excellent mechanical properties. In the field of aerospace, titanium alloy has been used for many years mostly due to its mechanical properties advantage [1–3]. Commercially, among the benefits that either titanium alloys or pure titanium offers as a material are high strength-to-weight ratio (density being 60 % of steel), light weight, and outstanding temperature strength [4]. Furthermore, Ti6Al4V is the most commonly used titanium alloy where high reliability is required due to its superior mechanical properties to others [4]. Similarly, the demand for titanium in manufacturing processes is growing with the target for sustainability of aircraft metal parts production owing to its environmental friendliness [5]. The properties of the titanium alloy depend on the microstructure, the size and arrangement of the alpha and beta ($\alpha + \beta$)-alloys phase where temperature is one of the factors that can significantly alter the microstructure coordination [6–8]. Hence, the quest for components supporting high-performing and light-weight bearings in aerospace applications require proper design, simulations and a good quality operation prediction control.

Bearings are components that find applications in the shaft of the aircraft engines, accessory gear box, landing gear, aircraft turbine, and numerous other places of use. Bearings used in any type of aerospace machinery must meet strict standards for material and quality control due to the harsh environments of operation. There are material standards, testing requirements, and required traceability on all parts. One of the characteristics required for bearings of a jet engine main shaft is the auxiliary power units for absorbing stress and providing support for loads [9]. The key characteristics required for the bearings in a jet engine main shaft are:

- suitability for high-speed rotation,
- high operating temperature,
- high reliability and traceability.

The main features of a bearing in its housing are in three forms, namely; bearing types (three-point contact ball or cylindrical roller), bearing material, and bearing design. Recent jet engines are designed to operate at higher temperatures and pressures for a lower fuel consumption, and to have a lighter weight [9]. These are key requirements in the quest for sustainability in terms of energy consumption and environmental friendliness as well as in the operational performance of the aircraft. The structure of the bearings for jet engine main shafts is becoming more complicated, hence reliability of the bearing housing must be improved. This important development task is being pursued on several fronts as in this study for AM [10]. To accommodate the wide variety of performance characteristics designs and manufactures, the development of bearing with a high reliability is necessary. The usual production methods of a bearing and its housing since ages-wise are through conventional machining and casting techniques [11]. The development of a bearing housing through the conventional means are met with some challenges, which can be suitably addressed with the use of AM technologies. For instance, the dynamics of service requirements necessitates the development of a bearing housing with improved quality. The improvement in the quality often requires some degree of flexibility during the design and manufacturing phase. Compared to the conventional methods, the AM technologies provide a high degree of flexibility tolerance during the product development. Furthermore, the Laser-Powder Bed Fusion (L-PBF) of Additive Manufacturing technology known as Selective Laser Melting (SLM) has gained an increased attention in recent years due to the ability of the process to produce near-net shape parts directly from CAD files without the retooling cost associated with casting or forging [11]. This makes the process considerable cost-and-time effective as compared to the conventional means. With SLM, traditional manufacturing processes, such as cutting, milling and grinding will not be necessary. Benefits include:

- (1.) new designs not possible using conventional subtractive technology,
- (2.) dramatic savings in time, materials, waste, energy and other costs of producing new components,
- (3.) significant reductions in environmental impact,
- (4.) faster time-to-market.

SLM builds up finished components from a raw material powder, layer by layer, through laser melting. Hence, the performance consideration of the process towards producing the referenced component of bearing housing directly.

The aircraft engine operates at very high temperatures, hence, a bearing part development must take into consideration the use of process that retains excellent mechanical properties at high temperatures such as the SLM. This is because a high temperature can promote cyclic stress and fatigue that can cause the bearing support to fail catastrophically in service. Furthermore, bearings developed for aircraft applications should be suitable for high speed rotation with excellent fracture strength to withstand the stress developed [12]. The desirable mechanical properties that must meet the required service conditions include; excellent wear resistance, hot-hardness, high strength-to-weight ratio [12]. While the design takes account of the suitable specifications for the required service conditions, the Finite Element Analysis (FEA) will examine the behaviour of the component as well as its mechanical properties under varying temperature. This will enable the manufacturer to ascertain the adequacy of the design for the required service conditions. To determine the effects of a varying dynamic response and excitation of components, a simulation model that includes specific geometric constraint assumptions needs to be developed. A simulation model of FEA that determines the dynamic response of the bearing housing component, which interpolates the solution from a set of precomputed values to provide faster results for design purpose, is required for a conformance investigation.

FEA is a powerful computer simulation tool, which has been adopted in many industries, including the aviation and automotive industry, for studying the behaviour of engineering systems under a variety of loading conditions. The reliability of a bearing housing is expected to be improved via proper design and FEA is a good quality control tool. This tool helps to determine manufacturability and heat treatment processes in order to ensure that the developed bearing component conforms to the standards. The FEA and simulation tools such as Abaqus has not only been valuable for maximising the performance of products, but also found useful applications in the development of more detailed instructions for operating and maintaining a finished component [10–12]. The SLM is one of AM technologies for metal fabrication with a processing capacity of good manufacturing accuracy and it is considered suitable for the purpose of this

work. This is because the process possesses an excellent controllability of internal complex structures for aerospace parts with large-scale and thin-walled complex structures [11].

Many works have been reported on the development of titanium alloy for aerospace applications. For instance, Zhu et al. [13] reported on the aerospace system and component design for light-weighting while Huda and Edi [14] reported on the material selection in the design of structures and engines of supersonic aircrafts. Inagaki et al. [15] reported that the use of titanium alloy for aerospace application has several merits, such as high compatibility with carbon fibre reinforced polymer, reduction in the maintenance cost, excellent fatigue strength and fracture toughness, high crack propagation, and good heat and corrosion resistance. Although the use of aluminium alloy brings about significant high strength-to-weight ratio of the aerospace component, it also has a drawback of reducing the strength of aluminium as temperature exceeds 200 °C [14, 15]. As such, aluminium alloy may fail catastrophically under the required service conditions, especially in extreme situations when the temperature exceeds the threshold. However, titanium is more suitable for high temperature applications though there is a need for the investigation of the thermal loads necessary for such service requirement because of its low thermal conductivity that can result in build-up stresses [16, 17]. The successful adoption of AM technology within the industry depends on its ability to reduce manufacturing costs and lead times without compromising the quality and mechanical properties of the finished product. In recent years, AM has had considerable successes in prototyping within the aerospace industry, permitting rapid design and product modifications, which in turn have enabled the final components to be manufactured quickly without a long lead time. In recent years, General Electric (GE) has been at the forefront of AM adoption for aircraft propulsion systems, integrating several AM technologies into new product developments. One landmark application of AM in the aerospace industry is the fabrication of individual fuel nozzles made of titanium to be used in a single commercial “Leading Edge Aviation Propulsion” (LEAP) engine by “Cubic Feet per Minute” (CFM) [18].

In terms of utilization in the aerospace industry, the primary PBF techniques comprise selective laser melting (SLM) and electron beam melting (EBM) [19]. The primary benefit of SLM and PBF, in general, is their ability to produce components of high resolution and quality, making their applications in the aerospace industry particularly useful.

In SLM, the build operation typically takes place in a vacuum or inert atmosphere (argon or nitrogen) to prevent the formation of surface oxides on the molten metal layers. The SLM process is very similar to direct metal laser sintering (DMLS) and SLS, with both undergoing a complete powder melting regime

The laser beam provides a sufficient energy to raise the powder above its melting temperature, creating a small region termed the ‘melt pool’ at an exact location that corresponds to the 2D projection of the CAD model. While SLS can utilise a range of polymers, metals, and alloy powders, and DMLS exclusively metals, SLM is primarily focused on particular metals, such as steel, aluminium, and titanium [19].

However, both DMLS and SLS lack the capability to fully melt the deposited powder material while the SLM has the ability to do so, resulting in the latter’s superior mechanical properties [20]. The primary benefit of SLM and PBF, in general, is its ability to produce components of high resolution and quality, making its applications in the aerospace industry particularly useful. In recent years, common metallic materials used to fabricate components for the aerospace industry have included tool steels and stainless steels, titanium, nickel, aluminium, and alloys of these materials [20]. Ti6Al4V alloy has gained widespread attention in the aerospace industry due to its combined properties of high strength, fracture toughness, and low density, together with a low coefficient of thermal expansion [21]. Significant efforts have been made in recent years to insert AM componentry into both structural and propulsion systems of aircrafts. Airbus used AM to produce A350 brackets from Ti6Al4V in 2014, the first metal AM components used for the interior of a commercial aircraft [21].

The objective of this paper is to perform the FEA of the bearing housing component from Ti6Al4V using the commercial software code Abaqus®.

The motivation for this work is the need to develop an aero-based component that will meet the required service and functional requirements taking into consideration all relevant effects for high speed applications. The work, therefore, employs a fast dynamic simulation model, for the investigation of the material behaviour under the thermo-mechanical loading conditions. Therefore, a minimal set of degrees of freedom, and analytical and physical motivated solutions were reviewed in this study. The novelty of this work lies in the investigation of the suitability of adopting titanium alloy for AM of a bearing housing for aerospace applications. The use of titanium alloy for aerospace application keeps emerging and has not been sufficiently highlighted in the existing literature about AM technology.

2. MATERIALS AND METHODOLOGY

The method essentially consists of assuming the piecewise continuous function for the solution by obtaining arbitrary parameters in a manner that reduces the error in the solutions. Here, the maximum yield strength in the component of the bearing housing was determined and the material was developed to a safe stress limit within the varying value of 800 to 1200 MPa. The maximum stress induced in the material should be less than allowable stress (yield stress and tensile stress)

in order to ensure a satisfactory performance in service without failure. The geometry-based modelling was employed for quick meshing of variants of the whole model and numerous sub-models. The scripting and other process automation techniques made the modelling and evaluation the results easier and faster, greatly simplifying the process of strength verification. The process of strength verification will enable the determination of the variations in the strength of the components vis-a-vis the service requirements under different operational and thermal loading conditions. This will provide an insight into the material behaviour and the point at which failure is imminent. One of the merits of the modelling and simulation tool is that such variations in the critical parameter of the designed component can be estimated numerically and compared with the mechanical properties of the material, thus, making the verification process relatively reliable. The considered component life cycle design is for a proprietary bearing housing component (M50-FC200) with the approach to achieving a longer service life if AM is employed for manufacturing of the part. The state of the art computational tool utilised for the analysis of titanium alloy – Ti6Al4V material response, is FEA. The simulation tool employed for the part design is Abaqus© software 2017 suite, the Abaqus/standard analysis tool in the complete Abaqus environment and Solidworks®. A sequence of design steps, tailored assessments of the material, is made to suitably evaluate the manufacturability requirements of the product. The part is developed in CAD model and uses FEA to obtain the bearing housing component (M50-FC200) design.

For an aerospace application aerospace, the LPBF technique considered in this study is the SLM. The primary benefit of SLM is its ability to produce components of high resolution and quality, making its application in the aerospace industry particularly useful [7–10]. The use of SLM, being a technique of LPBF, assures the production of fully dense parts with high-quality and near-net shape. Therefore, it is perfectly suitable to meet strict requirements of the high-strength titanium alloys used in the aerospace; as examined in this study. The choice of Ti6Al4V stems from its high strength-to-weight ratio and excellent resistance to corrosion (in aqueous solutions, oxidizing acids, chlorides, rocket propellants and alkalis). It also resists to creep, remains strong and fracture-tough. This makes it a suitable candidate material for aerospace applications [22–24].

The implementation of near- β titanium alloys in a commercial aircraft, namely, Ti-10-2-3, Ti-15-3-3-3, and VT 22 (Ti-5Al-5V-5Mo-1Cr-1Fe, Ti-6Al-4V), which are all still used in the aerospace today, has been reported. In particular, Ti-10-2-3 has proved to be one of the most forgeable β -titanium alloys (low flow stresses), and it also exhibits a high resistance to edge cracking [25–27]. However, the strength-to-weight ratio of Ti6Al4V, coupled with its forgeability

and high resistance to edge cracking, are strong advantages of the material vis-à-vis the aerospace requirements. These characteristics enable significant time-reductions between reheats, reduce labour-intensive conditioning operations, increase materials yield, improve efficiency, and lower processing costs.

The simulation performance in this study is benchmarked against characteristics of strain rates, which occur over a wide range of Ti-alloys in commercial aircraft applications [25–27].

The comprehensive FEA simulation performed for the Ti6Al4V in this study provides a mechanistic basis for reliable applications of additively manufactured bearing-housing component. In the event of any pores developing during the production, the pores can be eliminated by using defects-free raw materials, optimising the processing parameters, and implementing a suitable post-processing treatment.

The chemical composition corresponding to ISO 5832-3 as well as the mechanical and electrical properties of the titanium alloy (Ti-6Al-4V) are presented in Tables 1 and 2, respectively.

Element	Al	Fe	O	Ti	V
Percent weight [wt %]	6	0.25	0.2	90	4

TABLE 1. Chemical composition of titanium alloy (Ti-6Al-4V) [28].

S/N	Properties	Value
Mechanical		
1.	Yield strength	880 MPa
2.	Ultimate tensile strength	950 MPa
3.	Bulk modulus	150 GPa
4.	Modulus of elasticity	113.8 GPa
5.	Shear strength	550 MPa
Electrical		
1.	Specific heat capacity	553 J/kg K
2.	Thermal conductivity	7.1 W/m K
3.	Melting point	1878 K
4.	Coefficient of thermal expansion	$8.7 \times 10^{-6} \text{ K}^{-1}$

TABLE 2. Thermo-mechanical and electrical properties of titanium alloy (Ti-6Al-4V) [28].

Theoretical and numerical FEA models were then constructed and compared to the experimentally acquired data to assess the validity of the models and their efficacy in predicting the thermal behaviour of the designed component. The design considerations include the suitability for high speed and temperature application as well as high strength to support the load and absorb the induced stress [17]. The bearing was subjected to a working temperature ranging

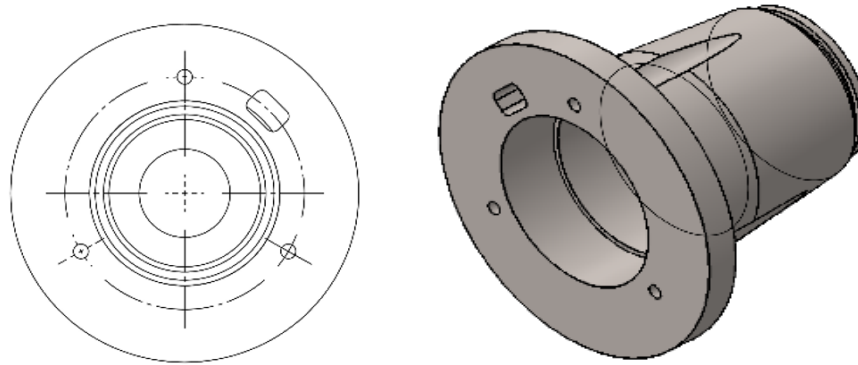


FIGURE 1. The 3D CAD models generated for the bearing housing.

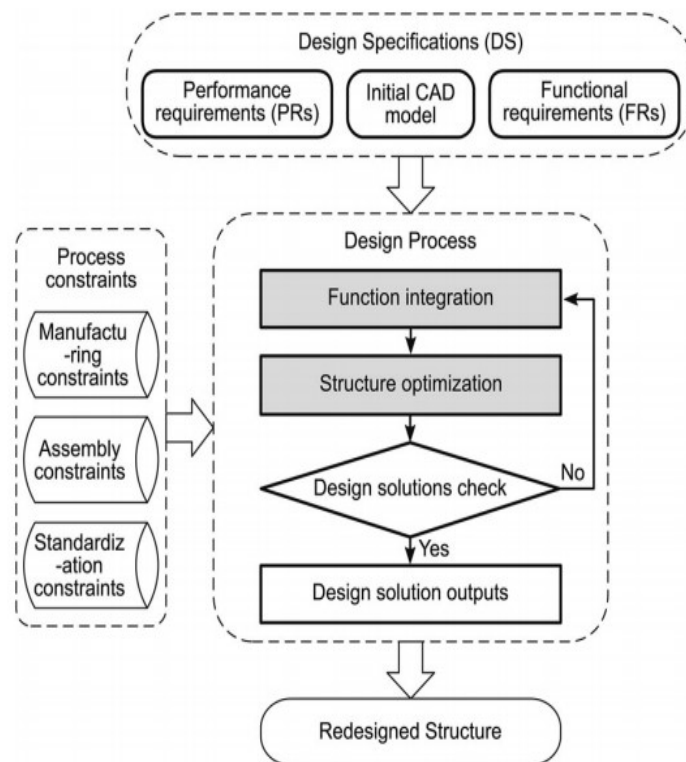


FIGURE 2. AM-enabled design method proposed by Yang and Zhao [29].

between 573.15–623.15 K. This is because the bearings of the aircraft engine main shafts are exposed to a temperature of approximately 473.15 K during the operation. The turbine remains in the heat soak retaining heat without any escape even after the engine stops, thereby raising the bearing temperature to over 573.15 K. Hence, the modelling and simulation package of the Abaqus is employed to study the stress and temperature distribution of the bearing in order to determine its mechanical behaviour under high temperatures. The modelling process starts with the generation of 3D CAD models that accurately mimic the components to be studied (Figure 2).

In assessing the suitability of a product idea for production in AM, usually, a mapping of data between materials and process, geometrical structure and behavioural properties, is carried out in order

to ensure a better manufacturing. Likewise, a CAD model in Design for Manufacture (DfAM), which is particularly used for the design plan, is introduced in this section as the hypothetical case of the bearing housing component. The parametric CAD model of the mentioned bearing housing is developed and used in determining the functionality based on the part in the software package of Abaqus FEA. Firstly, the four main parameters of flexural bearing housing geometry were identified, these include the outer diameter, and the thickness according to the dictates of the technical drawing for the component. The CAD model is developed from a proprietary technical chart (M50-FC200) of aircraft application using Solidworks® as shown in Figure 1.

The Von Mises stress analysis was used as the failure criterion during the finite element analysis carried

out with the aid of the modelling and simulation tool (Abaqus). The failure of the material occurs at a point in a member when the distortion strain energy in a bi-axial stress system reaches the limiting distortion energy. At this point, the material starts yielding to further application of load. The maximum distortion energy for yielding is expressed as Equation (1):

$$(\sigma t_1)^2 + (\sigma t_2)^2 - 2\sigma t_1 \times \sigma t_2 = \left(\frac{\sigma y_t}{\text{F.S.}}\right)^2, \quad (1)$$

where: σt_1 is the maximum principal stress (N/m^2), σt_2 is the minimum principal stress (N/m^2), σy_t is the stress at yield point (N/m^2) and F.S. is the factor of safety.

In order to investigate the suitability of production based on Laser Melting of AM, a simulation was conducted using the aggregated parameters in Tables 1 and 2. The version of the Abaqus for the modelling and simulation was employed for the titanium alloy and the bearing housing model. The objectives for the simulation approach are to reduce and complement exhaustive pre-study experiments and costs implication. Given the physical and analytical structural dynamics modelling in this study, the mathematical models are further expressed using governing equations. To denote the arbitrary reference point for the mechanical-to-thermal field coupling in the SLM [11], the thermal transfer at material point r , determined in Lagrangian domain, is denoted in Equation (2):

$$\rho \frac{dH(r, t)}{dt} = -\nabla \cdot q(r, t), \quad r \in \Omega, \quad (2)$$

where ρ is the material density (kg/m^3), H is the enthalpy (J), t is time (s), q is the heat flux vector (W/m^2) and q is the volumetric heat input (J/K/m^3). Assuming a linear dependence of the heat flux on the temperature gradient, i.e., Fourier's law, the heat flux vector can be determined from Equation (3):

$$q = -k(T) \nabla T(r, t), \quad (3)$$

where k is the thermal conductivity ($\text{W/m/}^\circ\text{C}$), assumed to be isotropic, T is the temperature (K). The temporal rate of enthalpy can be written as Equation (4):

$$\frac{dH(r, t)}{dt} = C_p(T) \frac{dT(r, t)}{dt}, \quad (4)$$

where C_p is the specific heat (J/g K). The volumetric heat input q in Equation (2) is the heat energy input, which plays a key role in the determination of the amount of heat needed to cause melting of the starting powders in the SLM process modelling. The meshing of the bearing housing at different orientations in order to predict the material's behaviour are described in the Results and discussion section.

2.1. MANUFACTURABILITY ANALYSIS AND AM DESIGN RULES

AM design rule collections ensuring manufacturability and approaches related to AM design potentials for development of innovative solutions must be taken into account. While AM provides huge design potentials, geometric freedom is not unlimited. In the literature, design rule catalogues can be found particularly for SLM. The geometric limits imposed by SLM are based on series of experiments and design for manufacturing. Munguia et al. [30] use an advice system based on artificial intelligence to compare additive and conventional manufacturing in order to recommend optimal production parameters. The second category aims at choosing an optimal production strategy depending on product requirements and process limitations.

Depending on manufacturability indexes calculated by design parameters, a CAD model is divided into a modular structure whose parts are manufactured separately and which are then assembled. Due to the novelty of AM for designers and producers, the selection of appropriate candidates remains a challenge. Figure 2 presents the AM-enabled design method proposed by Yang and Zhao [29]. The design method presents the basic process constraints, which encompass the manufacturing, assembly and standardisation constraints as pre-conditions for the process design. These constraints are integrated into the design process loop as presented in the Figure 2. The framework identifies the performance and functional requirements as two critical requirements that should be addressed by the process design. The functional integration can be achieved via the structural optimisation and the process is looped until the required design solution is obtained. The computer-aided modelling and simulation approach is often suitable for a performance evaluation of the designed solution (solution check) before proceeding to the final stage of manufacturing. This is because the approach is iterative and often allows the structural optimisation and adjustment of the design parameters and constraints until the final solution converges and the desired requirements are met. In addition, the modelling and simulation of the designed solution at this stage will promote the overall cost and time effectiveness of the overall process, thereby bringing about the development of components with high integrity without the need for expensive reworks. The designed solution output can also be compared with the ideal solution in order to estimate the design error and its level of permissibility.

Concurrent engineering has been a useful methodology that takes into account the attributes of each different stages of product's life cycle simultaneously. It is used to integrate all activities of functional analysis and requirement engineering, design, and manufacturing in parallel during the design stage as an integrated design. Several authors have reported on the difficulties in getting a Laser Powder Bed Fusion part of SLM when the dimensions are large (280 mm by 280 mm).

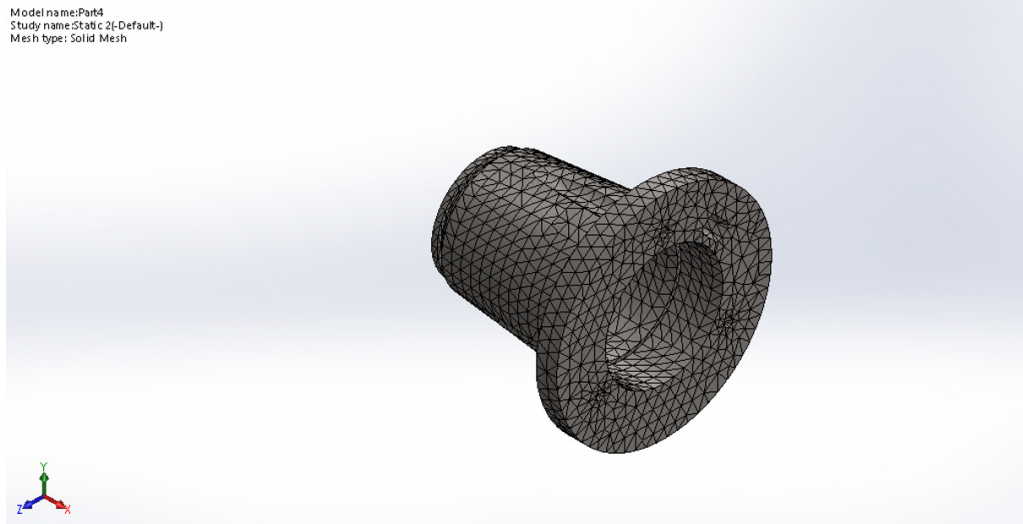


FIGURE 3. Component solid mesh.

This is because cracks usually occur due to internal stresses and this accounts for the reason why a lot of post-processing is needed to avoid cracking, like stress relieving and hot isostatic pressing [31].

The mathematical formulation of variables for the bearing housing orientation angles and layer thickness is expressed in Equation (5):

$$x = \{\theta_x, \theta_y, \theta_z, L_t\}, \quad (5)$$

where: $\theta_x, \theta_y, \theta_z$ signifies the part orientation with respect to angles between the part in x , y , and z axes. The angles show the orientation of the part in the build area while L_t is the layer thickness required during fabrication, the layer thickness value is between L_t min and L_t max.

2.2. THE FINITE ELEMENT ANALYSIS

Finite Element Analysis (FEA) is a method based on homogenised pictures, employed to better understand the underlying consolidation part of product development. The method consists of assuming the piecewise continuous function for the solution and deploying the parameters of the functions in a manner that reduces errors in the solution. The simulation of the Ti-6Al-4V alloy bearing housing as mentioned was, therefore, carried out. The maximum stresses were assigned to an allowable stress of component material to obtain maximum stress design for the bearing housing.

The FEA and simulation serves to provide a precursory visualisation of the response of the developed component during its eventual commissioning for in-service operations. The simulation was carried out using operating parameters representing extreme service conditions in order to obtain some knowledge on the limits of its mechanical integrity.

The implicit module of the Abaqus software was employed for the non-linear analysis of the component part. This is because the implicit dynamic simulations can be applied to component analyses, which

are non-linear in nature. The explicit module has a suitable integrator for the formulation and analysis of a non-linear behaviour. It is an iterative process and the time increment is adjusted until the solution converges. Following the meshing of the assembly into finite elements, it was subjected to convergence simulation runs with mesh refinement feature employed for the ease of convergence. An average mesh size of 0.8 mm, which falls within the seed size stability convergence zone, was employed for cost and time efficiency. One of the assumptions is that the loading is static and that the material is subjected to the same different loading and service requirements in all its parts. A structured 8-node hexahedral mesh element type with a linear displacement and temperature advancing front using Abaqus was employed. This was selected to mesh the assembly into finite elements, and thereafter subjected to convergence simulation runs with the mesh refinement feature employed for the ease of convergence.

2.3. MESH GENERATION AND GEOMETRIC MODEL

The mesh generation and geometric model was performed using Solidworks tool to maintain computational accuracy and convergence check balance. The mesh elements parameters were carried out at the joints. The convergence check gave an indication of suitability of 2 mm as the optimum mesh geometric model. A four-node thermally-coupled tetrahedron linear displacement standard solid mesh is employed in discretising the model into finite elements. A mesh size of 2 mm is used for the analysis from node to node over the entire geometry of the model in Figure 3.

For the convergence range, an average mesh size of 2 mm, which falls within the seed size stability convergence zone, was employed, in order to strike the right balance among the computational efficiency

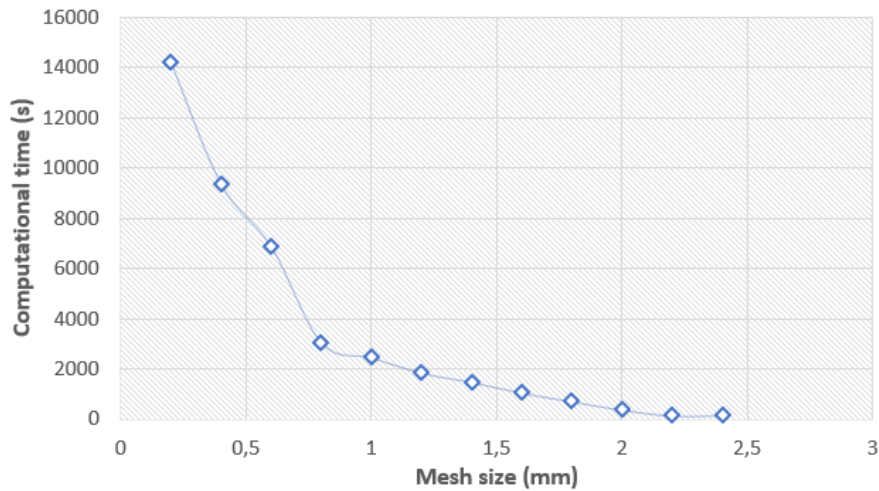


FIGURE 4. Mesh size and computational time.

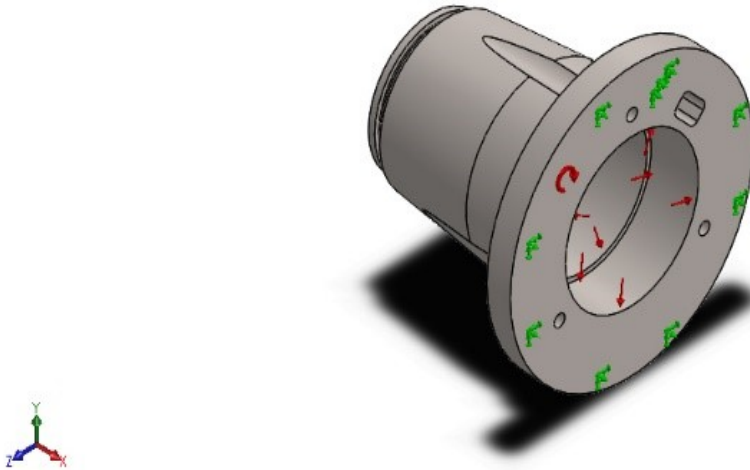


FIGURE 5. Model of the bearing housing.

and accuracy in contrast with other mesh sizes within the convergence band.

The mesh, element sizes and the convergence in the results between mesh sizes 1.8 mm and 2.4 mm indicates that any mesh size within this convergence range provides the best confidence in accuracy of the simulation result. Thus, a 2 mm mesh size was selected owing to the fact that it provided the least amount of computation time, which is very important, as time is a key factor in computer aided design and manufacturing.

The mesh size plays a vital role in the accuracy of results and computing time as it determines the number of elements involved. On this note, the computational time against the mesh size is presented using a mesh interval of 0.2 mm as presented in Figure 4. It was observed that the computational time decreases with an increase in the mesh size up to 2.2 mm. Further increase in the mesh size up to 2.4 mm resulted in

a slight increase in the computational time. Hence, the mesh size of 2.2 mm, which produced the least computational time (142 s), was selected. Figure 5 presents the model of the bearing housing.

The component is further analysed in Solidworks and assigned temperature-dependent material properties for elasticity, plasticity, and thermal response, with Ti-6Al-4V alloy selected from the material database. The guidelines for the bearings for jet engines were considered for the identification of the product's properties in relation to the service requirements [32]. The emphasis on the Ti-6Al-4V alloy is due to its main features, which are light weight, high strength (yield strength of approximately 1000 MPa), high temperature characteristics (maximum melting point for grade 5 is at 1933 K), thermal processability, fracture toughness, workability, and superior formability [33–36]. This alloy is currently the most preferred for aircraft manufacturing owing to its theo-

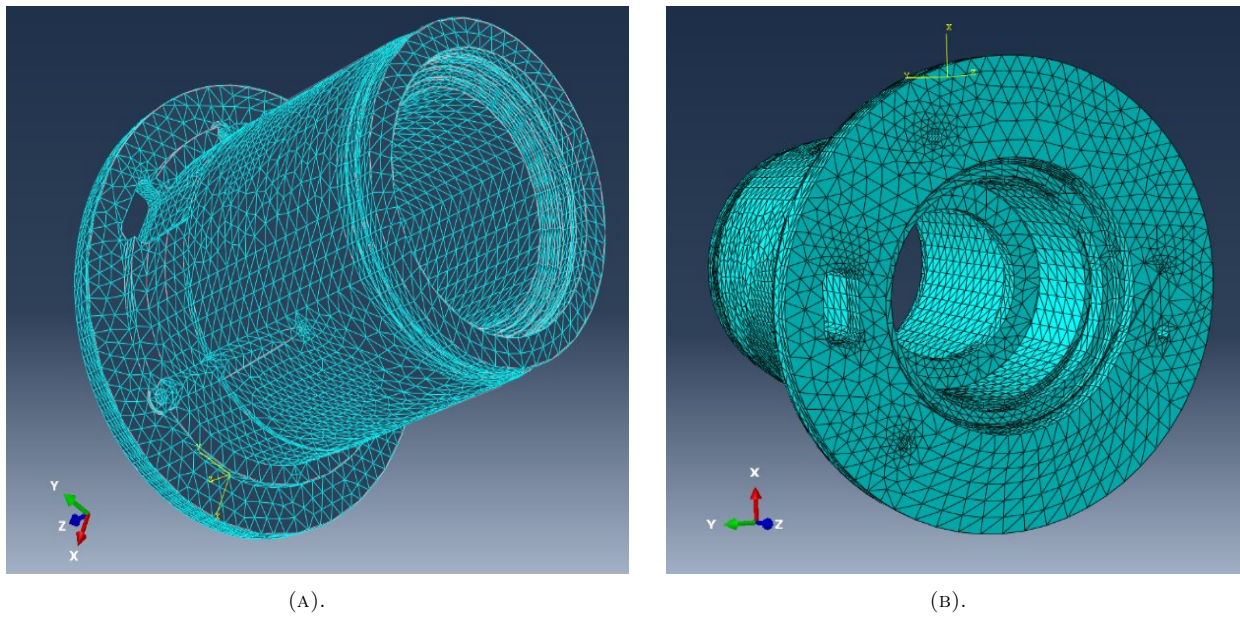


FIGURE 6. Component's mesh-based geometry as in FEA-Abaqus. (a) wireframe and (b) solid mesh.

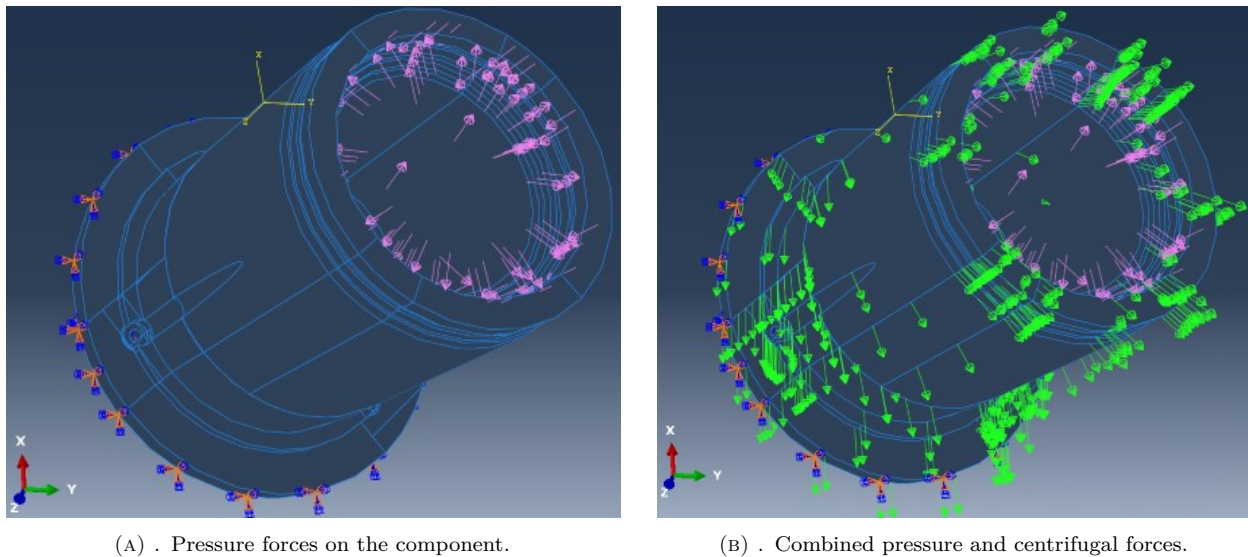


FIGURE 7. Visual mechanism acting on the bearing housing in Abaqus (a) and b).

retical chemical composition properties, good high-temperature properties and high strength-to-weight ratio [37, 38]. In addition, the availability of quantifiable data further increases its application for where the yield strength of annealed material is 825 MPa or higher, tensile strength is 895 MPa or higher, and elongation is 10% or higher at a room temperature [39].

The implicit module has a suitable integrator for the formulation and analysis of a non-linear behaviour as it is an iterative process with time increment adjustments until the solution finally converges. Following the meshing of the assembly into finite elements, it was subjected to convergence simulation runs with mesh refinement feature employed for the ease of convergence. Figure 6 present the component's mesh-based geometry as displayed in FEA-Abaqus.

2.4. PRESSURE AND CENTRIFUGAL LOADING CONDITIONS

In the operation of a typical aircraft-jet turbine engine, air is usually sucked in large volumes and compressed in the magnitudes of tons of air per second with the aid of fan and compressor in a coupled mechanism. The loads and fixtures used in the model, modelled in Solidworks, are presented in Table 3. While Figure 7 further illustrate the pressure and centrifugal forces acting on the component, modelled in Abaqus.

This understanding and philosophy of load often accounts for the centrifugal (green arrows) and pressure forces (purple arrows) acting on the components and the visual mechanism for the bearing housing is displayed in Figure 7.

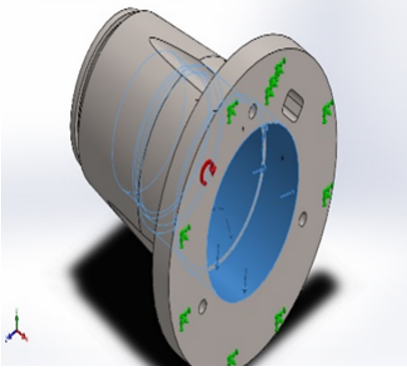
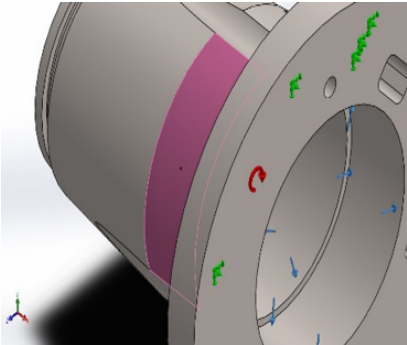
Load name	Load image	Load details
Pressure		Entities: 4 face(s) Type: Normal to selected face Value: 101 325 Units: N/m ² Phase angle: 0 Units: Deg
Centrifugal		Centrifugal, Ref: Face<1> Angular velocity: 1800 rad/s Angular acceleration: 0 rad/s ²

TABLE 3. Loads for pressure and centrifugal condition in Solidworks.

2.5. THERMAL BOUNDARY CONDITIONS

Aside from the philosophy of drawing air into the engine, the compressor also pressurizes the air, at ratios up to 40:1. This pressurised air is then delivered into the combustion chamber where it is ignited after the addition of fuel [40]. Hence, typical temperatures during this process may rise as high as 2273 K, thus accounting for the thermal stresses on components within and around the engine is critical. Typical ambient temperatures within the compressor ranges between 473 K and 1000 K [41] for the low-temperature creep behaviour of titanium. The thermal interaction for the bearing housing was further examined in Abaqus (Figure 8).

Thermal interactions were assigned to the model with the upper and lower bounds of 1973 K and 273 K, respectively, assigned as thermal boundary conditions in relation to the temperature bounds that can be experienced within the environment of the component during operation. Where the continuous flow of air or gases to which it is exposed may range from 1120 K to 1973 K. The higher temperature of 1973 K was used in the thermal analysis of the effects of convected temperature on the material as a worst-case operation scenario.

In the static general analysis, encastre boundary conditions in which all translational and rotatory motions are set at zero were assigned at the cap of the housing where it is often bolted to other components (as in Figure 8). Pressure loads of 101.325 kPa, the

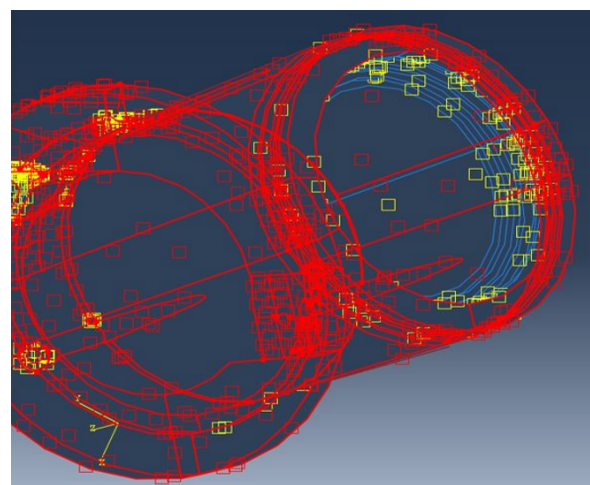
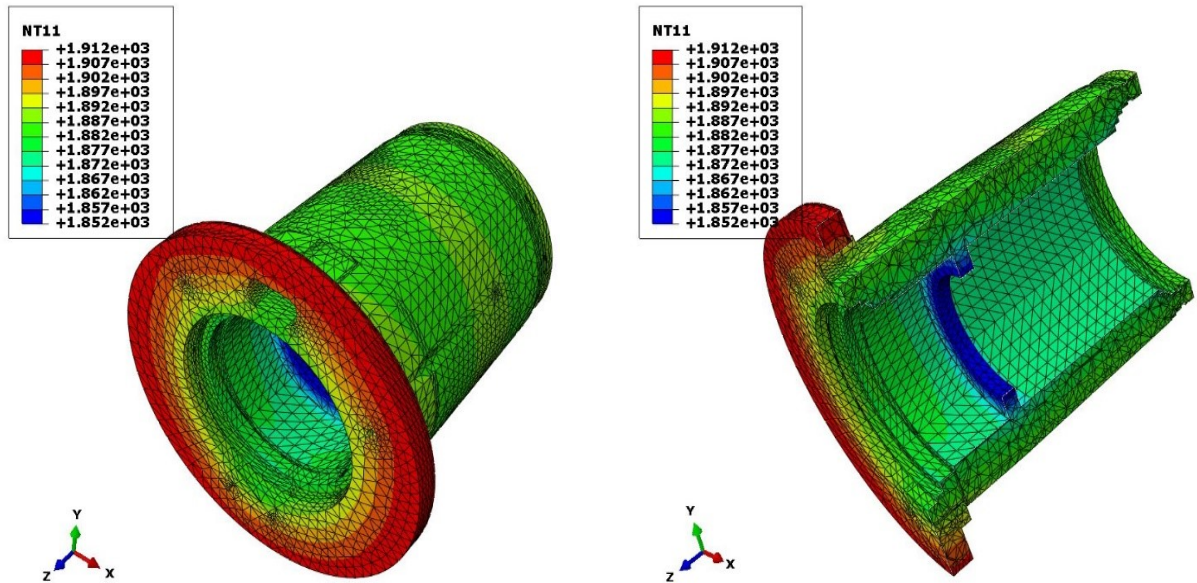


FIGURE 8. Thermal interactions for the bearing housing component.

atmospheric pressure of air at sea level, and arbitrary centrifugal load of 1800 rad/s were applied.

3. RESULTS AND DISCUSSION

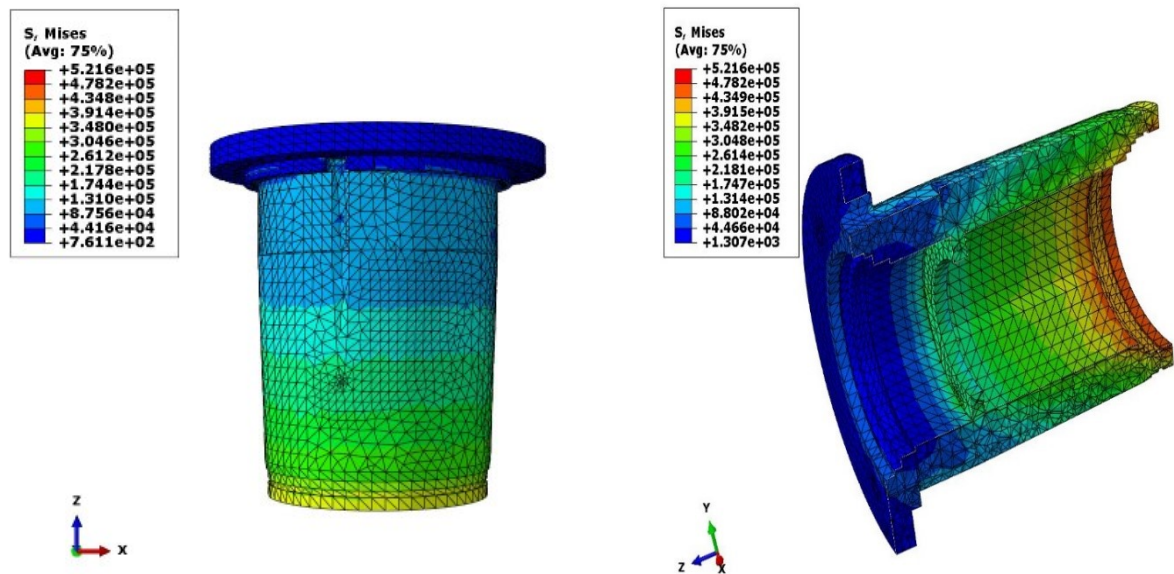
The results obtained for the Abaqus-FEA simulation are presented in Figures 9–13. The temperature distribution profile presented in Figure 9 shows the variation in temperature across the geometry of the component. The highest temperature achieved under the earlier stated thermal conditions is above 1900 K and was recorded at the periphery of the cap. A larger part of



(A) . Temperature distribution across the whole component geometry.

(B) . Temperature distribution – bilateral view of the component.

FIGURE 9. Temperature distribution on the bearing housing.



(A) . Superimposed stress distribution of thermal and pressure loading on the component.

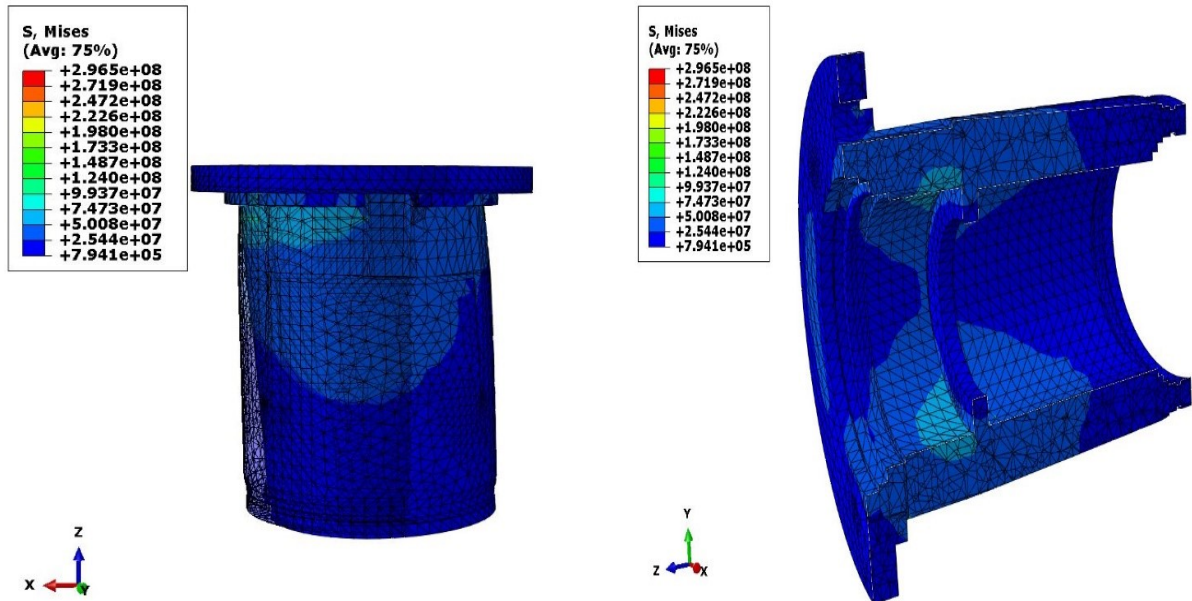
(B) . Superimposed stress distribution of thermal and pressure loading on the bilateral component.

FIGURE 10. Superimposed distribution of thermal and pressure loading.

the component does not heat up beyond 1900 K, which gives a strong indication of its ability to withstand such extreme conditions without melting, given the melting temperature of the material is about 1933 K. Figure 9 shows the temperature distribution during a steady-state operation.

The response of the component to external forces and loading conditions is further presented. The effects of the mechanical loading regimes have been compared to investigate the material’s responses to the applied forces. Both the Von Mises stress profile

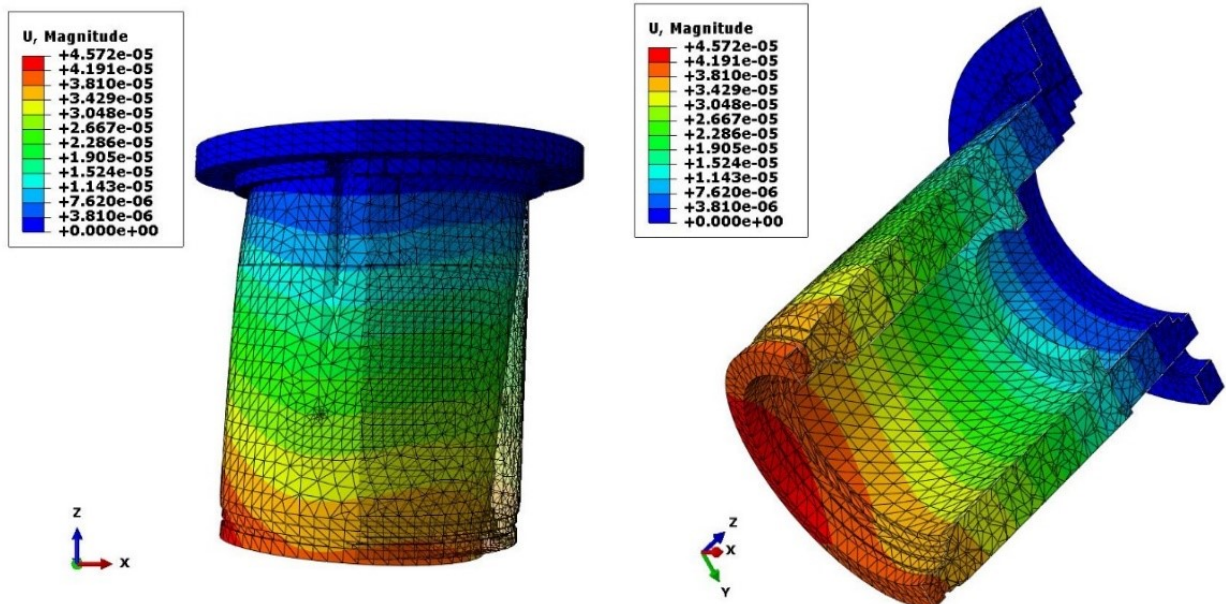
within the part and the magnitude do not pose any threats to the life or performance of the material under the reference operating conditions. Figure 10 shows the stresses developed due to air flow pressures and heat transfer, which are within a kilopascal range with the maximum Von Mises stresses being about 521 kPa. It is evident that the stresses developed do not result in a distortion or deformation of a material with yield strength in the region of 820 MPa. Figure 10 is the superimposed deformed or undeformed stress distri-



(A) . Superimposed stress distribution of thermal, pressure and centrifugal loading on the component.

(B) . Superimposed stress distribution of thermal, pressure and centrifugal loading on the bilateral component.

FIGURE 11. Superimposed deformed/undeformed stress distribution.



(A) . Superimposed displacement due to thermal, pressure, and centrifugal loading on the component.

(B) . Superimposed displacement due to thermal, pressure, and centrifugal loading on component bilateral.

FIGURE 12. Superimposed deformed/undeformed displacement due to coupled thermal, pressure and centrifugal loading.

bution due to coupled thermal and pressure loading only.

Remarkably, the contribution of centrifugal forces was found to be of significant magnitude as presented in Figure 11, as evidenced by its ability to raise the Von Mises stress three (3) orders higher than when they are suppressed. In addition, Von Mises stresses up to about 300 MPa are obtainable, which indicates that components experience some deformation. This is largely due to the torsional moments associated with

the centrifugal forces applied on the part. The superimposed deformed or undeformed stress distribution due to the coupled thermal, pressure and centrifugal loading is presented in Figure 11.

The displacements due to the deformation are presented in Figure 12, where the maximum displacement of 0.0457 mm is recorded at the free end of the part. This implies that the displacement due to the deformation is minimal.

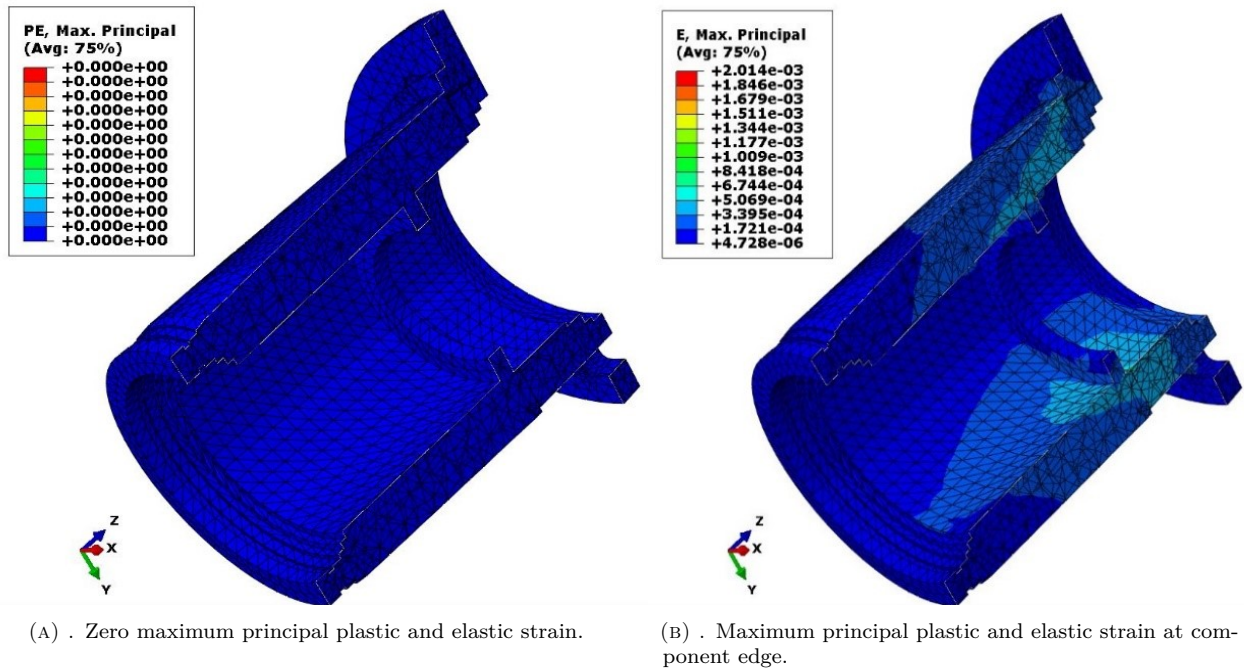


FIGURE 13. Maximum principal plastic and elastic strains due to coupled thermal, pressure and centrifugal loading.

Results, as shown in Figure 12, indicate the different aggregation of loads that may cause a slight displacement with magnitudes of the deformation attributable to the centrifugal loading regime imposed on the component while in service. Inferably, higher magnitudes of imposed loads than the ones considered could hypothetically amount to pushing the component's integrity beyond safe limits. Just like in every engineering material, loads that will push stress levels of the component beyond its yield strength of 850 MPa are bound to cause material failure.

Figure 13 displays the nature of strain profiles recorded from the loading of the component. Figure 13a reveals predominantly the elastic straining of the material with zero plastic strains while Figure 13b shows the magnitude of the elastic strains experienced at the edge of the component.

The results obtained show that the assigned Ti6Al4V material will be suitable for usage in the prescribed conditions for which these analyses were carried out. Furthermore, the material was found to have a great capacity to withstand the nature of forces and loads applied without failing since the resultant internal stresses, strains temperatures and displacements due to deformation fall within allowable ranges

4. CONCLUSION

This work considered the modelling and simulation of titanium alloy (Ti6Al4V) bearing housing of an aircraft manufactured additively. The excellent mechanical properties, such as high strength-to-weight ratio and good wear resistance, of the titanium alloy were explored. The design and the FEA were carried out using the Abaqus modelling and simulation tool. The design considerations include the suitability

for high speed and temperature application as well as high strength to support the load and absorb the induced stresses. The results obtained indicated that the designed bearing is suitable for high speed and temperature applications beyond 1900 K, which gives a strong indication of its ability to withstand such extreme conditions without melting, given the melting temperature of the material is about 1933 K. Using the Von Mises stress criterion, the maximum stress induced in the component during loading was 521 kPa. It is evident that the stresses developed do not result in a distortion or deformation of the material with yield strength being in the region of 820 MPa. This shows a good dimensional stability without any significant deformation or failure, which makes it suitable for aerospace applications. The value of the maximum stress induced at the inner ring of the bearing was significantly lower than the yield strength of the titanium alloy employed, thus indicating that the bearing is not likely to yield to failure under the required service conditions. This work provides design data for the development of bearing components using SLM because the values are in agreement to those published for laser-assisted machining and powder-based additive manufacturing for aerospace applications. This helps to detect the critical operating conditions early at the design stage before the fabrication of the bearing housing, in order to minimize any possible expensive reworks of the rig. This work did not consider the creep performance and dwell fatigue of the material (Ti6Al4V) at an elevated temperature, thus future works can consider the investigation of the potential for creep failure and dwell fatigue at high temperatures close to 1900 K.

ACKNOWLEDGEMENTS

Research support acknowledgements goes to the Department of Science and Technology in collaboration with the Council of Scientific and Industrial Research, (DST-CSIR), and the Research Chairs (Gibela) at the Industrial Engineering Department of Tshwane University of Technology Pretoria, all situated in South Africa.

REFERENCES

- [1] S. E. Haghighi, H. Lu, G. Jian, et al. Effect of α'' martensite on the microstructure and mechanical properties of beta-type Ti-Fe-Ta alloys. *Materials & Design* **76**:47–54, 2015. <https://doi.org/10.1016/j.matdes.2015.03.028>.
- [2] S. Ehtemam-Haghighi, Y. Liu, G. Cao, L.-C. Zhang. Influence of Nb on the $\beta \rightarrow \alpha''$ martensitic phase transformation and properties of the newly designed Ti-Fe-Nb alloys. *Materials Science and Engineering: C* **60**:503–510, 2016. <https://doi.org/10.1016/j.msec.2015.11.072>.
- [3] N. Taniguchi, S. Fujibayashi, M. Takemoto, et al. Effect of pore size on bone ingrowth into porous titanium implants fabricated by additive manufacturing: An in vivo experiment. *Materials Science and Engineering: C* **59**:690–701, 2016. <https://doi.org/10.1016/j.msec.2015.10.069>.
- [4] C. Bandapalli, B. M. Sutaria, D. V. Bhatt. High speed machining of Ti-alloys—A critical review. In *Proceedings of the 1st International and 16th National Conference on Machines and Mechanisms*, pp. 324–331. 2013.
- [5] W. Habrat, M. Motyka, K. Topolski, J. Sieniawski. Evaluation of the cutting force components and the surface roughness in the milling process of micro- and nanocrystalline titanium. *Archives of Metallurgy and Materials* **61**(3):1379–1384, 2016. <https://doi.org/10.1515/amm-2016-0226>.
- [6] E. Uhlmann, R. Kersting, T. B. Klein, et al. Additive manufacturing of titanium alloy for aircraft components. *Procedia CIRP* **35**:55–60, 2015. <https://doi.org/10.1016/j.procir.2015.08.061>.
- [7] G. Kasperovich, J. Hausmann. Improvement of fatigue resistance and ductility of TiAl6V4 processed by selective laser melting. *Journal of Materials Processing Technology* **220**:202–214, 2015. <https://doi.org/10.1016/j.jmatprotec.2015.01.025>.
- [8] L. Thijs, F. Verhaeghe, T. Craeghs, et al. A study of the microstructural evolution during selective laser melting of Ti-6Al-4V. *Acta Materialia* **58**(9):3303–3312, 2010. <https://doi.org/10.1016/j.actamat.2010.02.004>.
- [9] S. Leuders, M. Thöne, A. Riemer, et al. On the mechanical behaviour of titanium alloy TiAl6V4 manufactured by selective laser melting: Fatigue resistance and crack growth performance. *International Journal of Fatigue* **48**:300–307, 2013. <https://doi.org/10.1016/j.ijfatigue.2012.11.011>.
- [10] C. Y. Yap, C. K. Chua, Z. L. Dong, et al. Review of selective laser melting: Materials and applications. *Applied Physics Reviews* **2**(4):041101, 2015. <https://doi.org/10.1063/1.4935926>.
- [11] P. Michaleris. Modeling metal deposition in heat transfer analyses of additive manufacturing processes. *Finite Elements in Analysis and Design* **86**:51–60, 2014. <https://doi.org/10.1016/j.fine.2014.04.003>.
- [12] V. Vakharia, V. K. Gupta, P. K. Kankar. Nonlinear dynamic analysis of ball bearings due to varying number of balls and centrifugal force. In P. Pennacchi (ed.), *Proceedings of the 9th IFToMM International Conference on Rotor Dynamics*, pp. 1831–1840. Springer International Publishing, Cham, 2015. https://doi.org/10.1007/978-3-319-06590-8_151.
- [13] L. Zhu, N. Li, P. Childs. Light-weighting in aerospace component and system design. *Propulsion and Power Research* **7**(2):103–119, 2018. <https://doi.org/10.1016/j.jprr.2018.04.001>.
- [14] Z. Huda, P. Edi. Materials selection in design of structures and engines of supersonic aircrafts: A review. *Materials & Design* **46**:552–560, 2013. <https://doi.org/10.1016/j.matdes.2012.10.001>.
- [15] I. Inagaki, T. Takechi, Y. Shirai, N. Ariyasu. Application and features of titanium for the aerospace industry. *Nippon Steel and Sumitomo Metal Technical Report* **106**:22–27, 2014.
- [16] H. Clemens, S. Mayer. Design, processing, microstructure, properties, and applications of advanced intermetallic TiAl alloys. *Advanced Engineering Materials* **15**(4):191–215, 2013. <https://doi.org/10.1002/adem.201200231>.
- [17] C. Veiga, J. Davim, A. Loureiro. Properties and applications of titanium alloys: A brief review. *Reviews on Advanced Materials Science* **32**(2):133–148, 2012.
- [18] GE Additive. New manufacturing milestone: 30,000 additive fuel nozzles. [2019-01-09], <https://www.ge.com/additive/blog/new-manufacturing-milestone-30000-additive-fuel-nozzles>.
- [19] X. Wang, M. Jiang, Z. Zhou, et al. 3D printing of polymer matrix composites: A review and prospective. *Composites Part B: Engineering* **110**:442–458, 2017. <https://doi.org/10.1016/j.compositesb.2016.11.034>.
- [20] D. Bourell, J. P. Kruth, M. Leu, et al. Materials for additive manufacturing. *CIRP Annals* **66**(2):659–681, 2017. <https://doi.org/10.1016/j.cirp.2017.05.009>.
- [21] L. J. Kumar, C. G. Krishnadas Nair. *Current Trends of Additive Manufacturing in the Aerospace Industry*, pp. 39–54. Springer Singapore, Singapore, 2017. https://doi.org/10.1007/978-981-10-0812-2_4.
- [22] I. Daniyan, F. Fameso, K. Mpofu, I. D. Uchegbu. Modelling and simulation of surface roughness during the turning operation of titanium alloy (Ti6Al4V). In *2022 IEEE 13th International Conference on Mechanical and Intelligent Manufacturing Technologies (ICMIMT)*, pp. 176–181. 2022. <https://doi.org/10.1109/ICMIMT55556.2022.9845252>.
- [23] I. A. Daniyan, K. Mpofu, I. Tlhabadira, B. I. Ramatsetse. Process design for milling operation of titanium alloy (Ti6Al4V) using artificial neural network. *International Journal of Mechanical Engineering and Robotics Research* **10**(11):601–611, 2021. <https://doi.org/10.18178/ijmerr.10.11.601-611>.

- [24] Numerical and experimental analysis of surface roughness during the milling operation of titanium alloy Ti6Al4V. *International Journal of Mechanical Engineering and Robotics Research* **10**(12):683–693, 2021. <https://doi.org/10.18178/ijmerr.10.12.683-693>.
- [25] S. Huang, R. L. Narayan, J. H. K. Tan, et al. Resolving the porosity-unmelted inclusion dilemma during in-situ alloying of Ti34Nb via laser powder bed fusion. *Acta Materialia* **204**:116522, 2021. <https://doi.org/10.1016/j.actamat.2020.116522>.
- [26] S. Huang, P. Kumar, W. Y. Yeong, et al. Fracture behavior of laser powder bed fusion fabricated Ti41Nb via in-situ alloying. *Acta Materialia* **225**:117593, 2022. <https://doi.org/10.1016/j.actamat.2021.117593>.
- [27] V. Chakkravarthy, M. Lakshmanan, P. Manojkumar, R. Prabhakaran. Crystallographic orientation and wear characteristics of TiN, SiC, Nb embedded Al7075 composite. *Materials Letters* **306**:130936, 2022. <https://doi.org/10.1016/j.matlet.2021.130936>.
- [28] U.S. Titanium Industry Inc. Titanium alloys – Ti6Al4V Grade 5. [2019-07-02], <https://www.azom.com/article.aspx?ArticleID=1547>.
- [29] S. Yang, Y. F. Zhao. Additive manufacturing-enabled design theory and methodology: a critical review. *The International Journal of Advanced Manufacturing Technology* **80**:327–342, 2015. <https://doi.org/10.1007/s00170-015-6994-5>.
- [30] J. Munguía, J. Lloveras, S. Llorens, T. Laoui. Development of an AI-based rapid manufacturing advice system. *International Journal of Production Research* **48**(8):2261–2278, 2010. <https://doi.org/10.1080/00207540802552675>.
- [31] M. Bici, S. Brischetto, F. Campana, et al. Development of a multifunctional panel for aerospace use through SLM additive manufacturing. *Procedia CIRP* **67**:215–220, 2018. <https://doi.org/10.1016/j.procir.2017.12.202>.
- [32] N. T. N. Matsumori. Bearings for jet engine main shafts to protect safety of aircrafts. *Tool Engineer* **54**(13):61, 2013.
- [33] A. Boschetto, L. Bottini, F. Veniali. Surface roughness and radiusing of Ti6Al4V selective laser melting-manufactured parts conditioned by barrel finishing. *The International Journal of Advanced Manufacturing Technology* **94**(5-8):2773–2790, 2018. <https://doi.org/10.1007/s00170-017-1059-6>.
- [34] I. A. Daniyan, F. Fameso, F. Ale, et al. Modelling, simulation and experimental validation of the milling operation of titanium alloy (Ti6Al4V). *The International Journal of Advanced Manufacturing Technology* **109**(7):1853–1866, 2020. <https://doi.org/10.1007/s00170-020-05714-y>.
- [35] I. Tlhabadira, I. Daniyan, L. Masu, K. Mpofu. Computer aided modelling and experimental validation for effective milling operation of titanium alloy (Ti6Al4V). *Procedia CIRP* **91**:113–120, 2020. <https://doi.org/10.1016/j.procir.2020.03.098>.
- [36] I. A. Daniyan, I. Tlhabadira, K. Mpofu, A. O. Adeodu. Development of numerical models for the prediction of temperature and surface roughness during the machining operation of titanium alloy (Ti6Al4V). *Acta Polytechnica* **60**(5):369–390, 2020. <https://doi.org/10.14311/AP.2020.60.0369>.
- [37] F. H. S. Froes. 1 - A historical perspective of titanium powder metallurgy. In M. Qian, F. H. (Sam) Froes (eds.), *Titanium Powder Metallurgy*, pp. 1–19. Butterworth-Heinemann, Boston, 2015. <https://doi.org/10.1016/B978-0-12-800054-0.00001-0>.
- [38] D. Wang, W. Dou, Y. Yang. Research on selective laser melting of Ti6Al4V: Surface morphologies, optimized processing zone, and ductility improvement mechanism. *Metals* **8**(7):471, 2018. <https://doi.org/10.3390/met8070471>.
- [39] B. Dutta, F. H. (Sam) Froes. 24 - The additive manufacturing (AM) of titanium alloys. In M. Qian, F. H. (Sam) Froes (eds.), *Titanium Powder Metallurgy*, pp. 447–468. Butterworth-Heinemann, Boston, 2015. <https://doi.org/10.1016/B978-0-12-800054-0.00024-1>.
- [40] T. Tulwin. A coupled numerical heat transfer in the transient multicycle CFD aircraft engine model. *Procedia Engineering* **157**:255–263, 2016. <https://doi.org/10.1016/j.proeng.2016.08.364>.
- [41] J. Krishnaraj, P. Vasanthakumar, J. Hariharan, et al. Combustion simulation and emission prediction of different combustion chamber geometries using finite element method. *Materials Today: Proceedings* **4**(8):7903–7910, 2017. <https://doi.org/10.1016/j.matpr.2017.07.126>.

RECOMMENDED PROCEDURE FOR HEADROOM DESIGN ACCORDING TO GEOMETRIC PARAMETERS OF BUILDING STRUCTURES

LINDA VESELÁ

*Czech Technical University in Prague, Faculty of Civil Engineering, Department of Construction Technology,
Thákurova 7, 160 00 Prague, Czech Republic*

correspondence: linda.vesela@cvut.cz

ABSTRACT.

The system of Czech technical standards for geometric accuracy assumes that the designer determines the functional geometric parameters for a specific building. By calculation, he verifies them in the so-called “geometric plan” in the project documentation. The functional geometric parameters should be determined primarily for critical elements, i.e. for structures whose geometric accuracy is important for the execution of subsequent works, such as technologies requiring high precision and specific structures. The assumption is that designers will incorporate variations in geometric accuracy primarily in the development of the spatial parameters of the structures, which should ensure that the dimensional requirements for the completed structures will be met. One of these parameters is headroom. The design of headroom must respect the minimum height requirements prescribed by legislation, and where appropriate, by technical standards. At the same time, the design must respect the technological possibilities of the construction of individual structures – geometric deviations. To comply with the dimensional requirements for the completed structures, the geometric accuracy deviations should be determined in accordance with the requirements of the technical standards for the execution of the individual parts of the building structures and/or for their design. The aim of this article is to establish a calculation procedure for determining the safe design clearance so that the requirements of the legislation are met after implementation. The increase is determined based on a calculation procedure of the limiting geometric deviations that may affect the resulting headroom.

KEYWORDS: Headroom, geometric accuracy, limit deviation, geometric accuracy deviation.

1. INTRODUCTION

The headroom is a geometric parameter that is very important for several room types. Particularly in residential, administration or school buildings and their parts (bedrooms, living rooms, classrooms, offices, etc.), the national building regulations usually stipulate a minimum headroom that should be maintained even after the construction is completed [1, 2].

The minimum headroom is usually set to ensure that the quality and required values of the indoor climate parameters (especially maximum CO₂ values, etc.) can be maintained. The values of these parameters are usually dependent on the geometric dimensions of the rooms under consideration, and the value of the headroom can positively or negatively influence the indoor environmental parameters, especially for naturally ventilated rooms [3].

The main goal is to design and implement the dimensions of buildings so that people feel as comfortable as possible in them. Practically, this means that the dimensions must be appropriate, ceilings high enough, doorways and hallways wide enough, and so on.

It is not surprising that investors strive to ensure that the required minimum headroom is always met, therefore, this parameter is often checked after the

completion of the building. To comply with the minimum headroom requirement, the projected headroom must be designed with a margin, which, even after allowing for deviations in geometric accuracy for the construction, anticipated deflections of the ceiling slab and surface finishes, will ensure that the required minimum headroom is maintained after completion.

This paper proposes a procedure for calculating the recommended headroom using limit deviations of geometric parameters that can affect the actual headroom. The calculation procedure can be used for the design and control of the proposed clear height of newly designed rooms in civil engineering buildings. The calculation considers variations in geometric precision for the execution of the structures that may affect the resulting clearance value and the results of actual height measurements carried out on construction sites.

The analysis of technical standards shows that the headroom can be influenced by the following geometric parameters, in particular:

- deviation of the construction height,
- deviation of floor thickness,
- deflection of the ceiling slab.

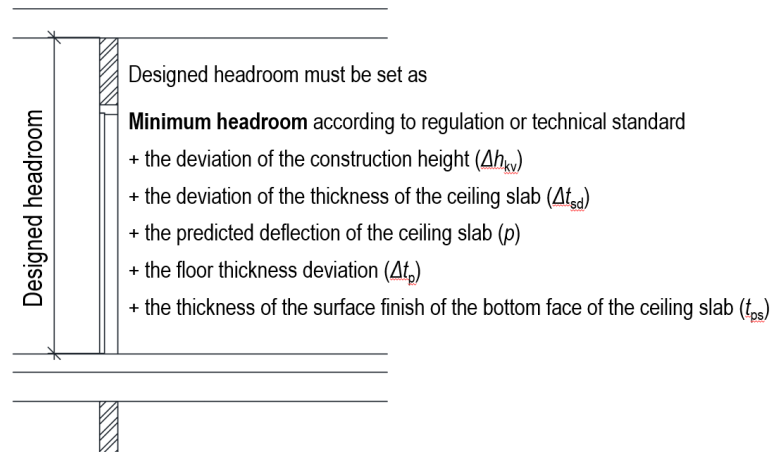


FIGURE 1. Determination of design headroom.

Therefore, the geometric accuracy of not only the non-finished structure itself, but also the deviations of the floor, the bottom face of the ceiling, and the deflection of the ceiling slab must be considered in the design and implementation of the structure according to Figure 1. The permissible deviations of the load-bearing structures, thickness of the floor, the proposed ceiling slab deflection and the surface finish of the ceiling must, therefore, be added to the minimum headroom [4, 5].

2. MATERIALS AND METHODS

2.1. CALCULATION OF THE RECOMMENDED HEADROOM

Based on the analysis of deviations in geometric accuracy and other parameters of horizontal structures, a procedure for calculating the recommended headroom was proposed, which can be used by the designer in the design documentation phase and by the contractor to check the accuracy of the design documentation. The calculation procedure is described below, including all the variables that should be considered in the calculation.

The recommended headroom ($h_{sv,dop}$) shall be calculated according to the following relation:

$$h_{sv,dop} = h_{norm} + t_{ps} + (\Delta h_{kv} + \Delta t_{sd} + \Delta t_p) \times k_{0,95}, \quad (1)$$

where h_{norm} is the required minimum headroom according to a technical standard or regulation, t_{ps} is the thickness of the surface finish of the bottom face of the ceiling slab, Δh_{kv} is the deviation of the construction height, Δt_{sd} is the deviation of the thickness of the ceiling slab, Δt_p is the floor thickness deviation, p is the predicted deflection of the ceiling slab and $k_{0,95}$ is the probability coefficient of maximum deviations.

In the case of a structure with a false ceiling, it is not necessary to take into account the surface treatment of the ceiling, i.e. $t_{ps} = 0$. If the ceiling finish is a free height false ceiling, i.e. a false ceiling whose minimum

height is not related to the type of technology to be installed in the false ceiling and its installation space, the assumed ceiling deflection can be omitted from the above relation, i.e. $p = 0$.

The deviations are considered in positive values. The geometric accuracy deviations are based on the parameters specified in the relevant technical standards for construction.

The applicable limit deviations of headroom should be indicated on the drawings in one of the following ways:

- by setting limit deviations within the quoted dimensions, e.g. 2650 (± 35) or 2650 (+20; -50),
- by specifying limit deviations within the drawing legend notes.

A negative limit deviation cannot be applied to the design minimum headroom determined by a calculation [4, 5].

The procedure for calculating the recommended headroom using the geometric limit deviations of the headroom has been developed on the basis of practical experience, where we repeatedly encounter projects, especially apartment buildings, where the headroom is designed at the limit of the minimum technical requirements. After the completion of the construction, in most cases, the investor complains about non-compliance with the basic technical requirements for buildings (non-compliance with the minimum headroom). In many cases, this problem stems from the design documentation, in which the designer, for some reason, did not respect the recommended deviations in geometric accuracy, deflections, etc., and designed the headroom without any margins. The minimum headroom cannot be guaranteed in the implementation of such a project because the building structures cannot be constructed from a technological point of view without certain deviations in geometric accuracy, even if the contractor is aware of this problem and tries to avoid it.

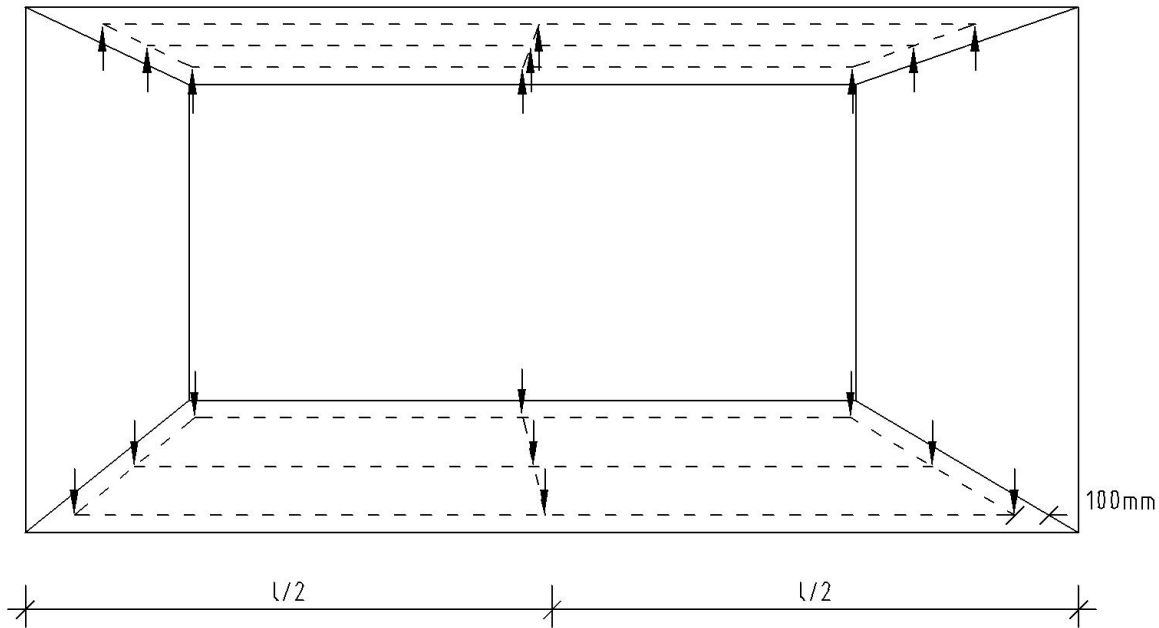


FIGURE 2. Measurement of headroom [6].

2.2. MEASUREMENT OF HEADROOM

To be able to assess whether the calculation of the headroom including the deviations of the geometric parameters is justified, experimental verification of the actual headroom on selected projects was carried out. The measurement of the headroom was always carried out in residential rooms that have a minimum headroom prescribed by the regulation, which must be respected [1, 2]

The headroom of the space under consideration (living room, bedroom, etc.) is the distance between the floor surface and the bottom face of the ceiling, or the lowest element of the ceiling (false ceiling, beams, column heads, plaster) because it should delimit a space in which a smooth horizontal and vertical movement is not impeded.

The heights of the rooms were measured at the distance of 100 mm from the walls, columns, and in the middle of the length and width of the room. The heights of openings and similar structures are checked 100 mm from the face of the supporting structure (wall, etc.), or even in the middle of the plan dimension according to Figure 2. In total, at least nine measurements were taken in each room. A measurement offset of approximately 100 mm from the edges of vertical supports (walls, columns) is recommended due to the occurrence of possible bigger surface irregularities on the edges of the structure [6, 7].

The designed headroom was subtracted from the measured value, and the headroom deviation was determined by relation:

$$\Delta_h = h_{sv,skut} - h_{sv,pd}, \quad (2)$$

where Δ_h is the calculated deviation in headroom, $h_{sv,skut}$ is the measured headroom, $h_{sv,pd}$ is the designed headroom.

The minimum Headroom according to technical standard or Regulation	No	Yes
Frequency of deviation	58	377
Percentage of all measured deviations	13.33 %	86.67 %

TABLE 1. The frequency and percentage of measured headroom that do not meet the minimum headroom according to technical standards or law regulations.

3. RESULTS

3.1. MEASURED HEADROOM DEVIATIONS

Headroom measurements were taken on a few housing projects that showed an increased risk of non-compliance with the minimum headroom because they were designed to the minimum required value or with only a minimum margin of up to 20 mm. Headroom measurements were taken after completion of the whole building and primarily in bedrooms and living rooms according to Figure 3. Figure 4 shows the frequency of deviations of the measured headroom from the designed headroom.

The evaluation shows that the designed headroom was not respected in most cases, while in about 95 % of the measurements, the actual clear headroom is lower than the designed headroom. In about 13 % of the measurements, the minimum clear headroom requirement for bedrooms and living rooms is not met according to Table 1, even if the minimum clear headroom was designed with a margin of about 20 mm.

Therefore, it cannot be assumed that if the headroom is designed with a minimum or very small margin (up to 20 mm) for geometric inaccuracy of the building

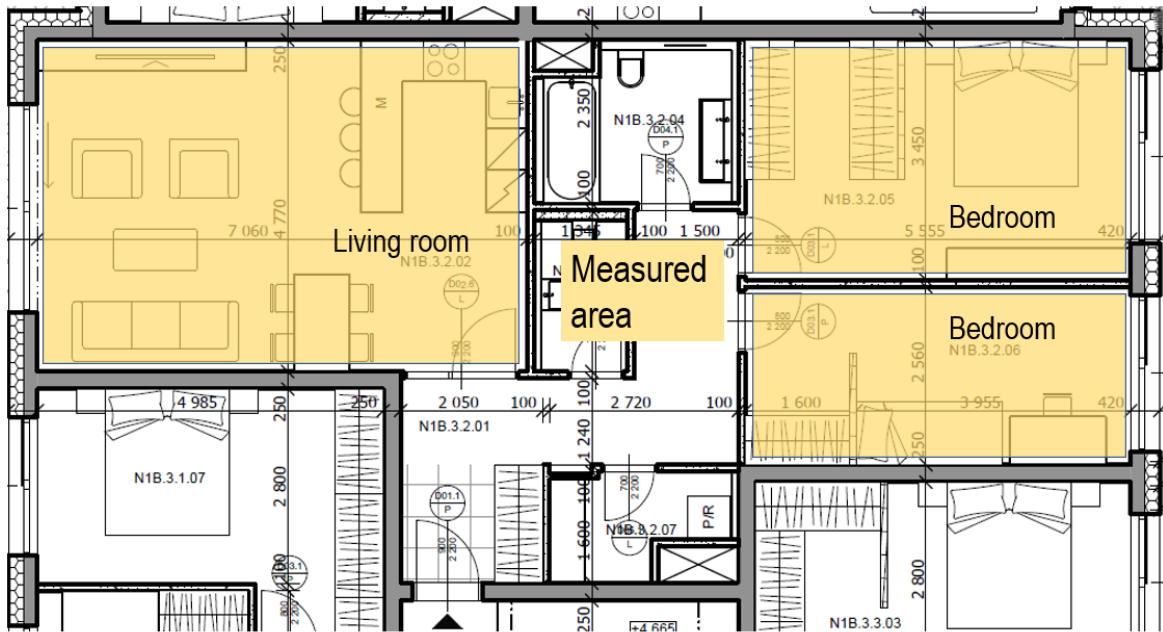


FIGURE 3. Example of measured area (bedroom, living room).

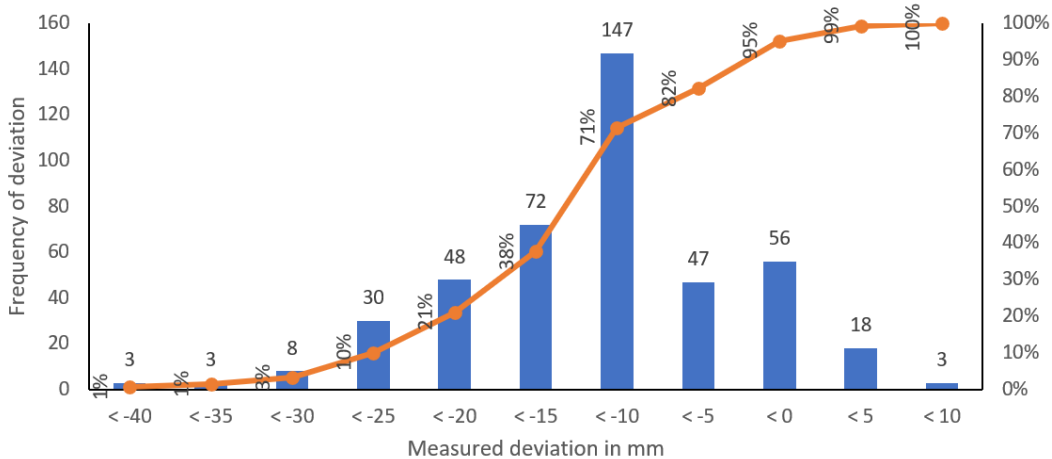


FIGURE 4. The distribution of measured deviations of headroom according to their value, frequency, and percentage.

structures, it will meet the legislation requirements. From the measurements taken, it can be concluded that the headroom will in fact be reduced, and in about 75 % of cases, the headroom will already be reduced during the rough construction. The design calculation of the recommended headroom, therefore, correctly assumes a margin for deviations in geometric accuracy, ceiling slab deflections and finishes on the underside of the ceiling that are not quoted [8].

3.2. PROBABILITY COEFFICIENT OF MAXIMUM DEVIATIONS ($k_{0.95}$)

Maximum deviations for individual geometric parameters are considered in the calculation of the recommended headroom. In practice, however, it cannot be assumed that all these maximum deviations occur simultaneously. Therefore, a coefficient of probability of occurrence of maximum deviations is implemented in the calculation. The coefficient was calculated for

the worst measured clearance deviation, called k_1 , and for the deviation that represents 95 % of all measured deviations, but the coefficient $k_{0.95}$ is used in the calculation of the recommended headroom.

The coefficient represents the probability of occurrence of 95 % of all headroom deviations and is determined on the basis of measurements made on site.

For each measured building, the negative clearance deviation representing the 95 % limit of all measured deviations was determined and compared with the maximum possible calculated deviation according to the relation (1) without adjustment by the coefficient $k_{0.95}$ and without deflection according to the following relation:

$$k_i = \frac{\Delta h_{0.95}}{\Delta h_{kv} + \Delta t_{sd} + \Delta t_p}, \tag{3}$$

where $\Delta h_{0.95}$ is the deviation representing 95 % of all measured deviations, Δh_{kv} is the deviation of the construction height, Δt_{sd} is the deviation of the thick-

ness of the ceiling slab and Δt_p is the floor thickness deviation.

The value of the coefficient $k_{0.95}$ is further determined by averaging over all projects by relation:

$$k_{0.95} = \frac{\sum_{i=1}^n k_i}{i}. \quad (4)$$

The current value of the coefficient $k_{0.95}$ was experimentally set to 0.71 [5]. Based on a more accurate analysis of the measured headroom deviations, the coefficient value can now be updated. The resulting value of $k_{0.95}$ is 0.32 according to Table 2.

Probability coefficient of maximum deviations	$k_{0.95}$	k_1
Average of all measured projects	0.32	0.44

TABLE 2. The value of the probability coefficient of maximum deviations relative to 95 % ($k_{0.95}$) and 100 % (k_1) of all measured deviations.

4. DISCUSSION

From the measured data, it can be expected that the constructed headroom is likely to be lower than the designed headroom in 95 % of cases. This fact is mainly influenced by geometric accuracy deviations brought into the structure during the construction process, which cannot be easily influenced because it is technologically impossible to construct structures without geometric accuracy deviations.

Therefore, when checking the headroom of rooms, two essential factors must always be considered. The first factor is the headroom design factor, i.e. whether the headroom has been designed with the sufficient allowance for variations in geometric accuracy, ceiling slab deflections, ceiling face finishes, etc.

If the project documentation proposes headroom that is in line with the minimum requirements of the technical standards or legislation, it is very likely that the construction headroom will be reduced during the construction process due to the tolerances allowed, and thus not comply with the minimum requirements.

The second factor is deviations in geometric parameters which may affect the constructed headroom. When checking the finished headroom, it is always necessary to check that the structures have been constructed within the recommended tolerances or deviations of geometric accuracy.

Both factors must be considered if there is any doubt whether the resulting headroom complies with legislative requirements.

5. CONCLUSION

One of the important and characteristic features of quality are the geometric parameters (ground and

height dimensions of the designed space) of the element and the structure for which boundary conditions should be set. The room dimension tolerances and measured deviations are the basic parameters that need to be established to achieve the desired result, the headroom of the space. Geometric accuracy and its deviations are often underestimated in the preparation of project documentation, even though the minimum required dimensions are one of the basic contractual and technical parameters of the building as defined in national regulations and contract documents. The failure to comply with them is often severely penalized.

To comply with standard or legal requirements for minimum headroom, the design headroom shall be determined as follows:

$$h_{sv,pd} \geq h_{sv,dop} > h_{sv,norm}, \quad (5)$$

where $h_{sv,pd}$ is the design headroom, $h_{sv,dop}$ is the calculated recommended minimum headroom, $h_{sv,norm}$ is the minimum headroom according to a technical standard or regulation.

Deviations of a finished headroom shall comply with the geometric accuracy limits specified in the technical standards.

ACKNOWLEDGEMENTS

The author is grateful to the Czech Technical University in Prague. This study was financially supported by grant SGS20/152/OHK1/3T/11 of the Czech Technical University in Prague.

REFERENCES

- [1] Vyhláška č. 268/2009 Sb., Vyhláška o technických požadavcích na stavby [Decree No. 268/2009 Coll. on Technical Requirements for Buildings as amended].
- [2] Nařízení č. 10/2016 Sb. hl. m. Prahy, Nařízení, kterým se stanovují obecné požadavky na využívání území a technické požadavky na stavby v hlavním městě Praze (pražské stavební předpisy) [Regulation No. 10/2016 Coll. on General requirements for land use and technical requirements for buildings in the Capital City of Prague (Prague Building Regulations)].
- [3] O. Franek, Č. Jarský. On reducing CO₂ concentration in buildings by using plants. *Acta Polytechnica* **61**(5):617–623, 2021. <https://doi.org/10.14311/AP.2021.61.0617>.
- [4] L. Veselá, J. Synek. Quality control in building and construction. *IOP Conference Series: Materials Science and Engineering* **471**(2):022013, 2019. <https://doi.org/10.1088/1757-899X/471/2/022013>.
- [5] L. Veselá, J. Klečka. TS 01 – stanovení minimální návrhové světlé výšky místností (Technický standard ČKAIT) [TS ČKAIT No. 01 – Determining the minimum height of the projected headroom]. Informační centrum ČKAIT, s.r.o., 2018. ISBN 978-80-88265-13-9 [2022-11-19], <https://profesis.ckait.cz/dokumenty-ckait/ts-01/>.

- [6] Český normalizační institut. Geometrická přesnost ve výstavbě. Kontrola přesnosti. Část 3: Pozemní stavební objekty. Technická norma ČSN 73 0212-3 [Geometrical accuracy in building industry. Accuracy checking. Part 3: Building structures. Standard No. ČSN 73 0212-3], 1997.
- [7] Český normalizační institut. Geometrická přesnost ve výstavbě. Navrhování geometrické přesnosti. Technická norma ČSN 73 0205 [Geometrical accuracy of Building. Design of geometric accuracy. Standard No. ČSN 73 0205], 1995.
- [8] M. Tuháček, O. Franek, P. Svoboda. Application of FMEA methodology for checking of construction's project documentation and determination of the most risk areas. *Acta Polytechnica* **60**(5):448–454, 2020. <https://doi.org/10.14311/AP.2020.60.0448>.

L^AT_EX CLASS ERRORS AND WARNINGS

- **Warning:** Article ‘allabaksh’ has [eprint] option
- **Warning:** Article ‘cihla’ has [eprint] option
- **Warning:** Article ‘kalus’ has [eprint] option
- **Warning:** Article ‘kotsovou’ has [eprint] option
- **Warning:** Article ‘lechner’ has [eprint] option
- **Warning:** Article ‘nogueira’ has [eprint] option
- **Warning:** Article ‘oyesola’ has [eprint] option
- **Warning:** Article ‘vesela’ has [eprint] option